A new unfolding method for the MAGIC telescope

Thesis submitted for the Degree of Doctor of Physics at the University of Dortmund

by

Valentin Curtef

Supervised by

Prof. Dr. Dr. Wolfgang Rhode

And we complain that we exhaust ourselves too fast when, on the contrary, we should wonder how new the world appears to us, just because, for a moment, we have forgotten it.
(A. Camus)

Contents

Introduction

As Kepler developed his heliocentric system, he assumed that the planets travel around the sun on circular orbits. Confronting this hypothesis with measured data for the orbit of the planet Mars, an inconstancy occurred as one point was too far out from the theoretical orbit. Despite the epicycle concept used in unanimity at that time, Kepler relied entirely on the experimental data and rejected the hypothesis of a circular orbit for a new one, that of an elliptical orbit (Köstler, 1995). It was the first time in physics that an experiment had a crucial relevance, being a corner stone for modern science.

The importance of scientific experiments lies in the fact that direct information is obtained from phenomena being observed. In the field of Astronomy this information is predominantly in the form of photons, messengers of the electromagnetic force, reasoning why the major part of the observed universe is of electromagnetic nature. For high energy photons, the Earth's atmosphere acts like a shield and balloons or satellites are needed to observe them. The extreme case, of very high energy photons demands a large collection area, which makes direct measurements difficult even by means of balloons and satellites. The only chance to observe very high energy photons is indirectly, i.e. by their interaction with the Earth's atmosphere. From such an interaction electrons and positrons are created, which travel faster than the speed of light in the atmosphere and produce Čerenkov light observable with the MAGIC telescope. Indirect observation of very high energy photons losses part of the photon information (energy) in the atmospheric interaction. In order to recover the energy of the initial photons, one needs to reconstruct it from the measurements, meaning to unfold. Thus, unfolding is the normal step back to the direct information which enables physicists to understand reality.

The unfolding method has a long history being already applied by Gauß (1794) for the orbit reconstruction of planetoids from few data points. It has also difficulties, i.e. suffers from oscillations induced by rare measured events which have a small weight and thus, a large error for the unfolded solution. To overcome such problems, a regularization is needed, which means to cut out the oscillating parts of the solution.

The present thesis describes an unfolding method whose principle is to determine the probability that a certain set of events has a certain range of energy. Measured data include different characteristics of the interaction of very high energy photons with the atmosphere. Only those characteristics which correlate with the energy of the initial photon known from Monte Carlo simulations, called *unfolding variables*, are required to compute the probability. Since the parameter space of the unfolding results is large, the search of a solution is time demanding (days). To overcome this inconvenience, an optimization technique was developed, which permits to achieve an unfolding solution within few minutes.

Unfolding methods are not related to the analyzed data and one is interested to know to which extent the unfolding solution encapsulates the unfolding variables in the data. For this purpose, new factors independent of the unfolding method used, were defined. These factors enable the use of the unfolding methods to obtain information about the unfolding variables in the data, independent

of the unfolding solutions as well. One of these information determines if the unfolding variables exist in the data after applying standard cuts (analysis) or additional cuts. This opens the way to study the effects of different cuts to the data and how they will change the content of the unfolding variables in the data. Moreover, using these factors, the search domain for the unfolding solution is considerably reduced.

The thesis is divided into six chapters. The first chapter describes the different interactions of cosmic rays with the Earth's atmosphere, as well as a technique to observe the outcomes of the interactions (showers), using the Major Atmospheric Gamma Imaging Čerenkov (MAGIC) telescope. Furthermore, an outline of the image processing analysis of the showers is given.

In the second chapter, the motivation why unfolding should be used is underlined. Two major unfolding methods are described: energy estimator and probability estimator, with and without the regularization effect and also an example are presented.

Further on, the probability estimation method with regularization will be used to reconstruct the energy spectra of Active Galactic Nuclei (AGN). Chapter three is dedicated to AGN, their structure, observation method, classification with respect to the angle between the observer's line of sight and the rotation axis of the AGN. The large scale structure of the AGN ($\sim 10^4 - 10^6$ pc) is dominated by radio jets, whereas the small scale one ($\sim$ pc) by the supermassive black hole (in the center of the galaxy) surrounded by an accretion disk (close to the black hole) and by a torus (further out). Finally, the mechanisms to obtain very high energy photons (Fermi acceleration, inverse Compton scattering) are described together with two relativistic factors which change the intrinsic characteristics of the AGN: supperluminal motion and Doppler factor.

The fourth chapter presents the unfolding program together with the unfolding variables used. To overcome the large parameter space to be explored for finding a solution, an optimization algorithm was developed. For the optimization, two new factors were introduced: the variability factor (ρ_V) to determine the smoothness of the convergence of the unfolding program, and the probability factor (π), which gives a measure of closeness of the number of unfolded events to the number of excess events. The unfolding method is tested on Monte Carlo and also on real data (Crab Nebula).

In the fifth chapter the unfolding method is applied to three special AGN, called blazars (the jet is oriented towards the observer): Markarian 421, Markarian 501 and PKS 2155-304. The obtained spectra follow the results of already established methods, and in most of the cases (Markarian 501 and PKS 2155-304) the spectra could be extended to higher and/or lower energies. For two different cuts applied to PKS 2155-304 a discordance between the spectra appeared from unknown reasons. Using one of the factors introduced in chapter four (π) an explanation for the discordance could be found: one of the cuts contained information about the zenith angle, whereas the other one did not. The presence of the zenith angle in the analyzed data curves the spectrum at lower and higher energies and this is exactly the discrepancy observed for the spectra of PKS 2155-304.

As the spectra emitted by blazars are absorbed on the way to the observer, the measured spectra need to be re-absorbed to obtain the emitted spectral energy distribution (SED) of the AGN. In the sixth chapter a re-absorbtion model is applied to the spectra obtained in chapter five. For sources at higher redshift absorbtion is expected to strongly suppress the higher energies one can observe. From the observed spectra studied, such a suppression could not be detected for an optical opacity of ~ 1 (suggested by present observation), phenomenon called *TeV crisis*. Therefore, the new presented unfolding method enforces the conclusions drawn by other unfolding methods that too high energy fluxes appear above TeV energies.

The thesis ends with conclusions and outlines.

Chapter 1

The MAGIC Telescope

1.1 Photons as messengers

As we look at the sky, the universe challenges us with its mysteries, but also offers us its enormous beauty. For a physicist, the beauty of the universe is information which appears also in form of particles. Particles are the messengers of far away objects, but unfortunately only the stable ones reach Earth. Among the stable ones, electrons and protons reach the highest energies, but they are reflected by the magnetic field in the intergalactic medium and galactic plane and one cannot track them back to their source. Due to this fact, the only messengers remained are photons and neutrinos. Neutrinos travel directly from the interior of the object where the physics takes place, but so far no neutrino was detected except from our Sun and the Supernova 1987A. Unlike neutrinos, photons (γ) that we can see are not from the interior of the object, but still they remain the only available messengers of the far reaching objects in the universe. In Fig. 1.1 this feature of the possible messenger is presented.

Optical and radio band are easiest to detect from the ground, but they do not exhaust the electromagnetic band. One has to go outside the Earth's atmosphere with balloons and satellites to overcome the absorbtion of photons for a broader electromagnetic band. As one reaches higher energies, the collection area of the satellites drops rapidly, so too much observation time for the satellite experiments would be needed to obtain sufficient statistics. Thus, the only possible way to observe γ's at very high energies (VHE) is from their interaction with the atmosphere. Thus one uses the atmosphere as a detector of very high energy photons.

1.2 Čerenkov light

Nothing can travel faster than the light in vacuum, but if the light travels in a given medium of index n it changes its velocity to $\frac{c}{n}$. If a charged particle travels in the same medium with a velocity $v > \frac{c}{n}$, the particle polarizes the medium for a short time, after which light is emitted continuously. As the particle is moving slower than $\frac{c}{n}$, the emitted photons act like dipoles and annihilate each

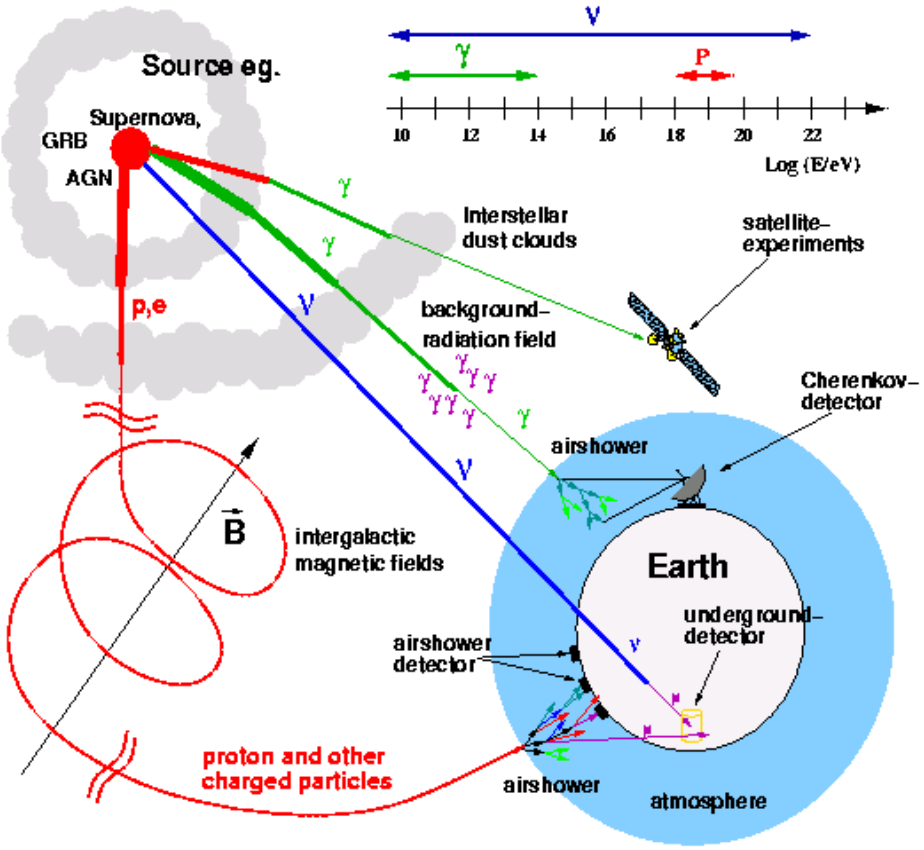

Figure 1.1: The astronomical messengers: photons, neutrinos and charged particle. Only photons and neutrinos can be tracked back to their source, whereas the charged particle loose the information on the source origin due to magnetic field interaction (Wagner, 2004).

other while, as the particle is moving faster than $\frac{c}{n}$, the dipole effect is not symmetric anymore and the photons sum up in the Čerenkov light.

The photons are emitted under a specific angle, the so-called Čerenkov angle, which depends on the index of the medium and the velocity of the particle as follows:

$$\cos\theta = \frac{\frac{c}{n}t}{\beta ct} = \frac{1}{n\beta}. \tag{1.1}$$

For water and air, one has indexes $n_w = 1.33$, and $n_a = 1.00029$ respectively, so the angles of the emitted photons will then be $\theta_w = 41.2°$, and $\theta_a = 1.3°$.

The minimal energy of the charged particle is given by

$$E_{min} = \frac{m_0 c^2}{\sqrt{1-\beta_{min}^2}} = \frac{E_0}{\sqrt{1-\frac{1}{n^2}}}, \tag{1.2}$$

where E_0 is the energy at rest. Thus, minimal energies for an electron and a muon in water are $E_e^{min} = 0.775$ MeV, $E_\mu^{min} = 160.24$ MeV respectively, and in air are $E_e^{min} = 21.225$ MeV, $E_\mu^{min} = 4.388$ TeV respectively.

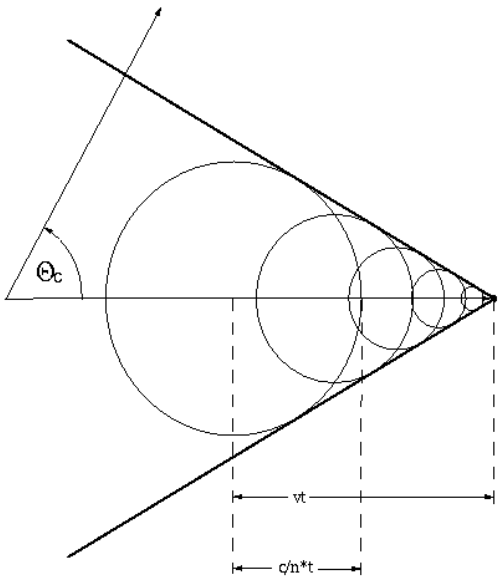

Figure 1.2: The Čerenkov effect, i.e. when a charged particle travels faster than the speed of light in a medium. The circles represent photons emitted after the medium was polarized, and the cone is the summation of the emitted light (Jackson, 1998).

The index of Earth atmosphere is changing with altitude h and is proportional to the density of the atmosphere:

$$n(h) = 1 + \rho_0 e^{-\frac{h}{h_0}},$$

where $\rho_0 = n_0 - 1 = 0.000298$, with n_0 the index at sea levels and h_0 a normalization factor. The Čerenkov angle and the energy become

$$\theta(h) = \arccos \frac{1}{\beta\left(1 + \rho_0 e^{-\frac{h}{h_0}}\right)} \quad \text{and} \quad E_{min}(h) = \frac{E_0}{\sqrt{1 - \frac{1}{\left(1+\rho_0 e^{-\frac{h}{h_0}}\right)^2}}} \tag{1.3}$$

The number of produced photons during the travel of the particle with charge ze is:

$$\frac{d^2N}{dEdx} = \frac{\alpha z^2}{\hbar c}\left(1 - \frac{1}{\beta^2 n^2(E)}\right), \tag{1.4}$$

with α the fine-structure constant. For the electron one obtains $\approx 370 \sin^2\theta(E)\text{eV}^{-1}\text{cm}^{-1}$.

1.3 Extended air shower

Particles with very high energies don't survive the travel to the Earth's ground because they interact with a nucleus in the atmosphere due to conservation of energy and momentum. The output of this interaction will induce a cascade of particles collimated along the direction of the initial particles, called air shower.

First observations of air showers go back to the 1920s. Although these observations included only simple structures of air showers, in the next decade they have played an important role in the development of electromagnetic cascades. It was Pierre Auger with his collaborators who discovered extended air showers first (Auger et al., 1939).

As one can observe the air showers only and not the initial particles, the energy of the particles and the interaction point with the atmosphere are not known. To this extent, a good understanding of the way showers develop is desirable. Due to fluctuations which appear in the development of showers it is impossible to determine the features of individual showers. By mean of such consideration, mathematical models, available now, provide only a statistical description of the showers development. To this purpose, Monte Carlo simulations are used.

1.3.1 Electromagnetic shower

An electromagnetic shower is induced by photons, electrons or positrons. In the case of electrons and positrons, because of bremsstrahlung, a photon with high energy is produced. In all cases, the photon will react with a nucleus and produce an electron-positron pair, which induces a cascade (or secondary output).

A detailed description of the shower is not easy to obtain, but main features of the induced air shower can be obtained through the simplified model of (Heitler, 1966). In this model, the cascade consists of particles of the same kind, which interact again after every length λ, new particles being created, each of them with half of the corresponding primary energy. This means that, after the interaction of a photon of energy E_0, an electron-positron pair is created at the length λ, each with energy $E_1 = E_0/2$. Two new photons are created due to bremsstrahlung, and the number of particles at 2λ is 4, each with energy $E_2 = E_0/4$. The new created photons will induce two new pairs electron-positron and additionally, two photons are produced due to bremsstrahlung, which implies that at the length 3λ there is a number of 8 particles, each with energy $E_3 = E_0/8$, and so on. So, at the length $n\lambda$ there are 2^n particles created each with energy $E_n = E_0 \cdot 2^{-n}$. The development of the shower stops at a critical energy E_c, where the shower reaches its maximum of created particles. Since ionization of electrons and positrons is stronger then bremsstrahlung, no further photons are produced and the existent photons are not able to produce new particles, losing their own energy through Compton scattering. Thus, starting from the critical energy, no new particles are created and the shower dies out.

Having the critical energy E_c and the relation $E_0 \cdot 2^{-n} = E_c$, one finds the maximum number of created particles or the depth of the shower as follows

$$t_{max} = n_{max} = \frac{\ln\left(\frac{E_0}{E_c}\right)}{\ln 2} \tag{1.5}$$

Even with such simple models, one manages to obtain important features of the shower, such as the fact that the number of created particles is increasing exponentially with the depth of the shower, where as the energy of the produced particles decreases exponentially with depth.

A more realistic scenario is one in which we have to keep in mind losses due to ionization and also the specific cross sections. For such cases, the number of electrons above the critical energy is

$$N_e(t, E_0) = \frac{0.31}{\sqrt{\ln(\frac{E_0}{E_c})}} e^{t\left(1-\frac{3}{2}t\ln s\right)}, \tag{1.6}$$

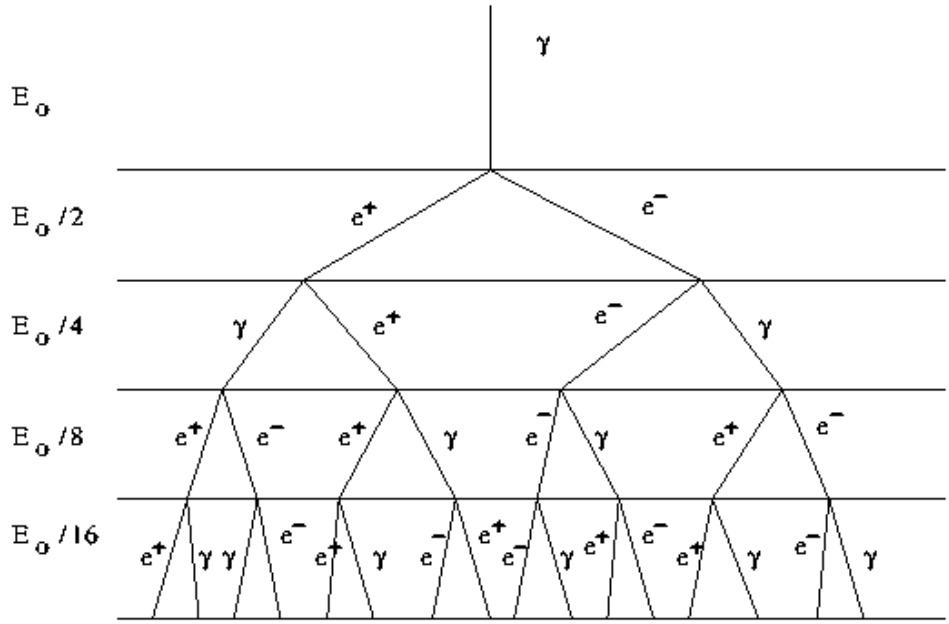

Figure 1.3: The electromagnetic shower. At the top the initial γ-ray and the first steps of the shower's developments in the simplified case of symmetric distribution of the energy of the initial γ-ray (Bojahr, 2002).

where s is the age of the shower and is given as

$$s = \frac{3t}{t + 2\ln(\frac{E_0}{E_c})}. \tag{1.7}$$

The age s of the shower is considered 0 at the beginning, smaller then 1 during the period of particle creation of the cascade, 1 where the shower reaches it's maximum, bigger then 1 during the period when it dies out, and 2 when $N_e < 1$.

During the development of the shower, the electrons and the positrons are scattering each other due to Coulomb force, which induces deviation from the shower axis. One can compute the lateral distribution of the electrons as (Greisen, 1956)

$$\rho_e(r,t,E) = \frac{\Gamma(4.5-s)}{2\pi\Gamma(s)\Gamma(4.5-2s)} \cdot \frac{N_e(t,E)}{r_M^2} \cdot \left(\frac{r}{r_M}\right)^{(s-2)} \cdot \left(1+\frac{r}{r_M}\right)^{(s-4.5)}, \tag{1.8}$$

where r_M is the Molier radius – $r_M = 21.2$ MeV$\cdot(X_0/E_c) \approx 79$ m in air at sea level –, and Γ is Euler Gamma function. The domain of validity for this formulae is $1 \leq s \leq 1.4$.

Showers induced by electrons or positrons are rare and are part of the background of γ-induced showers, the difference is that the electron and positron induced showers arrive isotropically at the telescope, where as the γ-induced showers can be tracked back to their source.

1.3.2 Hadronic shower

The difference between electromagnetic showers and hadronic showers lies in the fact that the initial particle is a hadron, so in the interaction with the atmosphere, the strong and the weak forces are

involved. The most predominant hadrons are protons.

The output of the interaction of the proton with the atmosphere consists mainly of pions with the known decay:

$$\pi^0 \to \gamma\gamma, \quad K^+/\pi^+ \to \mu^+ + \nu_\mu, \quad K^-/\pi^- \to \mu^- + \bar{\nu}_\mu. \tag{1.9}$$

According to the pion decay, different types of showers develop. The neutral pion (with decay length of $\gamma_{\pi^0} = 2.51 \times 10^{-6}$ cm) will decay into two photons which will induce an electromagnetic shower close to the decay point. The charged pion has a sufficient large decay length ($\gamma_{\pi^\pm} = 780$ cm) to interact with other nuclei in the atmosphere and to induce new hadronic showers, similar to the initial proton interaction. Because of the longer decay length of the $\pi^\pm$ and $K^\pm$ comparative to the π^0, the hadronic component of the shower will penetrate in the atmosphere deeper than the electromagnetic component. The hadronic component has the smallest deflection from the shower axis, thus the depth of the shower will be considered relative to this component. A scheme of the hadronic shower is shown in Fig. 1.4.

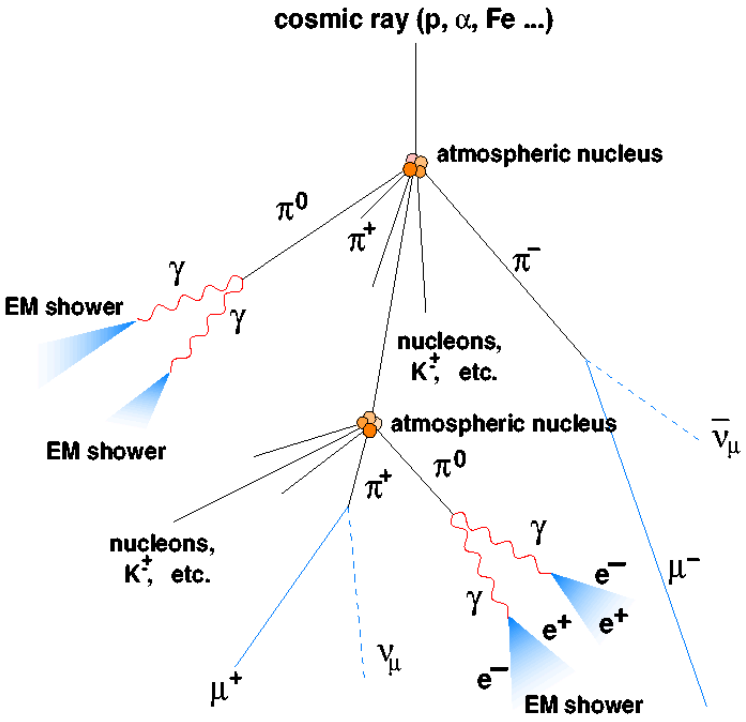

Figure 1.4: The hadronic shower and the three components: hadronic, electromagnetic and muon. At the top the incoming charged particle and the schematic interaction with a nucleus in the atmosphere. The hadronic part of the shower is closer to the direction of the initial particle, whereas the electromagnetic and muon parts developing at some distance from the hadronic outcomes (Wagner, 2006).

The interaction of the $\pi^\pm$ and $K^\pm$ with nuclei in the atmosphere ends with their decay into muons and neutrinos. Because of their small cross section and long lifetime, muons and neutrinos interact rarely with the atmosphere and travel straight to the ground.

The momentum transfer from the initial proton-nucleus interaction to the secondary output, scatters the electromagnetic and the muon components of the shower far from shower's axis. This applies to every new hadronic shower, so the image of the entire shower is dispersed.

To maintain the hadronic component of the shower, a big part from the energy of the initial proton is needed. Moreover, the muon component also diminishes the initial proton energy. In conclusion, to produce nearly the same amount of $e^{\pm}$, and thus Čerenkov light, a proton induced shower needs more energy in comparison with an electromagnetic shower.

Thus, for a proton with energy E_0 GeV which interacts at the depth λ_p in the atmosphere, losing $(1 - K_{el})$ of its energy by producing a number of ζ secondary pions ($\frac{1}{3}$ neutral), the depth of the maximum is the sum of the depths of the maximum of the electromagnetic showers and the interaction length of the primary proton (Stanev, 2004)

$$X_{max} = X_0 \ln \left[\frac{2(1 - K_{el}E_0)}{(\zeta/3)\varepsilon_0} \right] + \lambda_p(E_0), \tag{1.10}$$

and the number of electrons at the shower maximum as

$$N_e^{max} = \frac{1}{2}\frac{\zeta}{3}\frac{2(1 - K_{el}E_0)}{\varepsilon_0} \tag{1.11}$$

The total number of electrons in a hadronic shower is given by Greisser-Hillas formula, as:

$$N_e(X) = N_e^{max} \left(\frac{X - X_1}{X_{max} - \lambda} \right)^{\frac{X_{max}}{\lambda} - 1} \cdot \exp\left(\frac{X - X_1}{\lambda} \right), \tag{1.12}$$

where X_1 is the point of first interaction, and λ the mean free path.

1.3.3 Differences between γ- and hadron-induced showers

As we have already seen in section 1.1., the only particles to keep the information about their origin are the photons, so γ-induced showers are crucial in the observation of very high energy sources. Unfortunately, together with γ showers one observes also the hadronic showers, which are many orders of magnitude more numerous than γ showers and constitute the major component of the background. To overcome this inconvenience, an understanding of the differences between the two types of showers is requested.

- The absorbtion length of the hadronic shower is much larger then the one of the electromagnetic shower. This implies that the hadronic shower attains its maximum deeper in the atmosphere than the electromagnetic one and is more extended on the longitudinal side, for the same initial energy.
- A hadronic shower is more irregular than an electromagnetic one, since it includes electromagnetic showers spread around the shower's axis.
- The electromagnetic showers induced by π^0 are not so compact as the γ-induced ones.
- Only hadronic showers develop muon components in their structure.

Even if the differences mentioned above give us a clue how to separate the two types of showers, they are energy dependent. This means that at very high energies one can clearly see the differences, but as the energy drops under 100 GeV, the differences reduce so much that it gets difficult to distinguish between the shower types.

1.4 The Magic Telescope

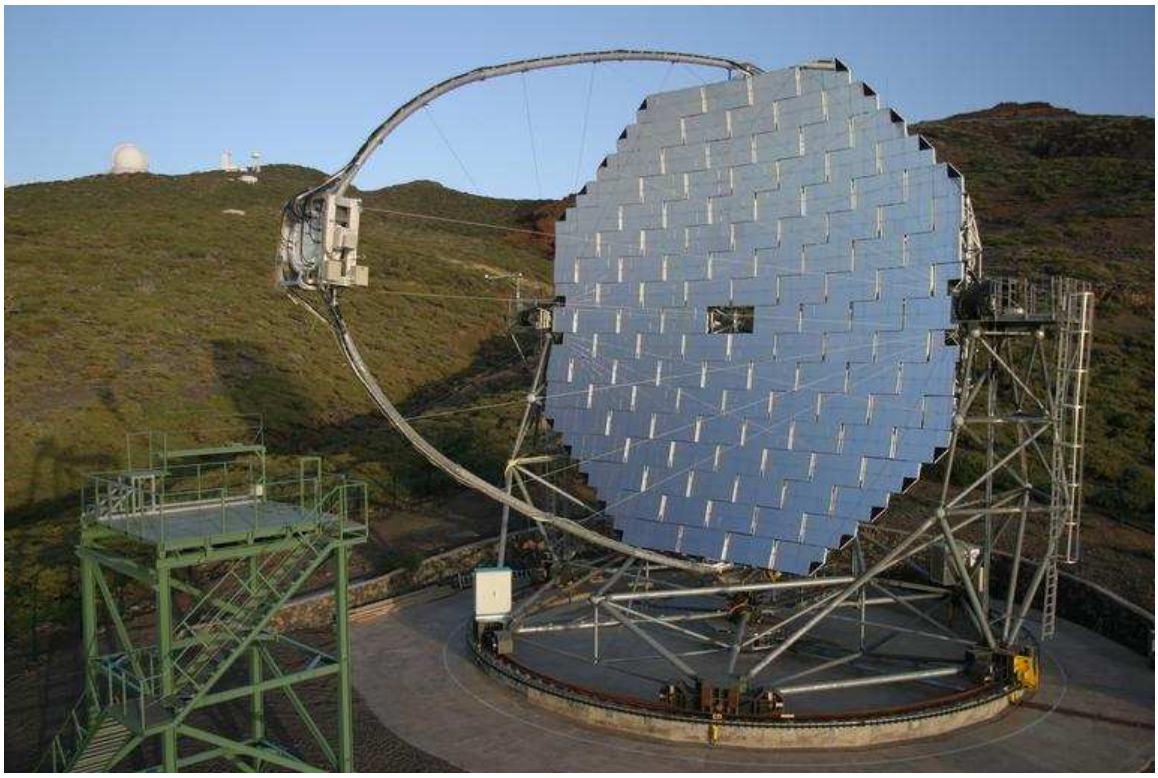

Figure 1.5: The MAGIC I Telescope on La Palma, Canare Island. (Wagner, 2008)

The Major Atmospheric Gamma Imaging Čerenkov telescope (MAGIC) is the biggest operating telescope in the world which uses imaging atmospheric techniques. It is located in the Roque de los Muchachos Observatory (28° N 17.9° W at 2200 m above sea level), island La Palma (Canare Islands)[1].

Further on, a short description of main features and components of the telescope will be presented.

1.4.1 Tracking

The telescope has an alt-azimuth-mount placed on a circular rail of 18 m diameter, which facilitates its movement during the observation. Two 11 kW motors for the azimuth direction and another one for the zenith direction perform the movement of the telescope, are capable to attain any position within 20 s (a great achievement for a 60 tones telescope), which helps in the observation of the Gamma Ray Burst (GRB) (Bretz, 2006). The 14-bit shaft encoders manage to control the telescope for the angular tracking of the observed source with an accuracy of 0.022°.

[1]It is believed to be the same island from which Christopher Columbus started his journey discovering the New World: America.

1.4.2 Optics

The mirror dish of the telescope has 17 m diameter and was built with an octagonal parabolic reflector of 239 m^2 area, tessellated in 956 quadratic mirror elements of 49.5 $\times$ 49.5 cm^2 each (Bastieri, 2005), grouped in panels. The panels consist of four mirrors (or three at the edge) each, arranged such that they give an overall time spread of 0.8 ns. The curvature of the individual mirror elements is spherical and their focal lengths vary along the radial position from 17 m at the center, to 18 m at the edge. For the construction of the mirror elements, an aluminium box was filled with an aluminum honeycomb structure to warrant lightness and rigidity; the average reflectivity of the mirrors is 85% with a roughness of 10 nm.

An Active Mirror Control (AMC) is used to correct distortions of the panels due to gravity effects at different tracking positions (Mirzoyan, 2003). The mirror adjustment has to be done every time before starting to track a new source, but this operation takes around four minutes. Instead of performing it anew, it is enough to do it once, at the beginning of every observation night and preserve the data in a file, which can be accessed at any time. So, the four minutes operation (AMC) is replaced with one of a few seconds (Look Up Table).

1.4.3 Camera

The Camera is the heart of every Image Atmospheric Čerenkov Telescope (IACT). The MAGIC camera is 1.5 m in diameter, with a weight of 450 kg and has a field of view (FOV) of 3.5°. It consists of 397 small pixels called *inner pixels* with 0.1° FOV, and 180 big pixels called *outer pixels* with 0.2° FOV (Ostankov et al., 2001). The structure of the camera facilitates the observations of γ-showers at low energies (30-200 GeV), which attain their maximum between 8 and 11 km from the ground. Under these circumstances, the shower will be in the inner part of the camera and the small pixels will allow a better recognition of the shower's structure.

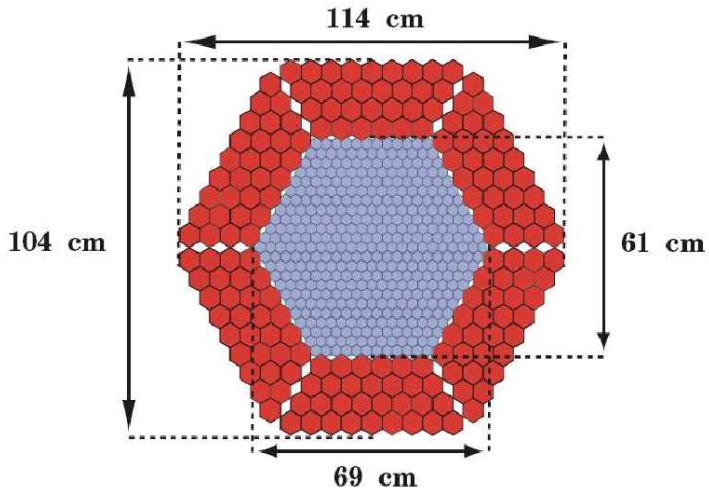

Figure 1.6: The Camera of the MAGIC Telescope. In grey the inner pixel, in red the outer pixel (Zanin, 2006).

Every pixel of the camera is composed of a photon-multiplier tube (PMT), which has typical time response of 1 ns and quantum efficiency of 28% on the peak value, and an aluminium tube with a form close to a Winston cone, through which the light is guided towards the PMT.

The entire camera is protected by a plexiglass window and by two lids, which are open only during observation. To increase the focus, the camera can be moved forward and backward with respect to the mirror dish in order to obtain different focuses, ranging from some meters to infinity.

1.4.4 Trigger

The events handled by the camera only last for ns, which will imply a huge number of events per observation. Since not all of the events are showers that can be reconstructed, a threshold (number of photoelectrons per pixel) is imposed as well as a minimum number of neighboring pixels over a given threshold in a given time window.

The trigger of the MAGIC telescope is a two-level system similar to the trigger systems used in high energy physics experiments. First, one checks if the signal in every pixel is greater than a given threshold. If this is true, a digital signal is generated with the standard duration of $\sim$ 3ns and the pixels are called lighted.

At Level 1 Trigger, the trigger area consists only of the inner part of the camera and is divided into 19 overlapping hexagonal regions of 36 pixels each. The condition imposed in this step is to accept only those lighted pixels surrounded by three other lighted ones in a compact configuration (if one takes a pixel out, there remain no isolated pixels).

Level 2 Trigger processes the pixel digital information to perform a topological selection and to reject unwanted classes of events, such as hadron or muon events (Paoletti, R.; et al., 2007).

1.5 Analysis

The information obtained during the observation of a source, called raw data, is the starting point in general analysis of Gamma Astronomy, performed in the following steps

- Calibration of the signal;
- Image cleaning;
- γ/hadron separation.

All these steps are done with MARS – MAGIC Analysis and Reconstruction Software (Bretz et al., 2005).

1.5.1 Data

Data are taken with a trigger rate of $\sim$ 200 Hz and saved on disk, in a file called *run*. When a specific amount of events, which survive the trigger, is reached (50000 in general), a new run-file starts. Data runs can be taken in two different modes: *On-Off* and *Wobble* as emphasized in Fig. 1.7.

- The On-Off mode is the classical way of observation, which consists of On-position (source in the center of the camera) and Off-position (in the neighborhood of the source and without the source), with ratio 1:2 observation time. To get the desired result, one has to subtract the Off-data (background) from the On-data (signal and background). The advantage of this method is given by the central position of the source in the camera, which permits a better reconstruction of low energy events. However, this observation mode has a major disadvantage: one loses time with the Off-data.

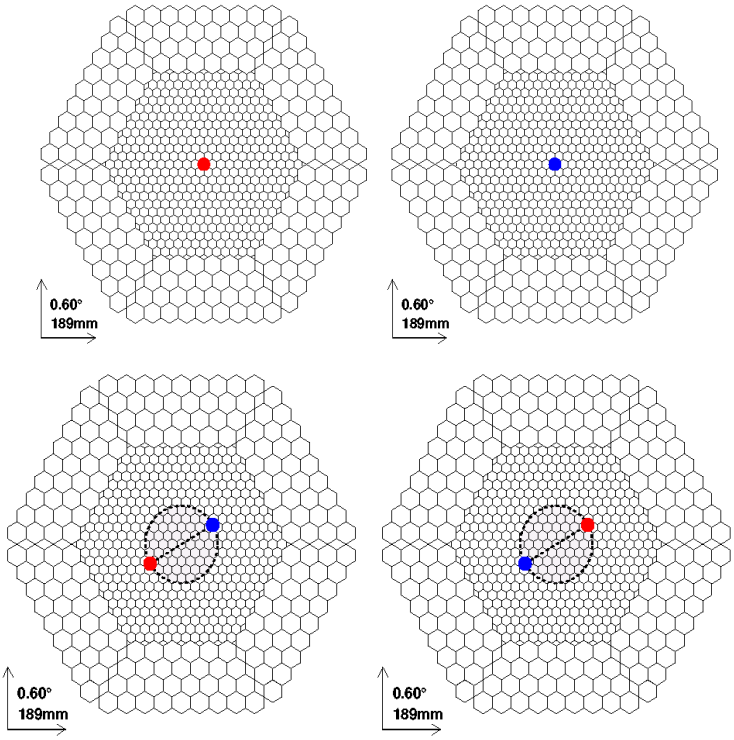

Figure 1.7: On top the On-Off observation mode, i.e. red the On position, with blue the Off position. As both are in the center of the camera, for better sensitivity, more observation time is needed. Bottom: the Wobble mode, where On (red) and Off (blue) position are both in the camera, but shifted from the center. To gain a uniform distribution of the background, the On and Off position have to be interchange during observation, as exemplifies in the left and the right side (Bretz, 2006).

- Wobble mode is characterized by the fact that On-position and Off-position are simultaneously in the camera. To this extent, one has to move the On-position slightly from the center of the camera and the Off-position diametral opposite to the On-position. In this way, one gains observation time. The source position in the camera changes during the observation, unlike in the On-Off mode, which implies a sensitivity loss since only the inner part of the camera is triggering.

1.5.2 Calibration

For a proper way of reading the recorded data during the observation, one needs to know the response of the camera to the received light. In this sense, every PMT will transform the received photons through the photo-electric effect, into a number of photo-electrons (phe). This number is called the conversion factor and is a known property of every PMT. However, this value changes slightly from night to night and its exact determination is necessary before any observation. To accomplish this, a light pulse is emitted to the camera at different wavelengths which illuminates it uniformly. Together with the known conversion factor of the PMTs (measured before they where installed on the camera), the conversion factor is given as the ratio between the sum of all phe obtained from the illumination of the camera and the mean digital charge of each pixel counted in the Fast Analog

to Digital Convertor (FADC).

Moreover, during the observation a calibration pulse (50 Hz) is sent to the camera which illuminates it with a fixed intensity and the settings for the high-voltage are re-arrange in order to obtain a uniform response of the camera. The number of phe is calculated for each pixel individually such that any eventual mis-behaviors can be corrected.

The so called pedestal is used to obtain information about the light of the night sky (like stars in the FOV of the camera) or noise sources (such as electronics). For this, a number of 1000 events are taken with random trigger which diminish considerably the probability that a shower arrives simultaneously with the pedestal run taken (Gaug, M; et al., 2005).

1.5.3 Image cleaning

For the future continuation of the analysis, it is important to decide if a pixel belongs to a shower or is just a renegade pixel of the night sky background in which case it is rejected. For this purpose, one defines the core pixel as the inner part of the shower in the camera and the neighbor pixel as the ones surrounding the core pixel. To be able to decide into which category the pixel belongs, each type of pixel has a given minimum number of phe required. Two type of image cleaning are possible: *absolute* and *relative*.

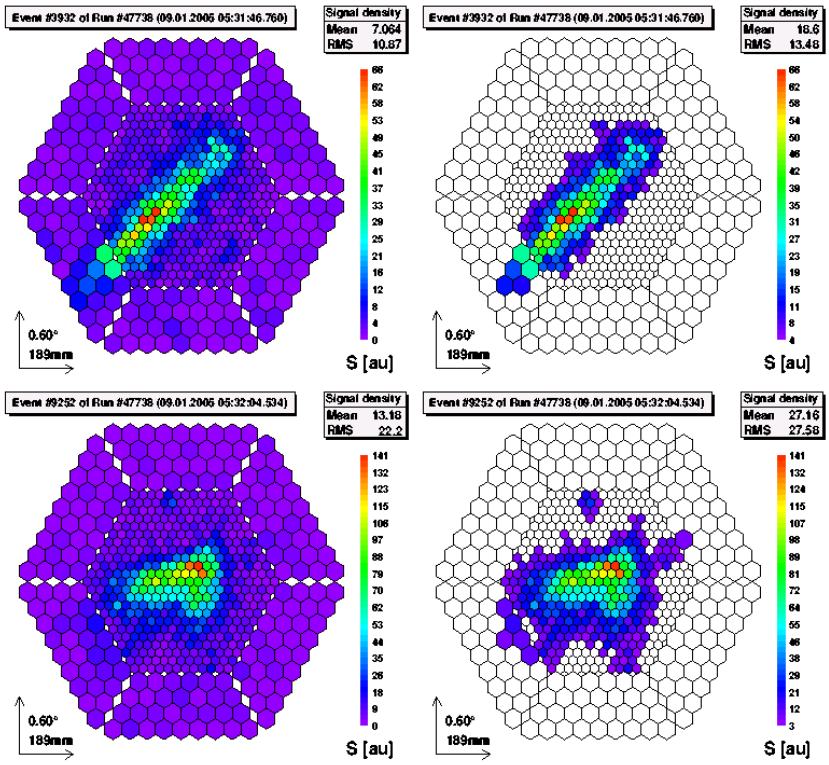

Figure 1.8: Image cleaning. Top: on the left the image of for a γ-ray shower in the camera before operating image cleaning, and the shower after image cleaning was applied, on the right side. Bottom: on the left the image of a hadron shower in the camera before operating image cleaning and the shower after image cleaning, on the right side (Bretz, 2006).

The absolute procedure take place when the number of phe for the core pixels is greater or equal to 8 ($n_{core} \geq 8$) and for the neighbor pixels greater or equal to 4 ($n_{neighbor} \geq 4$), or, in short, 8:4.

The procedure can be performed with other values for n_{core} and $n_{neighbor}$, and in this case speak about stronger cuts (like 10:5) or loser cuts (like 7:5). The relative methods of image cleaning use the pedestal noise for the rejection condition too, and one uses $n_{core} \cdot \theta_{ped}$ instead of n_{core}, and $n_{neighbor} \cdot \theta_{ped}$ for $n_{neighbor}$, with θ_{ped} the pedestal RMS.

In Fig. 1.8 the image cleaning is exemplified for a γ shower and a hadron shower. On the left the shower before the image cleaning and on the right, the shower after image cleaning.

1.5.4 Hillas parameters and γ/hadron separation

After imagine cleaning, the camera is left over with a multitude of shower images. To determine if a signal of VHE γ-rays was observed during the observation or not, one needs to know what kind of forms the γ-rays will have in the camera to separate them from other particles induced showers, after which one needs to decide which γ-rays come from the source and which not. In the first case one needs to parameterize the shower images, whereas in the last case one uses the shower's direction and arrival time.

The parametrization for showers was first introduced, in the middle of the '80, by Hillas (1983). The new parameters helped to identify the γ showers from the hadronic showers. The compact form of the γ showers produce an elliptical form in the camera. Therefore, the Hillas parameters describe the ellipse and its position in the camera. The most important parameters are:

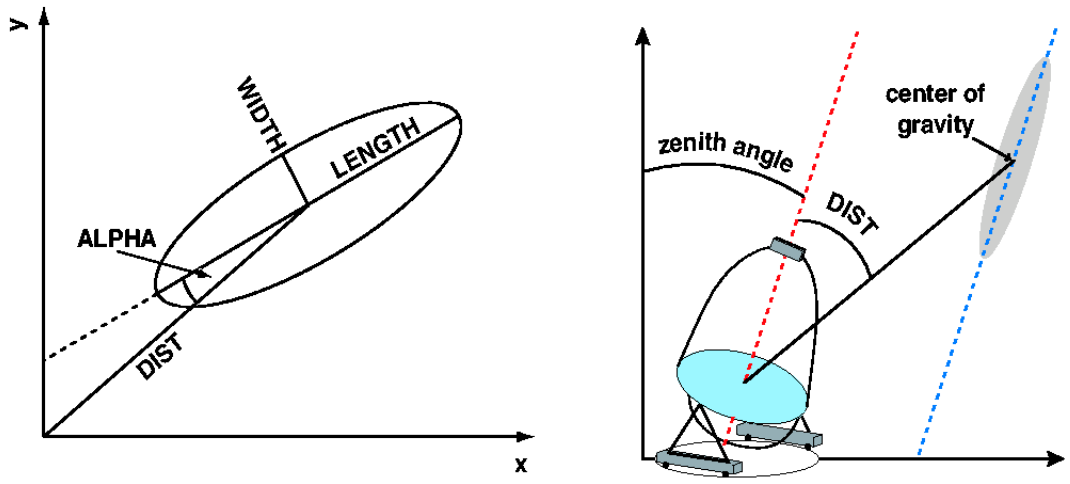

Figure 1.9: The Hillas parameters. On the left parameters that describe the shower as it appears in the camera; on the right, parameters that describe the shower seen relative to the telescope (Wagner, 2006).

- Size – the number of phe from all the pixels forming the shower image;
- Length – the lengths of the shower along the major axis of the ellipse;
- Width – the width of the shower along the minor axis of the ellipse;
- Center of Gravity (COG) – the brightest point of the light content in the shower image;
- Dist – distance of COG from the position of the source in the camera.
- M_3 – third moment of the distribution along the major axis

The difficulty differentiating between the γ showers and the other types of showers, i.e. hadronic or background, starts at low energies where the showers have similar shapes. Moreover, because it is not possible to identify single events, only the distribution of different types of showers can be compared. Monte Carlo simulations of γ showers offer information about their distribution relative to different Hillas parameters to define cuts between them and hadron showers. But not all Hillas parameters will turn out to be suitable for separation between γ induced showers and hadronic induced showers. On the other hand, one can not use single Hillas parameters for a separation cut, as the energy is spread in several of the Hillas parameters. Thus, one has a collection of cuts used to separate the γ showers from hadronic showers and the background.

One way to fulfill this, starts with the so called *Area* cut. The area, A, of the shower is define as

$$A = \pi \cdot Length \cdot Width. \tag{1.13}$$

If one plots the distribution of the area parameter for γ-ray (in red) and background (in black) relative to Size, as shown in Fig. 1.10, one sees a clear separation between the two distributions. The green line is a parabolic parametrization of the cut. In this way an efficient separation is delivered down to $\sim$ 50 GeV which makes this cut the most important one. However, the cut is insensitive to the direction of the incoming photons in the camera.

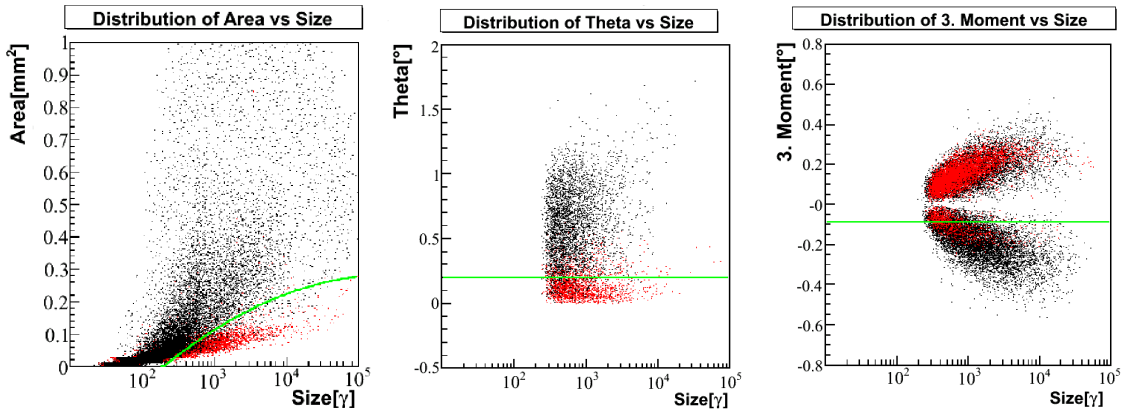

Figure 1.10: The cuts used for the γ/hadron separation of showers. The black points represent Off-data, whereas the red points are γ-ray showers from Monte Carlo simulation. The green line represents the cut used to discriminate between the two distributions (Riegel, 2005).

Photons from a source will show in the camera a common direction relative to the photons which belong to the background and therefore have an isotropic distribution of their direction. One can use this information to reconstruct the source position for every shower allowing a cut of all photons which do not point to the source position in the camera. This is done with the help of a new parameter (ϑ) which gives the distance from the reconstructed source position in the camera to the camera center. The distribution of γ shower and background versus *Size* is shown in Fig. 1.10. Again, the green line represents the cut used to separate the γ showers from background.

However, the ϑ-cut is not able to differentiate between showers which point in one direction along the shower axis or the opposite. For this, the third moment is used which gives the deviation of the *Length* and the *Width* distribution of the γ shower and describes the asymmetry of an event in the camera. The compactness of the γ shower will imply a positive value for the asymmetry whereas the hadron shower with its spread structure has a negative asymmetry value. This is emphasized in Fig. 1.10 where the red and black points represent the γ and the background showers. The green line represents the cut done for the separation.

After the cuts have been applied, an evaluation of the remained data is undertaken to determine if a signal is obtained or not. To do this, it is assumed that all the photons are of background origin and follow a normal distribution. Then a histogram is filled with the events from the On region and Off region and verify if there is an excess of On events relative to Off events as moving in the camera toward the source position, called θ^2 cut. If the number of On-data starts to increase as one comes closer to the source position in the camera, then an excess from the background is observed. The calculation for the significance is done in units of one standard deviation, i.e. 1 σ, using the formula of (Li and Ma, 1983)

$$S = \sqrt{2}\sqrt{N_{on}\ln\left[\frac{1+\alpha}{\alpha}\left(\frac{N_{on}}{N_{on}+N_{off}}\right)\right] + N_{off}\ln\left[(1+\alpha)\frac{N_{off}}{N_{on}+N_{off}}\right]}, \tag{1.14}$$

with $\alpha = \frac{t_{on}}{t_{off}}$, and N_{on}, N_{off} number of events from the On-data and Off-data respectively. The significance is true only if $N_{on}, N_{off} > 10$.

To be sure that a signal is observed from a source, a minimum of 5 σ are imposed, i.e. a probability of ∼99.9999427% that the observed signal is not due to statistical background fluctuations.

Chapter 2

Unfolding with regularization

2.1 Why unfolding?

The main information that photons carry is energy, besides direction. The price paid to observe the photons at very high energies is the energy itself. To recover the energy it is necessary to reconstruct it from the Hillas parameters. As the reconstruction of single events is not possible, one can only reconstruct the distribution of the energy of the observed photons, i.e. how many photons within a given energy range where observed. Such a distribution is called *energy spectrum*. From theoretical predictions it is know that the spectra of VHE sources should be in form of power laws.

The reconstruction process of nonmeasurable characteristics from measured data is called unfolding. This is not the only way one can compare measured results with theoretical predictions. A specific experiment could fold the theoretical prediction to include the alteration of the detector to the observed data and thus to compare directly with the measured data. This way of comparing the measurement with the theoretical prediction is even simpler than unfolding and comparing with the original prediction. Then, why should one use unfolding at all?

There are several reasons why unfolding should be used. The main reason is that unfolding allows a comparison of results from different experiments. Because of the individuality of every detector, each experiment will show a different alteration. The alteration becomes even more predominant if the comparison is done between experiments with single detectors and those with multiple (stereoscopic) detectors.

Another reason is that with new data, new theoretical models are developed. Since the theoretical development is not parallel with the experimental development (like improvements of the camera, mirror dish and others), it can happen that the procedure to fold the theoretical prediction for a specific experiment is no longer available, which makes it impossible to compare older measurements with newer theoretical predictions. Another point for unfolding is that, in the case of image reconstruction like the one treated here, unfolding can reveal certain features which may not be possible to recognize in the uncorrected distribution.

2.2 Statement of the problem

The purpose of any experiment is to measure some physical observable, x, and to determine the distribution it follows, $f(x)$. Every measurement will give a set of values of the physical observable which can be seen as a random sample from the distribution $f(x)$. The difficulty arises in the determination of the structure of $f(x)$ starting only from the set of values that where measured. Moreover, it is common that the physical observable, x, itself cannot be observed directly, and thus the experiment will measure other quantities related to it, y.

Unfolding has to overcome two different problems of the detector: finite resolution and limited acceptance.

- Finite resolution: the detector cannot measure with infinite precision, but there is a smallest non vanishing quantity (depending on the detector). This quantity defines a resolution window, such that it is impossible to differentiate between measured data casted inside it. This will imply a smearing of the initial observable data. The only way to look inside the resolution window is, statistically, by taking a distribution for the observed data.

- Limited acceptance: since the probability to observe an event is smaller than 1, a loss in the number of events that can be observed, is expected. This happens in general at the end of the range of a physical observable where events are lost due to strong trigger conditions (to suppress background) or/and data analysis (cuts).

Because of the problems specified before, the physical observable, x, will be changed into a measurable observable, y, with a new distribution, $g(y)$. Indirect observation changes both the dimension of x (if x is one-dimensional, y will be multi-dimensional) and its distribution, whereas finite resolution and limited acceptance will change only the distribution.

Mathematically, the unfolding problem can be formulated as a Fredholm integral equation of the first kind[1]

$$g(y) = \int A(y,x)f(x)dx + b(y), \tag{2.1}$$

with $f(x)$ the true distribution, $g(y)$ the observed distribution, $b(y)$ the distribution of the background and $A(y,x)$ the kernel or the response of the detector.

Thus, the unfolding problem consists of determining $f(x)$ when all the other functions are known. Solutions of equation (2.1) depend strongly on the accuracy of the data and the form of the kernel (Phillips, 1962). Due to statistical errors, the measured data, $\widehat{g}(y)$ and $\widehat{b}(y)$, are not accurate, which requires a reformulation of equation (2.1) as

$$\widehat{g}(y) + \epsilon_g(x) = \int A(y,x)f(x)dx + \widehat{b}(y) + \epsilon_b(x). \tag{2.2}$$

with $\epsilon_g(x)$ and $\epsilon_g(x)$ the statistical errors for the data and background.

Since $A(y,x)$ contains all the changes of the detector on the observed distribution $f(x)$, it is important to know it as good as possible. A theoretical form of $A(y,x)$ is quite difficult if not impossible to determine, so the most at hand solution is given by Monte Carlo simulations, in which the true distribution $f(x)$ is already known. Monte Carlo simulations allow the generation of the measured distributions $g(y)$ and $b(y)$ at the same time, if background is simulated too.

Statistical errors of the measured data impose a set of solutions for equation (2.2). Unfolding means now to find out $f(x)$ from the set of possible solutions, which is a difficult task if no additional structure on $f(x)$ is given. If we assume that $f(x)$ is given by a smooth function, then the unfolding

[1] The general Fredholm integral equation is given as $h(y)f(y) + \int A(y,x)f(x)dx = g(y)$

solution can be searched in the set of all possible solutions as the smoothest function in some sense, i.e. smoothness depends on the information of the particular problems.

In general, both variables x and y have discrete values, so in what follows the discrete forms of equation (2.1), respectively equation (2.2) are presented

$$g_i = \sum_{j=1}^{m} A_{ij} f_j + b_i \quad \text{and} \quad \widehat{g}_i + \epsilon_{g,i} = \sum_{j=1}^{m} A_{ij} f_j + \widehat{b}_i + \epsilon_{b,i} \tag{2.3}$$

where A is a $n \times m$ matrix and $g_i, i = 1, ..., n$, $f_j, j = 1, ..., m$. Equation (2.3) introduces a mesh on which the solution is calculated. The finer the mesh is, the better the solution will be, but if the mesh gets too fine, the solution will be worse. So the problem of how fine the mesh should be depends on the accuracy of $\widehat{g}$.

If the effect of finite resolution is not predominant, unfolding reduces to a simple correction (*factor* method). In this case A is a diagonal matrix, which ensures that the correction factor does not depend on the Monte Carlo inputs used. The distribution, $\overline{f}$ used for the simulation will generate a response of the detector (the Monte Carlo measured data), which will be filled in an histogram, $\overline{g}$. The elements of the matrix A will be the binwise ratio $\overline{g}_j/\overline{f}_j$ representing the acceptance probability for bin j. With all this specified, the correction of the measured bin content, $\widehat{g}_j$, is given by

$$\widehat{f}_j = \widehat{g}_j \cdot \left(\frac{\overline{f}_j}{\overline{g}_i} \right). \tag{2.4}$$

In general, the unfolding process has also to deal with finite resolution too, which will make it impossible to determine a simple algebraic solution of equation (2.3) since the matrix A is not always a square matrix and dose not have an inverse. In the case when it is possible to determine the inverse of A, the solution

$$\widehat{f} = A^{-1} \cdot \widehat{g}, \tag{2.5}$$

is subject to large fluctuation, as can easily be seen if one calculates the mean value for $\widehat{f}$ (unbias, i.e $E(\widehat{g}) = A \cdot \widehat{f}$)

$$E(\widehat{f}) = E(A^{-1} \cdot \widehat{g}) = A^{-1} \cdot E(\widehat{g}) = A^{-1} \cdot A \cdot \widehat{f} = f, \tag{2.6}$$

and the variance

$$V(\widehat{f}) = A^{-1} \cdot V(\widehat{g}) \cdot A^{-1}. \tag{2.7}$$

Thus, the inverse A^{-1} will induce high values for the variance which imply high propagation errors. An example of such fluctuation is shown in Fig. 2.1. To be able to reduce the high values in the variance, which represents the statistical error one needs to take a small bias effect, which represents systematic errors (Cowan, 1998).

2.3 The two unfolding methods

Not all measured data can be used for unfolding. It is required that only measured variables that correlate with the observable one is interested in, x, should be chosen. Every variable will have its specific correlation and range of correlation with x. The more variables correlate, the more the estimation ability for x increases and, at the same time, the correlation domain magnifies.

There is not a unique way to estimate x from measured variables. In Gamma Astronomy two such ways of estimation are used: *direct* and *probability* estimation.

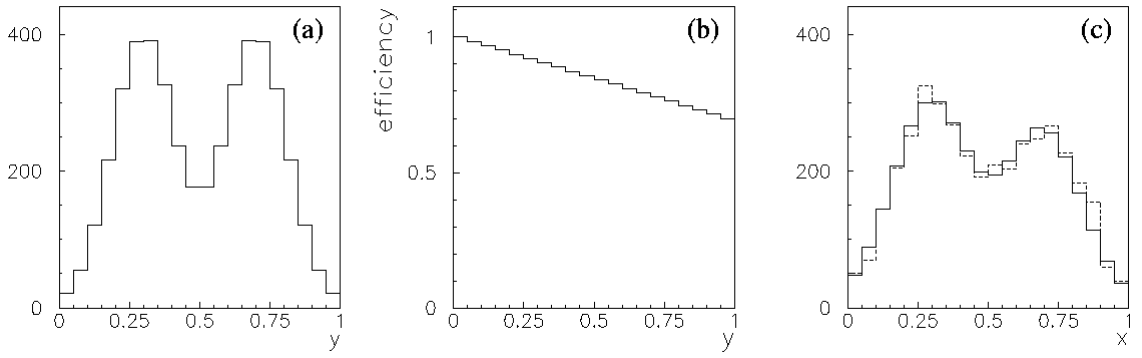

Figure 2.1: Illustration for deformation of data by a detector: (a) the known distribution of the data as used in Monte Carlo, (b) the alteration effect due to the detector (or the matrix A), (c) the distribution of the Monte Carlo events as seen in the detector (solid line) and observed (dashed) (Cowan, 1998).

2.3.1 Direct estimation

In this case, x is estimated through a formula which encapsulates the correlating variables to deliver x_{est}, i.e. the estimation is done for every individual event.

The response matrix A will represent a fraction of events which migrate from a bin j of the histogram of x into a bin i of the histogram of x_{est}. This property of A of migrating events between histograms dose not account for losses due to limited acceptance, trigger, selection cuts etc., so after unfolding corrections need to be done.

A is determined from a two-dimensional plot of the number of reconstructed Monte Carlo events in the $x_{est} - x$ plane, which were analyzed in the same way as the measured distribution g. Moreover, it is assumed that (Albert and et al., 2007)

$$\sum_{i=1}^{m} A_{ij} = 1, \quad \forall j. \tag{2.8}$$

The bin number for x and x_{est} can be chosen independent of each other, so, in general, A is not a square matrix and a solution by inversion is not possible. The unfolding process in this case becomes the minimization of the least-square expression

$$\chi_0^2 = (g - A \cdot f)^T \cdot C^{-1} \cdot (g - A \cdot f), \tag{2.9}$$

which is a solution for (2.3). C in the expression above is the covariant matrix of g.

Two cases can be distinguished:

- $n < m$ (underconstrained): The Gram matrix of A, $\mathcal{A} = A \cdot A^T$, is invertible and a particular solution, f^u, can be written as
$$f^u = A^T \cdot \mathcal{A}^{-1} \cdot g. \tag{2.10}$$
If $n \neq m$, then the solutions $f = f^u + f_{\overline{u}}$ form a vector space of $n - m$ dimension, where $A \cdot f_{\overline{u}} = 0$. Else (2.10) can be rewritten simply as
$$f^u = A^T \cdot \mathcal{A}^{-1} \cdot g = A^{-1} \cdot g, \tag{2.11}$$

and f^u is the only solution. In both cases $A \cdot f = A \cdot f^u = Y \Rightarrow \chi_0^2 = 0$. All solutions are independent of the covariance matrix C and from (2.8), the total number of events which remain unchanged is

$$\sum_i g_i = \sum_i \sum_j A_{ij} \cdot f_j^u = \sum_j f_j^u. \tag{2.12}$$

- $n > m$ (overconstrained): The minimization is done by varying f, which gives the solution

$$f^o = H^{-1} \cdot A^T \cdot C^{-1} \cdot g, \tag{2.13}$$

with $H = A^T \cdot C^{-1} \cdot A$. In this case the solution will depend on the covariance matrix and the minimal value is given by

$$\chi_0^2 = (g - A \cdot f^o)^T \cdot C^{-1} \cdot (g - A \cdot f^o). \tag{2.14}$$

For the square case, the solution can be written as $f^o = A^{-1} \cdot g$.

Instead of the least-square method, an implicit technique of minimization is possible by using parametric functions for f such as $f_k(q) = \psi(x_k; q)$ with $q = (q_1, ..., q_l)$. The minimization of χ_0^2 in (2.9) becomes now the minimization of

$$\chi_0^2 = \sum_{i,j=1}^{n} \left(g_i - \sum_{j=1}^{m} A_{ij} \cdot f_j(q) \right) \cdot (C^{-1})_{ij} \cdot \left(g_j - \sum_{k=1}^{m} A_{jk} \cdot f_k(q) \right), \tag{2.15}$$

with respect to parameters q. Because $l < n$ the problem is overconstrained. The minimization condition $\frac{\partial \chi_0^2}{\partial q} = 0$ can be computed analytically following the procedure described by (2.13-2.14) for a broad range of cases. In general, the parametrization can be written as

$$\psi(x_k; q) = \Phi_k(q) \cdot T_{\text{eff}} \cdot \Delta(x^k) \cdot B_{cor}^k, \tag{2.16}$$

where T_{eff} is the effective observation time, $\Delta(x^k)$ is the width of the $k-$bin of x, B_{cor}^k is the correction factor, and

$$\Phi_k(q) = \frac{1}{\Delta(x^k)} \int_{\Delta(x^k)} \Phi(x, q) dx, \tag{2.17}$$

where $\Phi(x, q)$ is the assumed parametrization for the differential spectrum for x. In both cases the solutions are subject to errors and fluctuations.

2.3.2 Probability estimation

The measured variables that correlate with x are now used to calculate the probability of a set of events that belongs to different bins of x. The input variables to calculate the probability are in general used individually, but it is also possible to use combinations of them. In principle, it is not excluded to use the estimation formula for x from the direct estimation as an input variable to calculate the probability, but this will not imply an improvement automatically. The reason for this is that the formula is true for single events, whereas the calculation of the probability relies on a set of events. The only contribution one can obtain from such a variable is a better correlation. But a better estimation is only achieved if the correlation surpasses the statistical error which is generally not the case.

In this case, A will denote a probability matrix describing the fraction of events in histogram bin i of $g(y)$, if the true value x is from histogram bin j of $f(x)$ (Blobel, 1984).

In order to solve equation (2.1), a discretization is performed, starting with a parametrization of f

$$f(x) = \sum_{j=1}^{m} a_j p_j(x), \tag{2.18}$$

where $p_j(x)$ are cubic B-spline functions. From (2.1) and (2.18) one obtains

$$\int_a^b A(y,x) f(x) dx = \sum_{j=1}^{m} a_j A_j(y) \;\text{ with }\; A_j(y) = \int_a^b A(y,x) p_j(x) dx, \tag{2.19}$$

which yields

$$g(y) = \sum_{j=1}^{n} a_j A_j(x) + b(y). \tag{2.20}$$

To complete the discretization process, an integration of (2.20) is required between the limits of the chosen bins

$$g_i = \int_{y_{i-1}}^{y_i} g(y) dy, \quad A_{ij} = \int_{y_{i-1}}^{y_i} A_j(y) dy, \quad b_i = \int_{y_{i-1}}^{y_i} b(y) dy, \tag{2.21}$$

which gives (2.3). The elements of the matrix A are calculated by adding Monte Carlo events with true value x, to the histogram of $A_j(y)$, with a weight proportional to $p_j(x)$. Since $p_j(x)$ can be regarded as probabilities, we impose the following conditions

$$p_j(x) \geq 0, \quad \sum_{j=1}^{m} p_j(x) \equiv 1. \tag{2.22}$$

The second condition in (2.22) defines a local normalization, so for the normalization of the resulting distribution, $f(x)$, one needs to define a global weight for the Monte Carlo events.

The unfolding problem will be to determine the m parameters a_j from the measured data which are in the form of histogram bin contents $\widehat{g}_i$, $i = 1, ..., n$. The data ,$\widehat{g}_i$, will follow a certain probability distribution, and the probability to observe $\widehat{g}_i$ when the mean value is g_i, is given by $P(\widehat{g}_i|g_i)$. By multiplying the probabilities, the Likelihood function is obtained

$$L(a) = \prod_{i=1}^{n} P(\widehat{g}_i|g_i). \tag{2.23}$$

Its maximum will deliver the coefficients a_i. Anyway, in practice, one prefers to solve an equivalent minimization of the following function

$$S(a) = -\sum_{i=1}^{n} \ln P(\widehat{g}_i|g_i) \;\; \Rightarrow \;\; S(a) = \sum_{i=1}^{n} g_i - \sum_{i=1}^{n} \widehat{g}_i \ln g_i. \tag{2.24}$$

The implication is true only if $\widehat{g}$ follows the Poisson distribution. In order to be able to apply usual matrix methods, $S(a)$ is approximated with a quadratic function

$$S(a) = S(\widetilde{a}) - (a - \widetilde{a})^T \cdot G + \frac{1}{2}(a - \widetilde{a})^T \cdot H \cdot (a - \widetilde{a}), \tag{2.25}$$

where $\widetilde{a}$ is an approximative solution of $S(a)$ and G and H are the gradient, resp. the Hessian. With $\widehat{g}_i$ calculated for $\widetilde{a}$, G and H can be computed as follows

$$G_j = -\frac{\partial S}{\partial a_j} = \sum_{i=1}^{n} \widehat{g}_i \frac{A_{ij}}{g_i} - \sum_{i=1}^{n} A_{ij}, \quad H_{jk} = \frac{\partial^2 S}{\partial a_j \partial a_k} = \sum_{i=1}^{n} \widehat{g}_i \frac{A_{ij} A_{ik}}{g_i^2}. \tag{2.26}$$

A necessary condition for the minimum is given by $\nabla S = 0$, which results in the following equation $-G + H \cdot (a - \widetilde{a}) = 0$, with the solution

$$a_{app} = \widetilde{a} + H^{-1} \cdot G. \tag{2.27}$$

The approximation $\widetilde{a}$ implies a search for the minimum using several iterations. The convergence of the method is assured if actual changes of $S(a)$ and expected changes of $S(a)$

$$(\Delta S)_{exp} = -\frac{1}{2}(a_{app} - a)^T \cdot G, \tag{2.28}$$

are small compared to 1 during an iteration. The stability is given by the following minimization problem

$$\min_t S(\widetilde{a} + t(a_{app} - \widetilde{a})), \tag{2.29}$$

at every iteration. Thus, the minimum is given by

$$a_{min;k+1} = t_{min;k+1} \cdot a_{app} + (1 - t_{min;k+1}) \cdot a_{min;k}, \quad a_{min,1} = \widetilde{a}. \tag{2.30}$$

Since $S(a)$ was approximated by a quadratic function near the solution, i.e. t_{min} close to 1, the solution $\widehat{a}$ is reached in few steps.

If the Poisson distribution is approximated by a Gaussian distribution, $S(a)$ will have the following form

$$S(a) = \frac{1}{2} \sum_{i=1}^{n} \frac{(\widehat{g}_i - g_i)^2}{\sigma_i^2}, \tag{2.31}$$

with $\sigma_i^2 = g_i$. In this case, as easily can be seen, the minimum is given by the least square principle. The gradient and the Hessian are

$$G_j = \sum_{i=1}^{n} A_{ij} \frac{\widehat{g}_i - g_i}{\sigma_i^2}, \quad H_{jk} = \sum_{i=1}^{n} \frac{A_{ij} A_{ik}}{\sigma_i^2}. \tag{2.32}$$

$S(a)$ is quadratic in this case, so the solution can be directly computed as

$$\widehat{a} = H^{-1} \cdot G. \tag{2.33}$$

The Gaussian distribution being only an approximation, the result obtained by (2.33) serves as an input for the Poisson solution.

To compute the covariant matrix for $\widehat{a}$, which is a diagonal matrix due to uncorrelated data events, a weight matrix $W = V^{-1}(\widehat{a})$ is used, which is also diagonal with $W_{ii} = \frac{1}{\sigma_i^2}$. The gradient and the Hessian in matrix notation are $G = A^T \cdot W \cdot \widehat{g}$ and $H = A^T \cdot W \cdot A$, and the solution is

$$\widehat{a} = H^{-1} \cdot G = (A^T \cdot W \cdot A)^{-1} \cdot A^T \cdot W \cdot \widehat{g} = A^{-1} \cdot \widehat{g}. \tag{2.34}$$

Finally, the covariant matrix will be

$$V(\widehat{a}) = (A^T \cdot W \cdot A)^{-1} \cdot A^T \cdot W \cdot W^{-1} \cdot W \cdot A \cdot (A^T \cdot W \cdot A)^{-1} = H^{-1}. \tag{2.35}$$

The same result applies for the case of the Poisson distribution, which is a good approximation for low statistics and true for the asymptotic case of high statistics.

As in the case of *direct estimation*, the solution will be subject to errors and fluctuations. In what follows, one tries to show where these errors come from. Since H is a symmetric positive definite matrix, the spectral theorem gives the following diagonal form

$$D = O_1^T \cdot H \cdot O_1, \tag{2.36}$$

with $d_{ii} \in \mathbb{R}_+$, $\forall i$ and O_1 orthogonal matrix. The eigenvalues of H can be arranged in decreasing order, $d_{11} > d_{22} > ... > d_{mm}$ (after index rearrangement), which makes it easier to notice the ratio between the highest and the lowest eigenvalues. Using the transformation

$$a = O_1 \cdot D^{-\frac{1}{2}} \cdot a_1, \tag{2.37}$$

(2.25) becomes

$$S(a_1) = -a_1^T \cdot D^{-\frac{1}{2}} \cdot O_1^T \cdot (H \cdot \widetilde{a} + G) + \frac{1}{2} a_1^T \cdot a_1. \tag{2.38}$$

From $\nabla S = 0$ follows

$$\widehat{a}_1 = D^{-\frac{1}{2}} \cdot O_1^T \cdot (H \cdot \widetilde{a} + G). \tag{2.39}$$

The advantage of using transformation (2.37) is that $V(\widehat{a}_1) = I$, which means that the components of the vector $\widehat{a}_1$ are statistically independent and have a variance of 1. This will allow us to test the significance of every component of $\widehat{a}_1$ independently, which is useful if some components are small compared to 1. These components can be neglected (cut) from the solution and they are exactly those components that induce high errors and fluctuations in the full solution, which can easily be seen from

$$\widehat{a} = \sum_{j=1}^{m} \frac{\widehat{a}_{1;j} o_j}{d_{jj}}. \tag{2.40}$$

So, the unitary variance of the components of $\widehat{a}_1$ and the small eigenvalues d_{jj} give a large weight factor.

2.4 Unfolding with regularization

Large errors and fluctuations are known difficulties of the unfolding problem. In the '60s, a strategy was developed to overcome these difficulties. The idea of the strategy is to add to the function one is maximizing or minimizing, the magnitude of the fluctuation. Then the same procedures as in the previous part can be applied for the new function. This enables to search a solution with a given degree of smoothness or with other wanted properties. How the magnitude of the fluctuation added to the initial function will look, depends on the way the fluctuation disturbs the full solution and on the way the solution should look. A constant is attached to the magnitude of the fluctuation, such that it will permit an adjustment to the contribution of the regularization term. This regularization constant will indicate how much the solution will be biased.

2.4.1 Direct method

The regularization is more efficient in the underconstrained case. For the overconstrained case, it shows improvement if some of the data have larger errors then others (e.g. different days of observation of a given source).

Regularization will imply the addition of an extra term to the magnitude of fluctuation $Reg(f)$, and (2.9) becomes

$$\chi^2 = \frac{w}{2} \cdot \chi_0^2 + Reg(f), \tag{2.41}$$

where w is the regularization constant. If w has large values, the effect of regularization is small, whereas for small values of w the regularization effect is high. Depending on the form of $Reg(f)$ two cases are frequently used:

- Tikhonov's method: the regularization term is given as

$$Reg(f) = \sum_{j=1}^{m} \left(\frac{d^2 f}{dx^2} \right)_j^2, \tag{2.42}$$

  where one can use different approximations for the derivative. The MAGIC collaboration uses

$$\left(\frac{d^2 f}{dx^2} \right)_j^2 = 2 \cdot \left(\frac{f_{j+1} - f_j}{f_{j+1} + f_j} - \frac{f_j - f_{j-1}}{f_j + f_{j-1}} \right). \tag{2.43}$$

  For a chosen value of w and a specified $Reg(f)$, the minimum of χ^2 is computed analogue to χ_0^2.

- Schmelling's method: the regularization term is defined as

$$Reg(f) = \sum_{j=1}^{m} s_j \cdot \ln \frac{s_j}{\epsilon_j}, \tag{2.44}$$

  with s_j being the normalized distribution of f

$$s_j = \frac{f_j}{\sum_{i=1}^{m} f_i}. \tag{2.45}$$

  For this kind of regularization one needs an additional condition: the distribution of f has to be positive definite.

A different way of unfolding is to suppress the small eigenvalues λ_l of $\mathcal{A}$ by a factor $\zeta(\lambda_l)$, so $\mathcal{A}$ can be written as

$$\mathcal{A} = \sum_{\lambda_l \neq 0} \zeta(\lambda_l) \cdot \lambda_l \cdot y_l y_l^T, \tag{2.46}$$

with y_l eigenvectors corresponding to the eigenvalues λ_l. The inverse of $\mathcal{A}$ is

$$\mathcal{A}^{-1} = \sum_{\lambda_l \neq 0} \frac{\zeta(\lambda_l)}{\lambda_l} \cdot y_l y_l^T. \tag{2.47}$$

One can chose ζ sufficient arbitrary. An index can be associated such that $\zeta(\lambda_l; i) \to 1$ for $i \to \infty$.

The unfolding process can be done also in an iterative way. In this case, the effect of regularization is that the process stops before the final minimum is reached. Thus, for the underconstrained case the iteration can be written as

$$B^{i+1} = B^i - \tau \cdot (\mathcal{A} \cdot B^i - g), \tag{2.48}$$

with $B = \mathcal{A} \cdot g$ and τ the relaxation constant, which should lie between 0 and $\frac{2}{\lambda_{max}}$, where λ_{max} is the largest eigenvalue of $\mathcal{A}$. The solution of the unfolding process can be expressed as $f^i = A^T \cdot B^i$, with B^i given by

$$B^i = (1 - \tau \cdot \mathcal{A})^i \cdot B^0 + \tau \cdot \sum_{j=0}^{i-1} (1 - \tau \cdot \mathcal{A})^j \cdot g, \tag{2.49}$$

and B^0 being the starting point for B. The iteration method is equivalent to the suppression method and for (2.48) $\zeta(\lambda_l; i)$ can be computed as

$$\zeta(\lambda_l; i) = \begin{cases} 1 - (1 - \tau \cdot \lambda_l)^i, & \text{if } B^0 = 0 \\ 1 - (1 - \tau \cdot \lambda_l)^i + (1 - \tau \cdot \lambda_l)^i \cdot \lambda_l, & \text{if } B^0 = g. \end{cases} \tag{2.50}$$

2.4.2 Probability method

In this case the magnitude of the fluctuation is given as the total curvature of f

$$r(a) = \int [f''(x)]^2 \, dx. \tag{2.51}$$

The regularization term is now added to $S(a)$, such that the new function to be minimized is

$$R(a) = S(a) + \frac{1}{2} \cdot \tau \cdot r(a). \tag{2.52}$$

As before, for very small values of τ the regularization effects are negligible, whereas for very large values the regularization term will dominate the solution.

At this point, the B-spline parametrization of f offers a major advantage since it permits writing the regularization term as a quadratic function of a

$$r(a) = a^{\mathrm{T}} \cdot \mathcal{R} \cdot a, \tag{2.53}$$

where $\mathcal{R}$ is a constant symmetric positive semidefinite matrix, i.e. $r(a) \geq 0, \forall a \in \mathbb{R}^m \setminus \{0\}$. Except some constants which can be absorbed in the regularization constant, $\mathcal{R}$ has, for cubic spline, the following form

$$\begin{pmatrix} 2 & -3 & 0 & 1 & 0 & 0 & \dots \\ -3 & 8 & -6 & 0 & 1 & 0 & \dots \\ 0 & -6 & 14 & -9 & 0 & 1 & \dots \\ 1 & 0 & -9 & 16 & -9 & 0 & \dots \\ 0 & 1 & 0 & -9 & 16 & -9 & \dots \\ 0 & 0 & 1 & 0 & -9 & 16 & \dots \\ \vdots & \vdots & \vdots & \vdots & \vdots & \vdots & \ddots \end{pmatrix}. \tag{2.54}$$

Using the transformation (2.37) the expression to be minimized can be expressed as

$$R(a_1) = -a_1^T \cdot D^{-\frac{1}{2}} \cdot O_1^T \cdot (H \cdot \widetilde{a} + G) + \frac{1}{2} \cdot a_1^T \cdot (I + \tau \cdot \mathcal{R}_1) \cdot a_1, \tag{2.55}$$

with $\mathcal{R}_1 = D^{-\frac{1}{2}} \cdot O_1^T \cdot \mathcal{R} \cdot O_1 \cdot D^{-\frac{1}{2}}$. In order to compute the regularized solution, one uses a transformation. To this purpose, $\mathcal{R}$ is diagonalized

$$\mathcal{T} = O_2^T \cdot \mathcal{R} \cdot O_2, \tag{2.56}$$

with eigenvalues arranged in increasing order $t_{11} \leq t_{22} \leq ... \leq t_{mm}$ and the transformation is defined as

$$a_1 = O_2 \cdot a'. \tag{2.57}$$

Due to the orthogonality of O_2 one can see that $a_1^T \cdot a_1 = a'^T \cdot a'$. Thus, (2.55) can be rewritten as

$$R(a') = -a'^T \cdot O_2^T \cdot D^{-\frac{1}{2}} \cdot O_1^T \cdot (H \cdot \widetilde{a} + G) + \frac{1}{2} \cdot a'^T \cdot (I + \tau \cdot \mathcal{T}) \cdot a'. \tag{2.58}$$

From $\nabla R = 0$, one finds the solution

$$\widehat{a}' = (I + \tau \cdot \mathcal{T})^{-1} \cdot O_2^T \cdot D^{-\frac{1}{2}} \cdot O_1^T \cdot (H \cdot \widetilde{a} + G). \tag{2.59}$$

If we denote with $\overline{a}'$ the full solution, i.e. without regularization ($\tau = 0$), the regularized solution can be expressed as the full solution multiplied by a correction factor

$$\widehat{a}'_j = \frac{1}{1 + \tau \cdot t_{jj}} \overline{a}'_j. \tag{2.60}$$

As long as $t_{jj} \ll \tau^{-1}$, the correction factor will be close to 1. When $t_{jj} \gg \tau^{-1}$, the correction factor will vanish after a transition region. The sum of all correction factors will give the number of independent contributions to the solution

$$m_0 = \sum_{j=1}^{m} \frac{1}{1 + \tau \cdot t_{jj}}. \tag{2.61}$$

The value of m_0 must be large enough to include all significant components of $\overline{a}$. Statistically, one can set a lower limit for m_0. The covariance matrix for the regularized solution is given as

$$V(\widehat{a}') = (I + \tau \cdot \mathcal{T})^{-2} \cdot V(\overline{a}') = (I + \tau \cdot \mathcal{T})^{-2}. \tag{2.62}$$

The m_0 coefficients $\widehat{a}'_j$ will define $f(x)$, which has to be transformed in a histrogram, i.e. data points $\widehat{f_k}$, and which can be accomplished by integrating

$$\widehat{f_k} = \frac{1}{x_k - x_{k-1}} \cdot \int_{x_{k-1}}^{x_k} f(x)dx = \frac{1}{x_k - x_{k-1}} \cdot \sum_{j=1}^{m_0} \widehat{a}'_j \int_{x_{k-1}}^{x_k} p_j(x)dx. \tag{2.63}$$

How the integration limits are chosen is an important task in keeping the correlation between the data points as small as possible. One way to do this is by means of the function p_{m_0+1} which has m_0 zeros which can play the role of the integration limits.

2.5 Example

For the probability matrix A the following symmetric form is chosen, which for the 5×5 (n=5) case is expressed as (Blobel, 2002)

$$A(\varepsilon) = \begin{pmatrix} 1-\varepsilon & \varepsilon & 0 & 0 & 0 \\ \varepsilon & 1-2\varepsilon & \varepsilon & 0 & 0 \\ 0 & \varepsilon & 1-2\varepsilon & \varepsilon & 0 \\ 0 & 0 & \varepsilon & 1-2\varepsilon & \varepsilon \\ 0 & 0 & 0 & \varepsilon & 1-2\varepsilon \end{pmatrix}. \tag{2.64}$$

The data will follow the distribution

$$g(y) = y \cdot e^{-ay}, \tag{2.65}$$

with a being a free parameter. Then for $\varepsilon = 0.22$ and n=20 the full unfolded result is shown in Fig. 2.2 together with the true distribution, the unfolded distribution without regularization and the unfolded distribution with regularization. The unfolding without regularization clearly shows oscillation from the true distribution, whereas for the unfolded distribution with regularization such effects are not present any more.

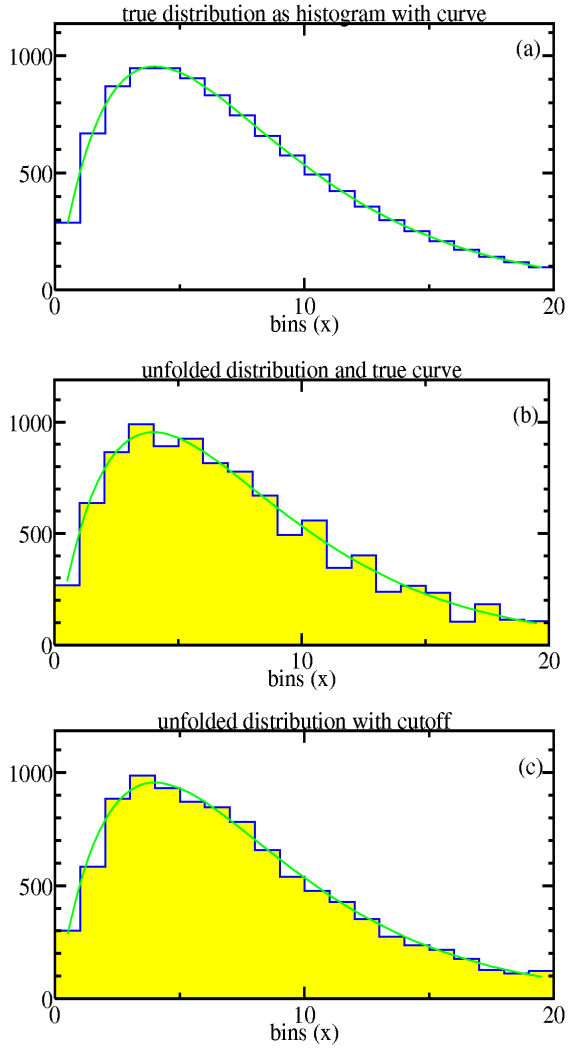

Figure 2.2: An unfolding example. Top: the true distribution of the data use for unfolding. Middle: the unfolded distribution without regularization which shows strong oscillation from the true distribution. All 20 coefficients were taken to determine the solution. Bottom: the unfolded distribution with regularization, i.e. a cut done after the 10-th coefficient. The green line represents a fit for the true distribution (Blobel, 2002).

Chapter 3

Active Galactic Nuclei

With the third generation of Atmospheric Čerenkov Telescopes, many new gamma-ray sources were discovered in the range of ~ 50 GeV to ~ 50 TeV. Although at the beginning of the Gamma-Ray Astronomy Era there were only a few known sources, nowdays, the number of them reaches nearly 100. In the same way, the number of different types of sources increased, such as pulsars and AGN, Supernovas remnants, Supernovas winds, binary systems, and others. The AGN are interesting because of two important components: they are far away and reveal the past of the universe, and the photon radiation emitted from them reaches very high energies.

Every measurement reveals some information about the object that is observed. Over the last decades, observations covering the entire electromagnetic band helped tremendously in the understanding of the structure and mechanism of AGN. However, the details that connect observations and theory are still unclear and further investigation is still needed.

3.1 The large scale structure of AGN

Galaxies are fascinating objects, but after their discovery they remained for a long time poorly understood. It was only the recent decades that a new window in understanding the formation and development of galaxies was opened. Arp's Atlas of Peculiar Galaxies (middle of the '60s) included a large number of galaxies with strange shapes (Arp, 1966), from which the Antennae galaxy is shown in Fig. 3.1 (right). Such an observation was frightening because the Hubble classification of galaxies, emphasized on the left sight of Fig. 3.1, was not sufficient anymore, but which was true as long one kept the galaxies fixed in the Hubble classification during their lifetime. It was soon recognized (Toomre and Toomre, 1972) that galaxies changed dramatically during their altering which opened the perspective to a dynamical environment for galaxies. The most important feature of this new perspective was the merging and interaction between the galaxies. From now on one could explain the elliptical galaxies as the merging of two spiral galaxies and not necessarily to look for different formations of each individual galaxy class.

At the beginning, this merging of galaxies is very violent and destroys the outer cover of the involved galaxies which explains their observed peculiar shape. But this is not the only high energetic event associated with galaxies. Already at the beginning of the '40s, C. K. Seyfert pointed that the broad emission lines (atoms in different ionization states) observed for a small percentage of galaxies, originated from the bright nuclei of the galaxy (Seyfert, 1943). Their emission lines were brighter

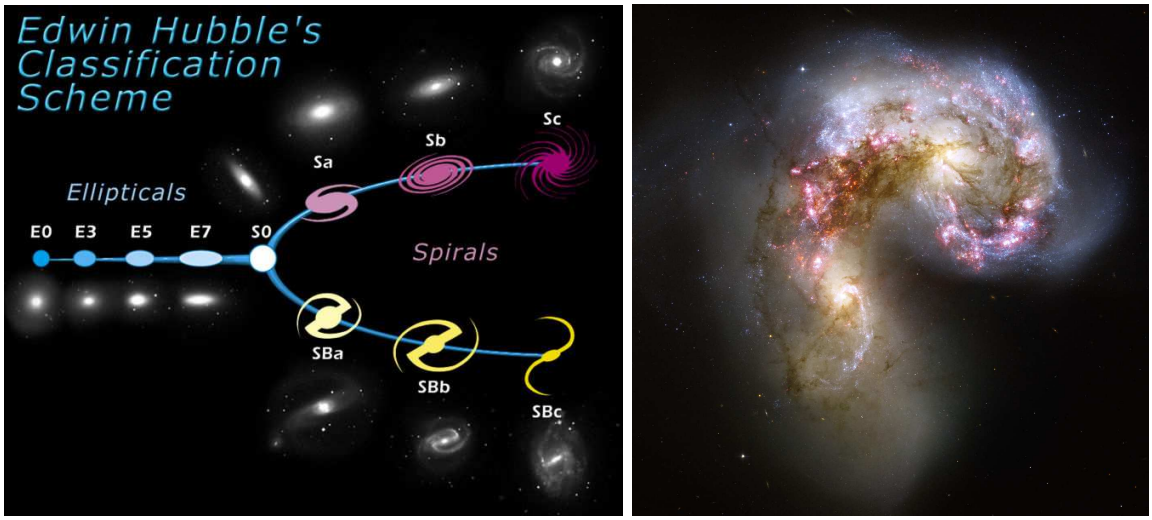

Figure 3.1: The Hubble classification of galaxies (Site, 2008) on the left side, and the Antennae-Galaxy (NASA and the Hubble Heritage Team , STScI/AURA) on the right side as an example of an irregular galaxy discovered by Arp (Arp, 1966).

then for the normal galaxies. Today such objects are called Seyfert galaxies and are divided in two categories

- *Seyfert 1 galaxies*: broad emission lines are present which include both allowed lines (H I, He I, He II) and narrower forbidden lines (like O III);
- *Seyfert 2 galaxies*: only narrow lines are present (allowed and forbidden).

Even if Seyfert galaxies are very rare, nearly 90% of them are sufficiently close to be observed by telescopes as spiral galaxies often of type Sb or SBb. Moreover, they are the most common galaxies with an active nuclei although not the only ones.

When in the middle of the '40s, radars were discovered, astronomy obtained a new tool for seeing the universe: the radio telescope. That enabled one to see in more detail the objects that were already known from the optical wavelengths. From the radio wavelengths point of view, the galaxies are divided in *broad-line* and *narrow-line*. It is the only classification that is common to both galaxies (Seyfert and radio). Seyfert galaxies are radio quiet[1], whereas radio loud galaxies are predominant in elliptical galaxies. A radio galaxy radiates its energy from a compact *core* in the nucleus of the galaxy and from a *halo* of the size of the galaxy itself or even larger. The new and surprising discovery was of *radio lobes* which are outside the galaxy and much louder then the rest of the galaxy. The lobes are connected to the galaxy via *jets* that can extend as far as Mpc (as in the case of 3C 236), thus many times the diameter of the galaxy. Loud galaxies have, generally, a one-side jet, while the quiet galaxies have typically a two-side jet. On the left of Fig. 3.2 the radio image of NGC 1097 is shown, whereas on the right side the radio structure of M87 is shown at different scales with a clear evidence of the two-side jet.

As the number of discovered radio sources increased rapidly, a simultaneous search for counterparts in optical sources became a normal task. But during the '60s, astronomers had difficulty identifying the optical objects. This difficulty came from the strange spectra of the objects which

[1]Objects with a low radio luminosity are called *quiet*, and with a high radio luminosity *loud*.

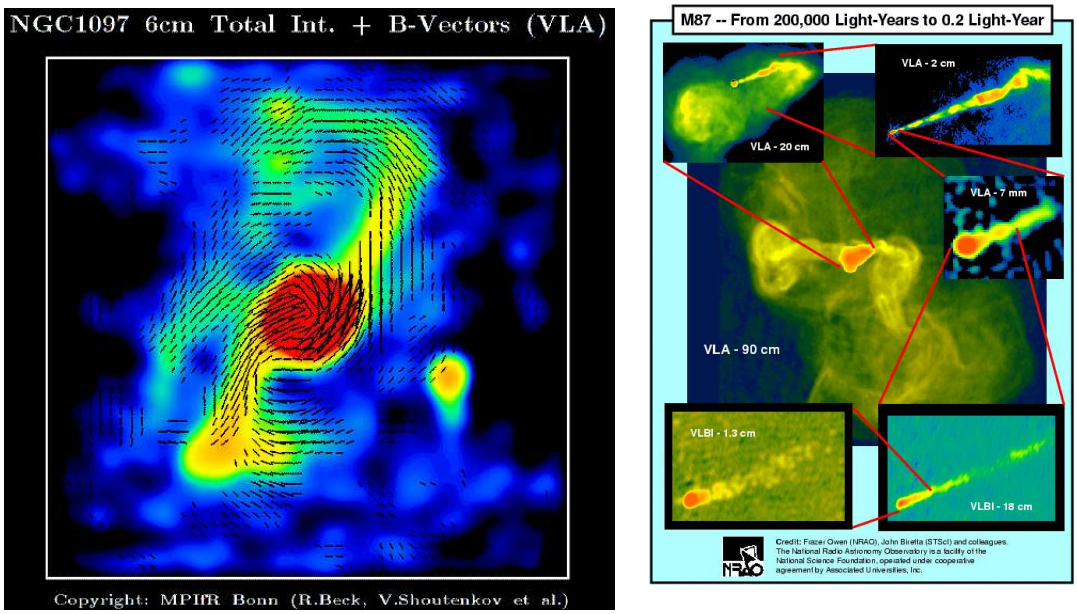

Figure 3.2: The radio structure of galaxies in the radio band. On the left NGC 1097 (Exploraciones en la Ciencia de los Sistemas Complejos, 2008) where the lines represents the structure of the magnetic field. On the right, M87 as seen in the radio at different frequencies, i.e. at different scales (F. N. Owen , NRAO).

contained broad emission lines from unknown elements or molecules. These objects were all starlike and therefore classified as quasi-stellar objects or short *quasars*. The mystery for the identification of the broad emission lines was elucidated by M. Schmidt (Schmidt, 1963) who recognized that the lines represented the normal lines but at a high redshift, like for 3C 48 with $z = 0.367$. Thus, the Hubble distance for 3C 48 is $\sim 900\ h^{-1}$ Mpc which represented one of the most distant objects in the universe at that time. Similar to radio galaxies, the emission came either from the radio lobes or from the central source in its core.

Because of the high redshift, the quasars appear in the optical band surrounded by a thin halo which, sometimes, can be resolved into a faint parent galaxy. The total luminosity of quasars is typically 5×10^{46} ergs s^{-1} which is 5 orders of magnitude higher than a normal galaxy. Compared to stars which have just a peaked spectrum, quasars have a spectrum which spans over 15 magnitudes. Around 90 % of the observed quasars are quiet and are catalogued as quasi-stellar objects (QSO). Nearly all QSO (together with quasars) have a spectrum similar to those of broad-line radio galaxies and Seyfert 1, where Seyfert 2 spectra have nearly no counterparts among QSO. The spectrum of QSO shows absorbtion lines too, which become more accentuated with higher redshift.

The energy of many QSO and quasars shows variability on a short time scale. Thus, the luminosity of the broad lines can change within days, weeks or months by a factor of 2, called high or low state . In the visible and x-ray range the variability is much shorter (hours, minutes), and are called 'flares'. QSO show polarization effects too. Some are purely polarized ($\lesssim 3\%$) for quiet and loud radio objects. Strong polarization is present for QSO and quasars with radio emission from the compact core. QSO and quasars (short AGN) with rapid variability and high polarization at visible wavelengths are classified as *blazars*. The most know blazar is BL Lacertae which was initially classified as a variable star. However, careful observation (due to the peculiar spectrum) revealed a halo with a spectrum similar to an elliptical galaxy.

The most distant quasar known today is J2329-0301 at $z = 6.43$ (Willott, 2007). Because of their

great distance, QSO and quasars reveal a picture of the young universe and thus one can assume that they represent an early stage of the formation and development of galaxies. This is sustained by the fact that the number of QSO and quasars start to change only for redshift greater then 2.

3.2 The small scale structure of AGN

It was Seyfert who observed that very few galaxies have bright nuclei which were nearly impossible to distinguish from stars. Only the association (a decade later) between the elliptical galaxy M87 and the radio source Vir A indicated that the source of the energy was the nucleus of the galaxy. A new association showed that the energy from the nuclei of galaxies was not a singular event. Even with the advantage of interferometry the radio sources could not be resolved below 1 arcsec, which implied a very compact object as the source of the radiation. With the theoretical knowledge about relativistic plasma of that time, it was possible to calculate the rest mass energy of another compact object Cyg A. Thus the minimal energy associated with relativistic electrons, protons and magnetic fields could reach $\sim 10^{58} - 10^{60}$ erg, or $\sim 10^4 - 10^6$ $M_\odot$. But with the discovery of QSO with such energies were no longer isolated cases but became more and more accepted facts.

In the middle of the '60s the idea of a very compact object in the center of galaxies that grow through accretion started to get established by Zel'Dovich and Novikov (1965). But only with the discovery of pulsars by Hewish et al. (1968) it was easier to accept black holes as natural candidates. At the beginning of the '70s the first black hole (originating from a star) was discovered in the X-ray source Cygnus X-1 (Brucato and Kristian, 1972) and it took nearly two decades longer to discover a black hole in the center of a galaxy: M87 (Harms, 1994).

The delay of finding a super massive black hole (SMBH) in the center of a galaxy comes from the fact that even if the gravitational signature of the SMBH on the motion of the surrounding matter is unique (relativistic velocities), the range of influence of the black hole is within a few Schwarzschild radii. Contrary to stars, galaxies are more far away, thus such detailed observations are very difficult to perform, even for the nearest ones. Nowadays a different strategy of observing SMBH has been developed, although uncertainties exist. At the moment, the only observational case which indicates a SMBH with an accepted statistical certainty is the Milky Way (stelar dynamics) and NGC 4258 (H_2O megamaser).

In the following, the observational techniques are described.

3.2.1 Stellar dynamics

This method relies in the development of the motion of stars which is purely gravitational. Such an observation is not a trivial task because one needs a large collection area (delivered by ground based telescopes) for the high spectral signal-to-noise ratio and high spatial resolution, which can be accomplished for example, by the Hubble Space Telescope (HST) for a handfull of sources. The difficulty of the method also includes a theoretical issue: the structure of the stellar orbits is unknown and difficult to recover from observation.

A principal model assumes that the motion of stars that surround the SMBH is governed by the gravitational potential $\Phi(\mathbf{x}, t)$ which includes all the stars. The distribution function $f(\mathbf{x}, \mathbf{v}, t)$ will give the number of stars in a given infinitesimal volume in phase-space. The distribution function follows the Boltzmann collisonless equation which states that the rate of change of the number of stars depends on the amount of inflow after the outflow is subtracted

$$\frac{df}{dt} = \nabla\Phi(\mathbf{x}, t) \cdot \frac{\partial f}{\partial \mathbf{v}}, \qquad \nabla^2\Phi(\mathbf{x}, t) = 4\pi G\rho(\mathbf{x}, t), \tag{3.1}$$

where the last equation links the gravitational potential with the total mass (stars, SMBH, dust, dark matter if present). Without any other restriction, the equations are impossible to be solved analytically. For the case of spherical, isotropic systems the distribution function only depends on one integral of motion, the total energy of the system. This implies that a one-to-one correspondence between the density distribution function can be found where the density can be calculated from measurements (assuming a central mass from which the mass for the SMBH can be derived). Once $f(\mathbf{x}, \mathbf{v}, t)$ is known, the velocity dispersion can be computed uniquely and thus a best fit to the observation for the central mass can be done. If the velocity distribution is not isotropic then, one needs two or even three integrals of motion.

3.2.2 Gas dynamics from water maser

Water masers are the result of collisional excitation of warm interstellar gas (Neufeld and Melnick, 1991) and was first observed in a star of late-type envelops by (Cheung et al., 1969). A decade later, examples of water masers where found in galaxies with a luminosity at 22 GHz, exceeding more then 100 times the luminosity of the sun. The advantage of this method to stellar dynamics is the spatial resolution of VLBA[2] compared to HST which can be better by a factor of ~ 200 for NGC 4258 (Miyoshi, 1995). Observations could not resolve the maser source within 3.5 and 1.3 pc for the nuclei. This excluded the possibility that the source of the masers is a superposition of massive young stars. This was the wonderful idea of (Claussen and Lo, 1986) that the source of this energy lies in an obscuring torus (not directly observable) at a pc scale.

In the middle of the '90s it was understood that the water maser could be produced when light in the X-ray regime illuminates and heats a torus of dense gas and dust. The source of this energy was assumed to originate from the accretion disc of the central SMBH. The temperature of the process has to exceed 400 K to allow the chain reactions of $O + H_2 \rightarrow OH$ and $OH + H_2 \rightarrow H_2O + H$, but not too much above this temperature in order to retain H_2.

Unfortunately, water masers are not very common. But galaxies that showed such a signature revealed a velocity field of the maser clouds of ~ 1000 km s^{-1} for NGC 4258, (Nakai et al., 1995). Very long baseline interferometric observation enclosed these velocities within $\pm 0.''05$ or ± 1.6 pc from the nuclei. It was natural to conclude that the velocities originate in a rapidly rotating Keplerian disc viewed nearly edge-on. But the crucial evidence of a SMBH came from the evidence that the systematic velocities showed a secular (orbital velocity with respect to the nuclei) and spatial variation (different maser clouds have different velocities): $\frac{d(\Delta\overline{v})}{dt} = 6\frac{\mathrm{km}}{\mathrm{s}}$, $\frac{d(\Delta\overline{v})}{d\alpha} = 280\frac{\mathrm{km}}{\mathrm{s}\cdot\ \mathrm{mas}}$ respectively (Haschick et al., 1994), where α is the angular displacement along the arc. With a distance of 7.2 ± 0.3 Mpc for NGC 4258 the calculation of the mass of the SMBH delivered $3.9 \times 10^7 M_\odot$ (Greenhill et al., 1995).

3.2.3 Gas dynamics of nuclear dust/gas disk

Observation of gas dynamics in the center of the Milky Way was already established by the end of the '70s. It was calculated that as the velocity of the gas increases from ~ 100 km s^{-1} at 1.7 pc to ~ 700 km s^{-1} at 0.1 pc which implied a virial mass of a few $10^6 M_\odot$ (Wollman et al., 1977). However, the statement has limited credibility because gas can be accelerated by other forces than gravity. At the beginning of the '90s HST made a magnitude limited sample of 12 early type galaxies in the Virgo cluster which included NGC 4261, a galaxy twice as far as the Virgo cluster. But this mistake turned out to be a lucky shot as the image shows in the inner 270 pc a nuclear dust disk surrounding the bright non-thermal nucleus of the galaxy as shown in Fig. 3.3. This picture had a direct impact because the regularity of the dust disk indicated that the material was in a cold,

[2]Very Large Baseline Array

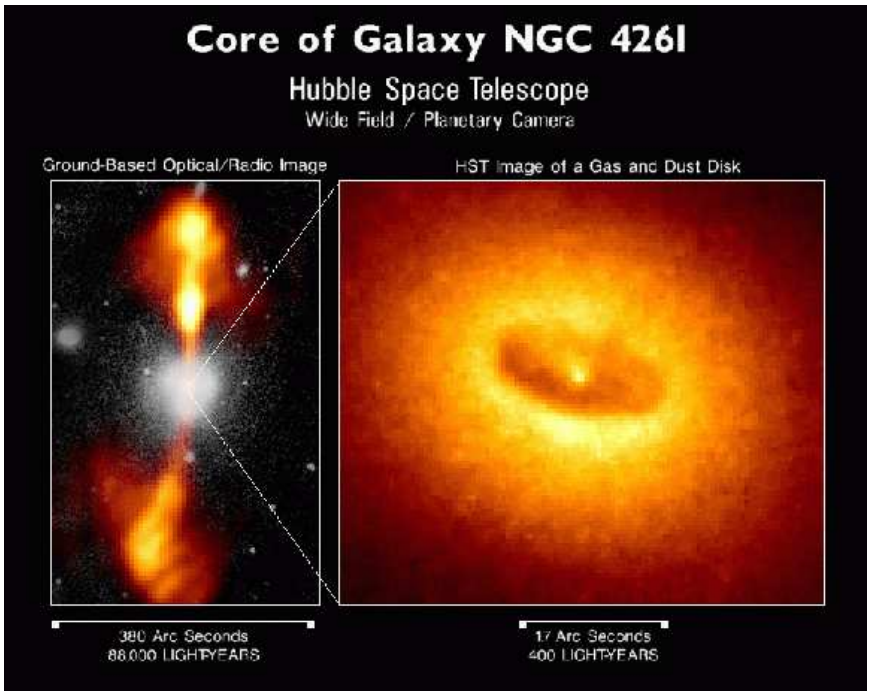

Figure 3.3: The radio jets and the center of the galaxy NGC 4261 (East Tennessee State University, 2008).

circular rotation. Together with the kinematical data, the influence of gravitational acceleration on the disk was now confirmed. For M87 this method indicated $(3.2 \pm 0.9) \times 10^9$ $M_\odot$ (Macchetto, 1997), and for NGC 4261 $(4.9 \pm 1.0) \times 10^8$ $M_\odot$ (Ferrarese et al., 1996).

The method was rapidly used for other galaxies and it was observed that gas disks are not common in elongated, fainter elliptical galaxies. Moreover, the presence of the disc made it more difficult to use the stellar dynamic method because of the dust obscuration. One can use both methods together but the number of such cases are few. Such a case is IC 1459 where the three integral models of stellar dynamics indicated a SMBH mass of $(2.6 \pm 1.1) \times 10^9$ $M_\odot$ (Cappellari, 2002) and the gas dynamic models starts from few 10^8 $M_\odot$ and reach 10^9 $M_\odot$ depending on the assumptions regarding the velocity dispersion of the gas. There is some evidence that the motion of the gas is not only gravitational, giving an uncertainty into the result.

3.2.4 The blue bump

During late the '70s it was observed that most quasars and Seyfert I galaxies show in the blue and ultraviolet (UV) spectrum a marked excess flux over the extrapolated infrared power law spectrum as emphasized in Fig. 3.4. Shields (1978) and Malkan (1983) named a "blue bump" the thermal emission from a geometrically thin but optically thick accretion disc around the SMBH. To be able to calculate the spectrum, theoretical models assume a local heat balance (i.e the heat created by viscosity within the disc is radiated locally through the disc surface), Keplerian velocity field and small accretion rate. Further more the disc is divided in concentric annuli[3] each radiating like a blackbody with the effective temperature steadily decreasing outwards. The parameters of the

[3]Annuli denotes the area between two coplanar concentric circles.

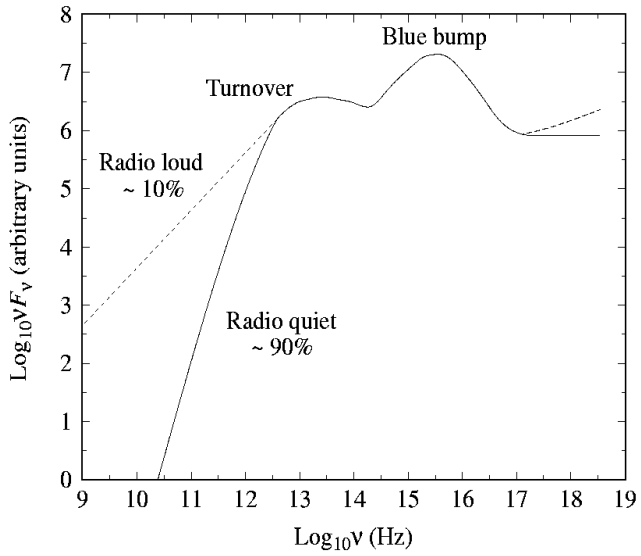

Figure 3.4: The photon spectrum for radio weak and radio laud AGN. The thermal emission has a maximum of νF_ν at $\nu = 10^{15.5}$ Hz, called the blue bump. Around this value only non-thermal emission dominates (Carroll and Ostlie, 1996).

models are: the mass of the central SMBH, the accretion rate and the inclination angle of the disk.

Even with such simple models it is possible to fit the spectrum relatively well. More realistic models (including relativistic effects, modification from blackbody radiation due to electron scattering, inner shock fronts, etc.) have been developed in the recent years which agree much better with the data. Such a fitting of optical/UV/soft x-ray data provides a powerful tool for studying the physical mechanism of the AGN activity, but is poor in the estimation of the mass of the SMBH.

3.3 Classification of AGN

Observations have shown that different types of AGN (Seyfert and radio galaxies, QSO) are all powered by the same engine: a rotating SMBH in the center, an accretion disc perpendicular to the rotation axis and, further out from the black hole, a dust torus. It is natural to assume that also the large scale structure of the AGN is the same. Thus, the difference in observing an AGN is due to the inclination angle of the observers line of sight and the rotation axis of the AGN. All these characteristics are shown in Fig. 3.5.

It is useful to define the angle of the torus, θ_t, as the maximal inclination at which the nucleus of the AGN is still visible, where, for the jet, one defines θ_j as the maximum inclination angle for which the relativistic beaming factor emitted from the jet is larger then 1. Because of the symmetric structure of the AGN, the angle between the observer and the rotation axis of the AGN lies between $0°$ and $90°$. Depending on the position of the observer to the AGN, three different cases can be distinguished:

- $\theta_t < \theta$: The angle of the observer is larger than the opening angle of the torus, thus the nucleus is obscured. Thus, the broad line region and thermal continuum radiation are hidden from the

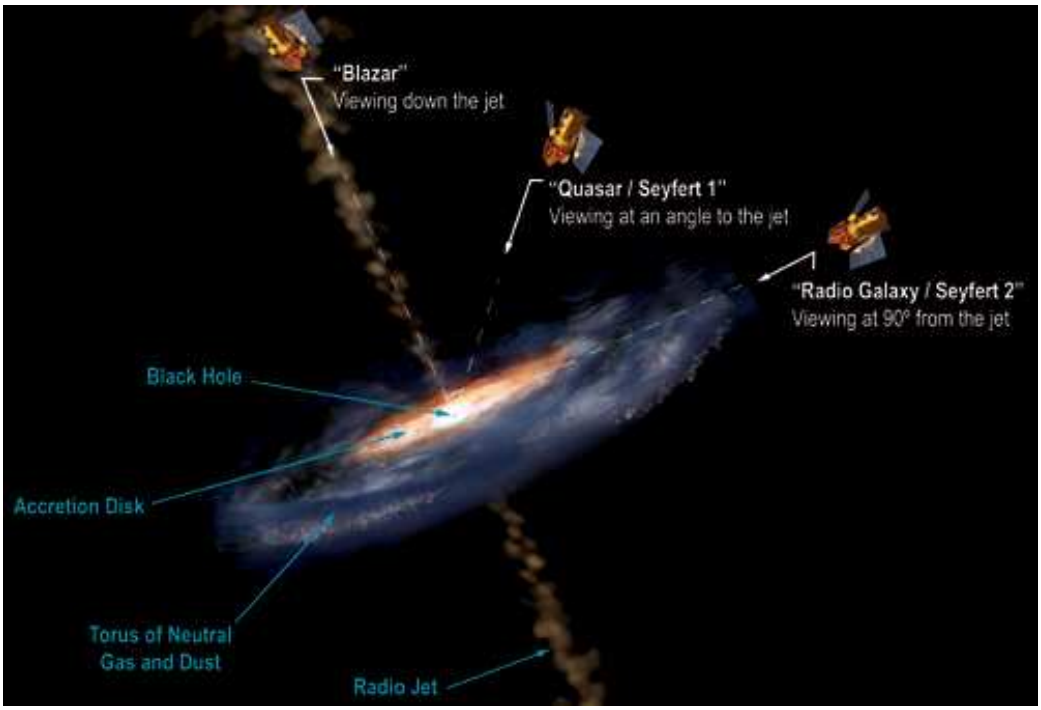

Figure 3.5: The different faces of an AGN as seen from different angle of the observer with the line of sight, together with the structure of the AGN (Aurore Simonnet, Sonoma State University, 2008).

observer and the AGN is a radio galaxy. Such AGN with low luminosity and weak jets are classified as FR I, while the ones with high luminosity are classified as FR II (Fanaroff and Riley, 1974).

- $\theta_j < \theta < \theta_t$: The angle of the observer is such that the nucleus is directly visible, but with reduced emission from the jet. Now, the spectrum of the AGN includes the blue bump from the accretion disc and the broad emission line from moving clouds. The radio region of the spectrum is dominated by emission from the lobe, with a steep shape. So far only objects with high luminosity show such a spectral configuration and are classified as Steep Spectrum Radio Quasars (SSRQ).
- $\theta < \theta_j$: The observer looks directly into the jet. In this case, the emission is relativistically boosted in the direction of the observer. The spectrum is flat in the radio regime and shows strong variability and polarization. Thus, the AGN are classified as blazars within which one can distinguish between Flat Spectrum Radio Quasars (FSRQ) and BL Lac. BL Lac are also divided into High energy cutoff BL Lac (HBL) and Low energy cutoff BL Lac (LBL), where the cutoff indicates the contribution of synchrotron emission due to electrons when it reaches its maximum. HBL are also strong x-ray sources but radio quiet. At very high energies the γ from HBL reach TeV, while LBL only reach GeV energies.

This classification enforces a unifying picture of AGN. The same mechanism was discovered for the formation of stars, for supernovae and GRB's. This emphasis that such a mechanism works independently of the object in its center and the evolutionary stadium of the astronomical object (Zhang, 2006).

3.4 The mechanism of AGN

As pointed out before, the thermal emission originates from the accretion disc surrounding the SMBH, while the non-thermal emission is generated due to an acceleration mechanism in the jet.

3.4.1 The SMBH and the accretion disc

The only mechanisms which can produce black holes originate from supernovae explosions, the merging of two neutron stars or by the collapse of gas clouds. The first mechanism requires the shortest time to obtain a black hole, $\sim 10^7$ years (the lifetime of massive stars), while the second mechanism needs stars with a longer lifetime and a sufficient merging time. The third mechanism is more difficult to occur, and it is not very well understood how much mass is needed for a gas cloud to collapse. In all three cases, the obtained black hole would have a mass of ~ 10 $M_\odot$, which is insufficient for a SMBH.

To grow a black hole, gas, stars or dark matter would have needed to feed it. Although the gravitational potential of the black hole is extensive, the matter will not fall directly into the black hole due to angular momentum conservation and because of the rotation of the black hole. The only way that mass can fall into the black hole is by losing its angular momentum. This, on the other hand, implies that the mass accumulates around the black hole and forms a stable orbit: the accretion disc. There are several methods of removing angular momentum which can be helpful in this case. The pure gravitational case implies that the potential of the incoming matter should be asymmetric, whereas the hydrodynamic dissipation needs different populations of gas, each with different angular momenta. However, both methods are insufficient to explain the observations.

A more convenient method relies on magnetic fields, which can subtract the angular momentum in two ways. One way is by means of magnetic winds. If the angle between the magnetic field line and rotation axis is bigger than 30°, the orbit around the black hole is not stable anymore. Thus, when elements from the accretion disc start to move outwards, the rotation will increase its speed constantly until it reaches the Alfvén speed. By substracting mass, a specific angular momentum is substracted as well. In this way, it is possible to discharge a larger quantity of angular momentum then the equivalent mass. Another way is by small magnetic perturbations in the accretion disc which will move the attached elements to the field of line outside the disc.

The accretion disc plays a second role because it allows a transformation of gravitational potential into radiation energy. Thus, mass spiraling down to the black hole through the accretion disc, will release an amount η of energy, which becomes larger as the density and the spin of the object grows. The accretion luminosity is expressed as

$$L_{\text{disc}} = \eta \dot{M} c^2, \tag{3.2}$$

with $5.72\% < \eta < 43.2\%$ of a particle's rest mass. Thus, observation of high luminosity implies that if $\eta = 0.1$ and $L = 1.5 \times 10^{46}$ ergs s^{-1} then the SMBH is fed with $\dot{M} \sim 2.6 M_\odot$ yr^{-1}. It is no surprise that a growing black hole is connected to starburst galaxies, where such an amount of gas is available.

3.4.2 The jet

Why is there a jet? How is the jet actually created? What are the components of the material in the jet? All these questions have so far, no clear answers, because so far, there is no detailed

mechanism known by which jets are created. Nevertheless, the best way to model a jet is trough Magneto-Hydro-Dynamic (MHD) winds where one can assume that electron-positron populations form the jet. It is the same winds which help to transport angular momentum from the accretion disc. Here, one uses the properties of the wind itself by assuming that the energy flux is dominated by the electromagnetic wave, rather than the kinetic energy associated with matter, and relativistic flows can occur with speed $\sim$ c. It is also possible to obtain the collimation of the jet as an extra feature of the MHD wind. This is possible as a consequence of the magnetic field which is frozen into the matter of the accretion disc, due to high conductivity.

Simple models emphasize that within a radius r of its center, the jet transports a current away from it, thus an inverse current must exist. This returning current flows back to the central engine through different field lines, which will eventually intersect with other field lines. This is possible if sufficient dissipation exists to induce a degeneracy of the freezing condition. By analogy, a dissipation region has to exist at the bottom of the flow where the returning current is turned around, joining the outward-going currents. It is possible, for Kerr black holes (with rotation), to form jet and radio emission without any accretion, but it is impossible to create the jets only by MHD consideration. This means that the dissipative region is responsible for the luminosity of the jet.

3.5 The origin of γ-rays in AGN

The non-thermal emission is one of the most important properties of AGN. However, there is not a concrete model which can explain all the observed elements of the non-thermal spectrum. In principal, a theoretical model exists which connects the emission to the observations, enabling an approximation of the non-thermal engine of the AGN. In the following, the components of the model, namely the Fermi acceleration mechanism, synchrotron radiation and inverse Compton models will be described.

3.5.1 Fermi acceleration

When charged particles hit a magnetized massive cloud with velocity V, it is possible to infer that they gain energy through a stochastic process. Such a process was first predicted by (Fermi, 1949). Assuming that the cloud is sufficiently massive and its velocity remains constant during the collision, the energy of the particle seen from the cloud's frame is

$$E' = \gamma_V (E + Vp\cos\theta), \;\; p'_x = \gamma_V \cdot \left(p\cos\theta + \frac{VE}{c^2} \right), \tag{3.3}$$

with $\gamma_V = \left(1 - \frac{V^2}{c^2}\right)^{-1/2}$, θ the angle between the initial direction of the particle and the normal of the cloud and p'_x the x component of the momentum. In the collision the energy is conserved and $p'_x \rightarrow -p'_x$, thus the transformation back to the observer yields

$$E'' = \gamma_V \cdot (E' + Vp'_x) \;\; \overset{(3.3)}{\Rightarrow} \;\; E'' = \gamma_V^2 E \left[1 + \frac{2Vv\cos\theta}{c^2} + \frac{V^2}{c^2} \right], \tag{3.4}$$

with $v = p_x c^2/(E \cdot \cos\theta)$. Expanding (3.4b) to second order in V^2/c^2 it follows

$$E'' - E = \Delta E = \frac{2Vv\cos\theta}{c^2} + 2\frac{V^2}{c^2}. \tag{3.5}$$

To evaluate the first term one integrates over all pitch angles ($v \approx c$), and thus

$$\left\langle \frac{2V\cos\theta}{c} \right\rangle = \frac{2}{3}\left(\frac{V}{c}\right)^2 \;\Rightarrow\; \left\langle \frac{\Delta E}{E} \right\rangle = \frac{8}{3}\left(\frac{V}{c}\right)^2. \tag{3.6}$$

The energy gain is only of second order being a very slow process, but with an increase which leads to an exponential growth. Thus, if the free path between clouds along a field line is L, then the average time between a collision is $2L/c$ and the rate of energy increase is given by

$$\frac{dE}{dt} = \frac{4}{3}\left(\frac{V^2}{Lc}\right)E = \phi E. \tag{3.7}$$

Assuming now that the particles are accelerated for a characteristic time τ_a, then the number of particles with energy E is given by

$$\frac{d}{dE}[\phi E N(E)] = -\frac{N(E)}{\tau_a} \;\Leftrightarrow\; \frac{dN(E)}{dE} = -\left(1+\frac{1}{\phi\tau_a}\right)\frac{N(E)}{E}, \tag{3.8}$$

with the solution

$$N(E) = c\cdot E^{-\alpha},\;\; \alpha = 1+\frac{1}{\phi\tau_a}. \tag{3.9}$$

Fermi's original treatment does not account for the stochastic nature of the acceleration and the particle's energy gain due to scattering. That is why to first order (in $\frac{V}{c}$) no gain is obtained. If one further develops the simple model of Fermi, then the index of the energy changes as (Bell, 1978)

$$\alpha = \frac{3}{2}\cdot\left(1+\frac{16}{9\phi\tau_a}\right)^{1/2} - \frac{1}{2}. \tag{3.10}$$

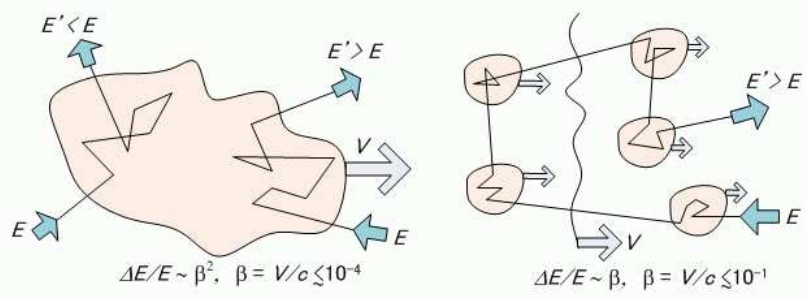

Figure 3.6: The principle for the two different fermi acceleration mechanism. On the left the mechanism for the second order Fermi acceleration; on the right the first order Fermi acceleration (Cangoroo, 2008).

If $E = \beta E_0$ is the average energy of the particle after one collision and P the probability to remain in the acceleration region, then, after i collision, $N = N_0 P^k$ particles are still accelerated and have the energy $E = E_0\beta^k$. Thus, independent of the number of the collisions one has

$$\frac{\ln(N/N_0)}{\ln(E/E_0)} = \frac{\ln P}{\ln\beta} \;\Rightarrow\; \frac{N}{N_0} = \left(\frac{E}{E_0}\right)^{\ln P/\ln\beta}. \tag{3.11}$$

This implies

$$N(E)dE = c\cdot E^{-1+(\ln P/\ln\beta)}dE, \tag{3.12}$$

which is again a power law. In this case the average energy increase is

$$\left\langle \frac{\Delta E}{E} \right\rangle = \frac{4}{3}\frac{V}{c}, \tag{3.13}$$

which is first order Fermi acceleration. In the case of shocks it can be shown that (Bell, 1978)

$$\frac{\ln P}{\ln \beta} = -1 \quad \Rightarrow \quad N(E)dE \propto E^{-2}dE. \tag{3.14}$$

Both types of Fermi acceleration mechanisms are schematically shown in Fig. 3.6.

Some important remarks can be drawn from the first order Fermi acceleration mechanism. The accelerated particles are scattered on both sides of the shock, namely upstream and downstream. The particle that recrosses the shock from downstream to upstream results in bulk streaming of the relativistic particles via the unperturbed instersellar medium. This implies that the particles with high energies will be restricted within some characteristic distance in front of the shock. Moreover, the number of particles with high energies decreases exponentially and there is an upper energy limit at which the particles can be accelerated.

3.5.2 Synchrotron radiation

When a charged particle is accelerated, a disturbance in its velocity is induced and a discontinuity in the field lines appears, due to the finite speed of light. The travel of this discontinuity can be observed and is called synchrotron radiation. For relativistic electrons which have velocities near to the speed of light, further acceleration has a small chance to occur. In the case that the electrons are accelerated in a circular motion they are deflected transversely to the direction of motion. The transverse acceleration is large because the transverse velocity can increase rapidly in a short time while passing a magnetic field.

As shown before, the jets of AGN have magnetic fields and it is natural to assume that charged particles are accelerated (*heated*) in the shock front in the jet and gain energy due to Fermi acceleration. Nevertheless, the particles lose energy due to the synchrotron radiation (*cooling*) as well from the adiabatic growth of the jet, as one moves outside. This interplay between energy depending heating and cooling of the particles leads to a gain of energy and thus to a larger gyro-radius which increases the probability of the particle to escape the shock region. Thus, the gamma-ray spectrum at low energies originates from the heating, but with increasing energy, the heating loses strength and cooling starts to dominate until a cutoff is reached (due to adiabatic losses too) (Rybicki and Lightman, 1985).

To calculate the slope of the spectrum at low energy, one needs, for the beginning, the frequency of the rotation of the charged particle. For this, one can start from the Lorentz force

$$\frac{d}{dt}(\gamma m\mathbf{v}) = \frac{q}{c}(\mathbf{v}\times\mathbf{B}) \quad \Leftrightarrow \quad m\gamma\frac{d\mathbf{v}}{dt} + m\mathbf{v}\frac{d\gamma}{dt} = \frac{q}{c}(\mathbf{v}\times\mathbf{B}), \tag{3.15a}$$

$$\frac{d}{dt}(\gamma mc^2) = q\mathbf{v}\cdot\mathbf{E} = 0. \tag{3.15b}$$

The last equation implies that γ is constant, thus one can write equation (3.15a) as

$$m\gamma\frac{d\mathbf{v}}{dt} = \frac{q}{c}(\mathbf{v}\times\mathbf{B}). \tag{3.16}$$

In the case of a homogenous magnetic field (see Appendix A for the exact calculation), the velocities are given as

$$\mathbf{v}_1 = c_0\frac{\sin(\omega_B t)}{\omega_B} + c_1 \ \text{ and } \ \mathbf{v}_2 = c_0\frac{\cos(\omega_B t)}{\omega_B} + c_1, \tag{3.17}$$

with

$$\omega_B = \frac{qB}{\gamma mc}. \tag{3.18}$$

As the integration constant c_1 is perpendicular to the plain of the first integration constants, the solution can be written as a combination of a uniform motion and a circular one

$$\mathbf{v}_{\parallel} = v\frac{\sin(w_B t)}{w_B}, \;\; \mathbf{v}_{\perp} = v\frac{\cos(w_B t)}{w_B}, \tag{3.19}$$

due to the constant $v = |\mathbf{v}|$, and ω_B represents the frequency of the rotation. The combination of the circular motion with the uniform motion along the field lines will imply a helical motion.

The total loss due to radiation can be written by means of acceleration $a_{\perp} = \omega_B v_{\perp}$ or

$$\left(\frac{dE}{dt}\right) = \frac{2q^2}{3c^3}\gamma^4\omega_B^2 v_{\perp}^2 \;\; \Leftrightarrow \;\; \left(\frac{dE}{dt}\right) = \frac{2q^2}{3c^3}\gamma^4 v^2\cos^2(\omega_B t). \tag{3.20}$$

For an isotropic distribution of the velocities, it is necessary to integrate over all pitch angles (between field and velocity) and the total energy radiated becomes

$$\left(\frac{dE}{dt}\right) = \frac{4}{3}\sigma_T c\beta^2\gamma^2 U_B, \tag{3.21}$$

with σ_T the Thomson cross section, and $U_B = B^2/8\pi$ the magnetic energy density.

Because the emission of the synchrotron radiation takes place at different points on the trajectory of the charged particle, the width of the observed pulse is smaller by a factor γ^3 compared to the gyration period. It is therefore useful to define a critical frequency

$$\omega_c \equiv \frac{3}{2}\gamma^3\omega_B\sin\alpha, \tag{3.22}$$

with α the pitch angle. Then the total energy loss can be rewritten ($\beta \approx 1$) as

$$\left(\frac{dE}{dt}\right)(\omega) = \frac{\sqrt{3}}{2\pi}\frac{q^3 B\sin\alpha}{mc^2}F\left(\frac{\omega}{\omega_c}\right), \tag{3.23}$$

with F a dimensionless function and $\frac{\sqrt{3}}{2\pi}$ a normalization factor. As the Lorentz factor, γ, is included in the critical frequency, the total energy will be independent of γ, which allows to approximate the spectrum with a power law. The spectral index (slope) is defined as

$$\left(\frac{dE}{dt}\right)(\omega) \propto \omega^{-s}. \tag{3.24}$$

Writing the number density of particles with energies between E and $E + dE$ as

$$N(E)dE = C(\alpha)E^{-p}dE \;\; \Leftrightarrow \;\; N(\gamma)d\gamma = C(\alpha)\gamma^{-p}d\gamma, \tag{3.25}$$

with p the index of the particle distribution. Then the total energy radiated per unit volume and unit frequency is given by $N(\gamma)d\gamma$ times the radiation of a single particle over all γ, thus

$$\left(\frac{dE}{dt}\right)_{tot}(\omega) = C(\alpha)\int\left(\frac{dE}{dt}\right)(\omega)\gamma^{-p}d\gamma. \tag{3.26}$$

If the integration limits are sufficiently wide one obtains

$$\left(\frac{dE}{dt}\right)(\omega) \propto \omega^{-\frac{p-1}{2}}. \tag{3.27}$$

Then the slope is connected to p as

$$s = \frac{p-1}{2}. \tag{3.28}$$

3.5.3 Inverse Compton

When a photon scatters with an electron with kinetic energy larger then the energy of the incident photon, the photon can gain energy. This process is known as inverse Compton scattering. Because of momentum conservation it follows that (Rybicki and Lightman, 1985)

$$\epsilon_1 = \frac{\epsilon}{1 + \frac{\epsilon}{mc^2}(1 - \cos\theta)}, \tag{3.29}$$

where ϵ and ϵ_1 are the energy of the photon before and after scattering, and θ is the angle between the normal of the incident direction and scatter direction. Due to Doppler shifting one has

$$\epsilon' = \epsilon\gamma(1 - \beta\cos\theta), \quad \epsilon_1 = \epsilon_1'\gamma(1 - \beta\cos\theta_1'). \tag{3.30}$$

Combining the last equations yields

$$\epsilon_1' \approx \epsilon\left[1 - \frac{\epsilon'}{mc^2}(1 - \cos\Theta)\right], \quad \cos\Theta = \cos\theta_1'\cos\theta' + \sin\theta'\sin\theta_1'\cos(\phi' - \phi_1'), \tag{3.31}$$

with ϕ' and ϕ_1' the azimuthal angles of the incident and scattered photon respectively. Thus, for relativistic electrons the photon gains a factor γ^2 of energy, if $\gamma\epsilon \ll mc^2$ (rest frame), otherwise quantum effects have to be considered. If $n(p)$ is the density distribution in phase space, and $\nu d\epsilon$ the density of photons with energies between ϵ and $\epsilon + d\epsilon$ then

$$\nu d\epsilon = n d^3p \quad \Rightarrow \quad \frac{\nu d\epsilon}{\epsilon} = \frac{\nu' d\epsilon'}{\epsilon'}, \tag{3.32}$$

where the last part of (3.36) is assured due to the invariance of d^3p to Lorentz transformation. Then the total energy emitted (scattered) in the electron's rest frame is given by

$$\frac{dE_1'}{dt'} = c\sigma_T \int \epsilon_1'\nu' d\epsilon'. \tag{3.33}$$

In the case of elastic scattering ($\epsilon_1' = \epsilon'$) and after averaging over the pitch angle, the total emitted energy can be expressed as

$$\frac{dE}{dt} = \frac{4}{3}\sigma_T c\gamma^2\beta^2 U_{ph}, \quad \text{with} \quad U_{ph} = \int \epsilon\nu d\epsilon. \tag{3.34}$$

Recalling equation (3.25) it is obvious that

$$\frac{(dE/dt)_{sync}}{(dE/dt)_{IC}} = \frac{U_B}{U_{ph}}. \tag{3.35}$$

If one takes, e.g. $B = 5\mu$G and $U_{ph} = \frac{1}{2}$MeV m^{-3} this implies that $U_B/U_{ph} = 1$ and thus both processes are equally important.

Depending on the source of photons in the jets of the AGN, two mechanisms can be identified: the photons which come from synchrotron emission called *synchrotron self-Compton* (SSC), or from an external source called *external Compton* (EC). An intresting remark is that the inverse Compton is much less efficient for protons due to the huge mass difference with the electron, whereas the Fermi acceleration is much more efficient for protons than for electrons, in accordance with observation (Sikora et al., 1987).

3.6 Superluminal motion and Doppler boosting

All these processes take place at very large distances from the observer. One of the first observations related to AGN, indicated motion that exceeded the velocity of light in vacuum. A better understanding of the observation revealed two key phenomena: superluminal motion and Doppler boosting.

3.6.1 Superluminal motion

The first observation of the motion of the radio components of 3C 273 from the nucleus revealed an angular velocity of $\omega = 0.0008''\ \mathrm{yr}^{-1}$ (Pearson, 1981). It was assumed that the motion of the radio knot was traveling in the plane of the sky, perpendicular to the line of sight, and that the distance was $440h^{-1}$ Mpc, which implied an apparent velocity of $5.57h^{-1}$c. This was clearly impossible, and thus one of the assumptions has to be wrong.

The explanation for such a huge velocity is resolved by assuming that the radio knot moves toward the observer at an angle ϕ from the line of sight with an actual velocity v. A photon emitted at a time $t_{e,1}$ will travel a distance d, where a photon emitted at $t_{e,2}$ will travel $d - \Delta t_e v \cos\phi$, with $\Delta t_e = t_{e,2} - t_{e,1}$. The photons will arrive on Earth at

$$t_{a,1} = \frac{d}{c}, \text{ and } t_{a,2} = \Delta t_e + \frac{d - \Delta t_e v \cos\phi}{c}, \tag{3.36}$$

This implies that the differences in arrival time and apparent velocity are given as

$$\Delta t = t_{a,2} - t_{a,1} = \Delta t_e \left(1 - \frac{v}{c}\cos\phi\right), \quad v_{app} = \frac{\Delta t_e v \sin\phi}{\Delta t} = \frac{v\sin\phi}{1 - (v/c)\cos\phi}. \tag{3.37}$$

From the right side of equation (3.41) after dividing by c one obtains

$$\frac{v}{c} = \frac{v_{app}/c}{\sin\phi + (v_{app}/c)\cos\phi}. \tag{3.38}$$

The condition of subluminal speed for the radio knot implies (see Appendix B for more details)

$$\frac{v_{app}^2/c^2 - 1}{v_{app}^2/c^2 + 1} < \cos\phi < 1, \tag{3.39}$$

and that the minimum point and value are given by

$$\cot\phi_{min} = \frac{v_{app}}{c}, \quad \frac{v_{min}}{c} = \sqrt{\frac{v_{app}^2/c^2}{v_{app}^2/c^2 + 1}}. \tag{3.40}$$

Thus the minimal Lorentz factor can be calculated as

$$\gamma_{min} = \frac{1}{\sin\phi_{min}} = \sqrt{1 + v_{app}^2/c^2}. \tag{3.41}$$

Applying this to 3C 273 yields $v_{min}/c = 0.984$ resulting in a Lorentz boost of $\gamma_{min} = 5.65$ and a minimal angle $\phi_{min} = 10.2°$.

3.6.2 Doppler boosting

Relativistic effects cause the apparent velocity of the jet components to exceed the velocity of light. The relativistic effects of Doppler boosting play the same role for the apparent luminosity and apparent brightness temperature of AGN as for the apparent velocity of the jet components. The Doppler factor is defined as

$$\delta = \frac{1}{\gamma(1 - \beta\cos\theta)}, \tag{3.42}$$

where γ is the Lorentz factor and θ is the jet orientation angle with respect to the line of sight. Then the apparent luminosity and brightness temperature can be computed from the intrinsic (i.e. rest frame of the AGN) as

$$L_{obs} = L_i\delta^{\alpha}, \quad \text{and} \quad T_{obs} = T_i\delta, \tag{3.43}$$

where L_i is the intrinsic luminosity that would be measured by an observer in the AGN rest frame, and α is a index which depends on the geometry of the jet and the spectral index of the population of the jet, and has typical values between 2 and 3. From equation (3.41b), (3.46) and (3.47) one can compute the intrinsic values for γ, δ and T_{obs}. In Fig. 3.7 the effect of the Doppler boosting for luminosity is shown for the case when $\alpha = 3$. One can see that the Doppler factor can reach values as high as $\sim 10^4$ for $\beta = 0.995$ ($\gamma = 10$).

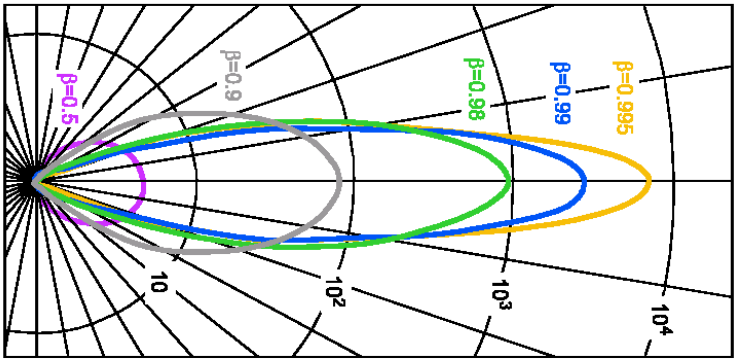

Figure 3.7: The Doppler factor for luminosity for $\alpha = 3$. The radial lines indicate angles at intervals of 10° and the circle represents the luminosity boosting factor. Red: $\beta = 0.5$,; grey: $\beta = 0.9$; green: $\beta = 0.98$; blue: $\beta = 0.99$; orange: $\beta = 0.995$ (Kellermann et al., 2007).

In the case of blazars the same effect applies to the contrajet, i.e. the jet showing in the opposite direction of the observer's line of sight, only that the jet is more attenuated. This is why near the core of AGN only one-side jets are seen. The ratio of both jets can be casted as

$$R = \left(\frac{1 + \beta\cos\theta}{1 - \beta\cos\theta}\right)^{p} \quad \Rightarrow \quad R = \left(\beta_{app}^2 + \delta^2\right)^{p}, \tag{3.44}$$

where $p = 2+\alpha$ for a moving emission region and $p = 3+\alpha$ for a continuous jet (Lind and Blandford, 1985).

Chapter 4

The main unfolding program

The unfolding method presented in 2.3.2 is implemented in a computer program written in Fortran 77, called Regularized Unfolding (Blobel, 1984). The program uses the following input files:

- Steerfile – includes the files with Data to be unfolded, Monte Carlo events and Background (if available). All files need to be in ASCII-format and have the same number of columns each representing a variable; each row of a file represents an event. The variables used for the unfolding need to be specified (maximum 3 variables). To overcome the disadvantage of using only three variables in the same time, it is advisable to use combination of variables in stead of a single variable. Optionally, the steerfile can include the energy limits of unfolding and the choice for linear or logarithmic unfolding.
- Testfile – includes nearly all parameters used in the unfolding program. Usually, the following parameters have to be fixed by the user:
  - *Global weight*: for Data and Monte Carlo the values are fixed to 1. If the Background is not needed, the global weight for the Background has to be set to zero, otherwise it is calculated as follows

    $$GW_B = N_B \cdot \left(1 - \frac{N_B \cdot LW_B}{N_D}\right) \cdot LW_B, \tag{4.1}$$

    where N_B is the number of Background events, N_D is the number of data events and LW_B is the ratio of observation time between data and Background, being a standard output of the analysis delivered by MARS.
  - *Bins*: the column of every correlation variable is filled in a histogram and the user needs to specify the number of bins for every variable individually. Additionally the energy range can be specified where the variables correlate with energy. If not specified, the program automatically calculates the energy range for each unfolding variable.
  - *Energy bins*: define the histogram of the energy and the user has to specify the limits of every bin individually. Usually the bins are chosen to be logarithmic equidistant.
  - *Energy limits*: the limits of energy (Monte Carlo) used in the unfolding. These limits can extend the limits of the energy histogram and the user has the freedom to chose the value of the limits. The program determines the minimal and maximal energy value of Monte Carlo events, which can be a guide for the specific value of the energy limits chosen for the unfolding.

  - *Number of degree of freedom* (N_{DF}): this parameter is the equivalent of the regularization constant. The value is typically close to the number of bins of the histogram for the energy.
  - *Knots* (N_K): the number of knots used for the B-spline function. One can chose $N_K = 2 \cdot N_{DF} + 3$, but this is not helpful in general (when dealing with background).
  - The user has additional options like $FXPOSITIVE$ which keeps the value of the unfolding result positive, or $SMOOTH$ which keeps the value of the unfolding result smooth.

- Mainfile – is the heart of the program and contains the local weight for Monte Carlo and Background (if used in the unfolding). The local weight for Monte Carlo is defined as

$$LW_{MC} = \frac{N_D - N_B}{N_{MC}} = \frac{N_E}{N_{MC}}, \tag{4.2}$$

  with N_{MC} the number of Monte Carlo events, and N_E the number of excess events. As already mentioned, the local weight for Background is delivered by the MARS program. The local weight for Data is 1. The file is executable so it is important to compile it after the modifications are done.

After the parameters specification, the user runs the program which will give the output (the reconstructed distribution and the error for every bin) in a few a seconds and save it in a .tex file. Some important results of the unfolding (the number of reconstructed events and covariance histograms) are included only in the logfile.

Not every combination of parameters will deliver a good unfolding result. In order to assure that the result of the unfolding is good, it is important to check: if the number of reconstructed events is as close as possible to the number of excess events and if the covariance histograms in the logfile are flat (the solution is not governed anymore by oscillations). These are necessary but not sufficient conditions for a good unfolding solution.

It is the case that specific combinations of parameters deliver no results at all. The reason for this are non-convergence of the algorithm or numerical instabilities resulting from division by zero.

Finding the right combination of parameters which will give a good unfolding solution is not such a trivial task, one has to try different combinations in order to fulfill the requirements stated above. For this purpose, only some parameters need to be changed: number of bins for the histogram of the correlation variables, number of degrees of freedom, knots, and energy limits. All parameters have integer values except for the energy limits. The total number, T_N, of all these possible combinations is given by

$$T_N = D_{V_1} \cdot D_{V_2} \cdot D_{V_3} \cdot D_{N_{DF}} \cdot D_{N_K} \cdot D_{EL}, \tag{4.3}$$

with D the domain for every correlating variables V_1, V_2, V_3, N_{DF}, N_K, and energy limits, EL. As a simple estimation let $D_{V_i} = D_{N_{DF}} = \{5, ..., 14\}$, with $i = \{1, 2, 3\}$, $D_{N_K} = \{5, ..., 34\}$ with the energy limits kept fixed, then $T_N = 10^3 \cdot 10 \cdot 30 \cdot 120 = 3.6 \cdot 10^7$ combinations. Suppose to run a combination takes ~ 1.5 seconds, this means that 5 days are necessary to check all possible combinations. If the energy limits are used as well, the result obtained before has to be multiplied with a factor of 200. This factor depends strongly on the step one uses to search the domain for the energy limits. This implies that it takes ~ 2.7 years to check all possible combinations of the parameters. Although this number appears frightening, heuristical approaches can lead to good solutions in reasonable time.

In case no good result is found, one needs to vary the energy bins too. Normally the energy bins can be optimized using Monte Carlo, which is more effective if the unfolding is without Background.

To obtain the final spectrum it is necessary to divide the obtained unfolding result with the effective collection area. The collection area is calculated via Monte Carlo simulations. This will produce a number (N_E) of excess events with energy between 10 GeV and 30 TeV with a slope -2.6

in a specific area A_0. The collection area can be computed as

$$A_{eff} = A_0 \frac{N_E}{N_{E,cut}}, \tag{4.4}$$

where $N_{E,cut}$ is the number of events which survived the cuts. Because A_0 depends on the slope, and the slope of the data is unknown, it is necessary to transform the initial slope of the Monte Carlo iteratively until the excess events of the observed data can be reproduced by the Monte Carlo. Moreover, because the Monte Carlo events are simulated without arrival time it is necessary to weight the Monte Carlo with the observation time. The collection area is calculated and delivered by the MARS program.

4.1 Variables used for unfolding

From the parameters used to describe an event, i.e. the shower observed in the camera, only some parameters will correlate with the energy, called *unfolding variables*.

The most important unfolding variable is $Size$ (the total number of photo-electrons from the shower), which is a good approximation for the energy. $Size$ has the largest correlating range with the energy. Showers with the same value for $Size$, will have, at different zenith angles, different energies, so only $Size$ cannot be used for unfolding. Another variable used for the unfolding is $Dist$ (the distance from the center of gravity of the shower to the position of the source in the camera), which gives information about the altitude (energy dependent) where the shower took place in the atmosphere. The last variable used is Zd, the zenith angle at which the shower was observed. Although this variable shows no correlation with the energy, it is important because events with the same energy observed at different zenith angles look different.

For the correlation shown in Fig. 4.1 the Monte Carlo were analyzed as normal data. The left side represents the data before the ϑ^2-cut (events from the entire camera) and after ϑ^2-cut (source position) the right side. Although the ϑ^2-cut will diminish substantially, the range of the correlation for the unfolding variables with the energy (the correlation form) remains unchanged by the cut applied.

For the unfolding of the energy spectra of sources, only $Size$ and $Dist$ proved to be necessary and the zenith angle being used only when required. Thus one can define $Size$ and $Dist$ as fundamental unfolding variables and the zenith angle as a secondary unfolding variable. Cuts can affect whether some parameters of the shower are needed for the unfolding or not (see § 4.3.3).

One is not limited to these three variables for the unfolding solution. Variables like $Lenghts$ and $Width$ correlate with energy, but they show nearly the same correlation as $Size$, as emphasized in Fig.4.3. The red points represent averages over the bins content and the black line, a linear fit. Since the correlations of $Length$ and $Width$ with $Size$ are linear, no new information can be gained for the unfolding solution. As the program is limited to three unfolding variables, $Length$ and $Width$ were not used for the unfolding also for reason to be explain below.

4.2 Optimization of the unfolding program

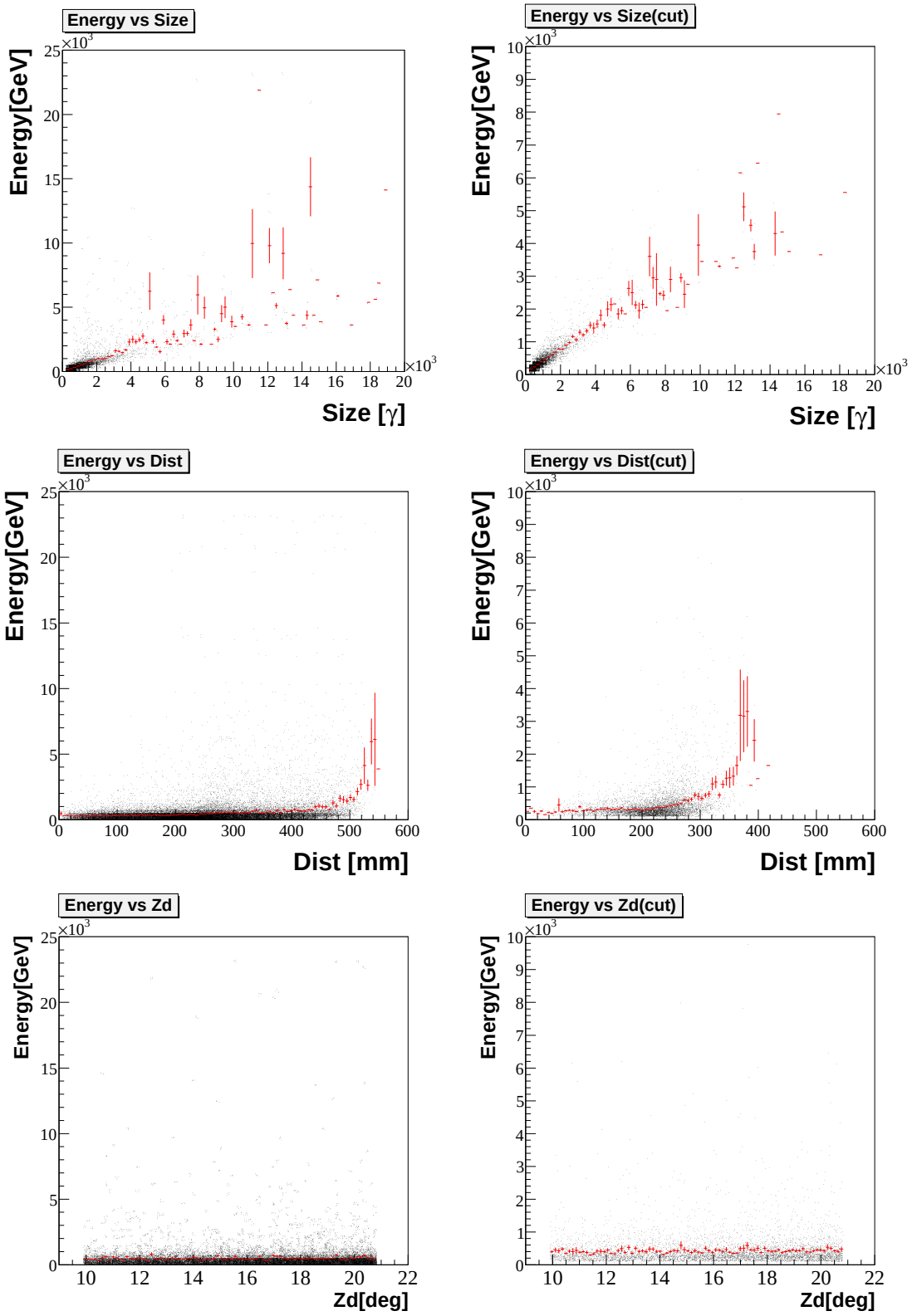

Figure 4.1: The parameters used for unfolding, i.e. *Size*, *Dist* and *Zd*, and their correlation with the energy. On the left side the correlation is shown before ϑ^2-cuts and on the right side the same parameters after ϑ^2-cuts. The black points represent individual events, whereas the red ones averages over bins.

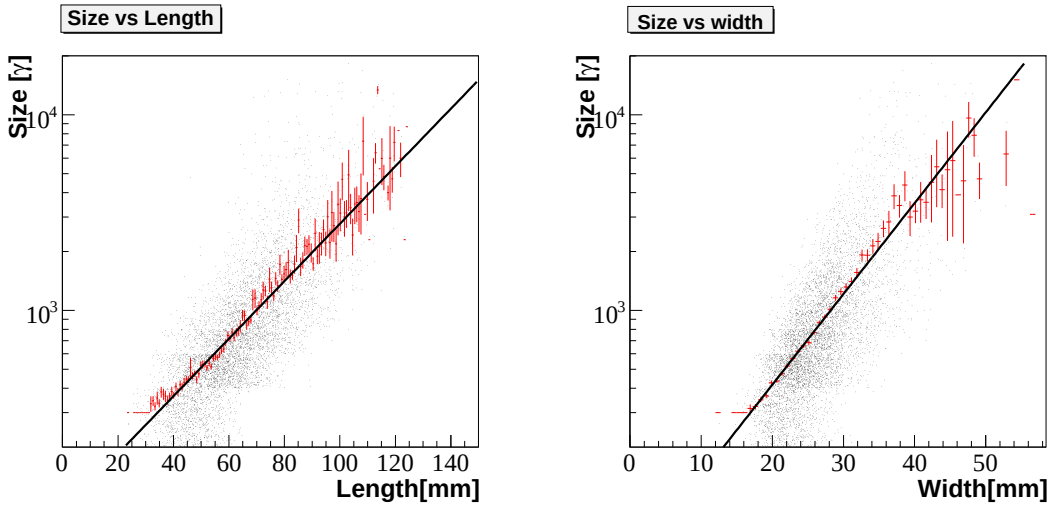

Figure 4.2: On the left: the correlation of *Length* versus *Size* before θ^2-cuts. On the right: the correlation of *Width* versus *Size* before θ^2-cuts. The black points represents individual events, whereas the red points averages over bins. The black line represents a linear (logarithmic) fit.

As already emphasized, it is difficult to find a good unfolding solution, so optimization techniques are required. There is a strong impediment in developing an optimization algorithm to find the unfolding solution: the analytical expression of the function to be optimized is not known.

To fulfill the conditions, an unfolding solution should have a variable that contains specifications about the flatness of the covariance histograms. In this sense, a χ^2 test was introduced for each histogram, i.e. the values for χ^2 increase as the histograms get flatter. In this way the automatic comparison becomes possible between the two χ^2 values and number of reconstructed events with some desired values.

Since the function we want to optimize is not known analytically, it is not possible to apply some standard numerical optimization algorithms, which will need the expression or the approximation of the gradient of the function. All one knows, after running the unfolding program, are the values of the function in a point (combination of unfolding variables). The optimization idea in this situation is to apply a searching strategy which explores the features of the unfolding program.

For a result obtained with an optimization method, one cannot be sure if it is the optimal solution or not, if we are in a local optimum or in a global one, or just in a critical point (not minimum and not maximum). Therefore, one does not know how far from the optimal solution is the obtained one, i.e. if the unfolding solution is suitable. In Fig.4.3 two different functions are plotted, both of them having many local optima. For the one on the left side, the local optima are close to the global optima, whereas for the one on the right side this is not the case, the local optima are decreasing constantly.

The quantity to be optimized is the value χ^2 for the second histogram, since the first histogram is usually flat. We have to determine the values of the unfolding variables which will make the second χ^2 flat as well, keeping the first one flat. So, we have to handle an optimization problem on

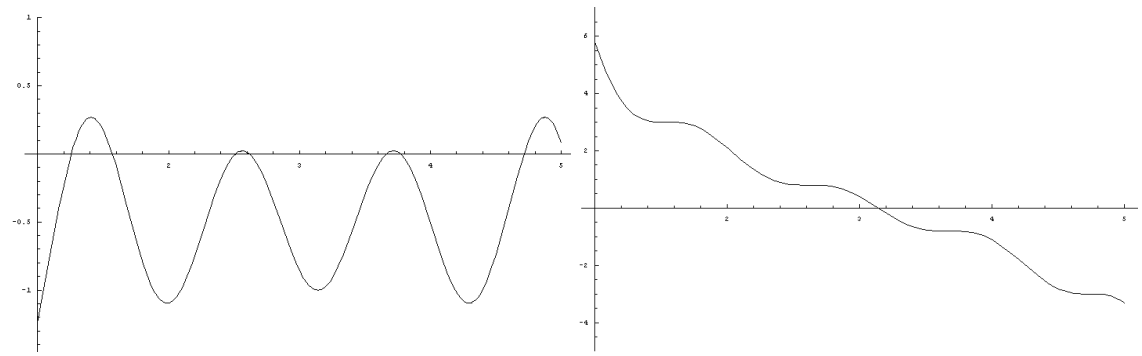

Figure 4.3: The different distribution of critical points, i.e. minima and maxima for arbitrary function. On the left plot the maxima/minima have nearly the same value, whereas in the right plot, the minima follow a decreasing trajectory.

a parameter space $D_Z^5 \times D_Q^2 \subset \mathbb{Z}^5 \times \mathbb{Q}^2$, subject to some restrictions

$$\begin{aligned} &\max_{x \in D_Z^5 \times D_Q^2} \chi_2^2 \\ &\text{s.t. } \chi_1^2 > c_0 \\ &\quad |N_I - N_E| \rightarrow \min \end{aligned} \tag{4.5}$$

where c_0 has to be set by the user and can vary between 3 - 7, N_I is the number of unfolding events and χ_1^2, χ_2^2 are the values for the χ^2 for the first and the second covariance histogram respectively.

Experiments have shown that in the case of unfolding without Background, the parameter space where one searches for the solution reduces to $D_Z^5 \subset \mathbb{Z}^5$, since solutions can be found without optimizing also the energy limits. The optimization of the energy limits becomes necessary when Background is required for the unfolding.

4.2.1 Optimization without Background

In the case of optimization without Background, the number of excess events is the same as the number of data events. So the second constraint in problem 4.5 becomes $N_I = N_E$, but since the number of unfolded events (depending on the five parameters) will oscillate around the number of data events only within few percentages, the constraint on them can be neglected. The optimization problem is now much easier to handle and can be rewritten as

$$\begin{aligned} &\max_{x \in D_Z^5} \chi_2^2 \\ &\text{s.t. } \chi_1^2 > c_0 \end{aligned} \tag{4.6}$$

Still, the unknown dependency of χ_2^2 on the unfolding variables is an impediment in applying a straight-forward maximization technique to find the optimum of the problem. What one can do in such a situation is to try to increase at each step the value χ_2^2 by optimizing along the domain of every unfolding variable individually, i.e. solving the following problem

$$\begin{aligned} &\max_{x_5 \in D_{N_K}} \Big(\max_{x_4 \in D_{N_{DF}}} \Big(\max_{x_3 \in D_{V_3}} \Big(\max_{x_2 \in D_{V_2}} \Big(\max_{x_1 \in D_{V_1}} \chi_2^2 \Big) \Big) \Big) \Big) \\ &\text{s.t. } \chi_1^2 > c_0 \end{aligned} \tag{4.7}$$

Start with an arbitrary point $x^0 = (x_1^0, x_2^0, x_3^0, x_4^0, x_5^0) \in D_Z^5$. One associates x_1^0 with the number of bins for the histogram corresponding to the first, x_2^0 to the second and x_3^0 to the third variable, x_4^0 with N_{DF} and x_5^0 with N_K. With these specifications, $D_Z^5 = D_{V_1} \times D_{V_2} \times D_{V_3} \times D_{N_{DF}} \times D_{N_K}$ and as already mentioned, the optimization will take place for each $x_i^0,\ i = \{1, ..., 5\}$, individually. The order in which this optimization will perform is important. For this optimization procedure the order is given by (4.7).

Let E_min, E_max and GW_B be fixed by the user and let s_0 denote the value of χ_2^2 for the starting point x^0. Then, one begins with the maximization of χ_2^2 with respect to the first variable x_1, by varying it over the domain D_{V_1} and keeping the other variables x_2, x_3, x_4, x_5 fixed to their initial values. In this way, a number of $|D_{V_1}|$ values for χ_2^2 are delivered from which the maximal value and the maximal point can be extracted. In the case that there exists more than one maximal point, the first one is chosen and denoted with x_1^1 giving the value s_1 for χ_2^2 and the optimization continues from $(x_1^1, x_2^0, x_3^0, x_4^0, x_5^0)$ with respect to the second variable along the domain D_{V_2}. The new maximum variable is denoted with x_2^1. In the case no bigger value is found, we remain with the initial value x_2^0. After each iteration, we are assured that the value of χ_2^2 increases or remains the same, in which case we continue to apply the procedure for the rest of the variables hoping for an improvement. When all domains of the variables were checked, the new point becomes $x^1 = (x_1^1, x_2^1, x_3^1, x_4^1, x_5^1)$ and we say that one step was made. If the value of the χ_2^2 doesn't increase even after the point $x^2 = (x_1^2, x_2^2, x_3^2, x_4^2, x_5^2)$ the program stops because the initial starting point x^0 will not bring us to achieve a bigger value for χ_2^2. So the final value obtained for χ_2^2 can give the unfolding solution we are looking for, but it can also be just a local maximal value which is not suitable for the unfolding solution. To overcome this inconvenient one possibility is to choose another initial starting point $x^0 \in D_Z^5$, or to modify the value of c_0, or to play with the limits of the energy, but this requires good experience in working with the unfolding program.

Experimental work shows that the optimization algorithm needs less than five steps to end the searching process, which means between 3 and 7 minutes.

4.2.2 Optimization with Background

In the case of optimization with Background, the excess events N_E represent the difference between the number of data events and background events. The presence of the background will imply a stronger variation of the number of unfolded events N_I compared to N_E, and the optimization will follow the form (4.5). Although the subtraction of the background events is not a difficult task, it is still possible that N_I deviates more than double from N_E, which is clearly an unsatisfactory result. This deviation of N_I from the expected value originates on the one hand in the cuts applied during the analysis of the data on the chosen bins for the variables and for the energy limits on the other hand.

The difficulty of the optimization arises since one tries to increase the value for χ_2^2 and, in the same time, to keep N_I as close as possible to N_E. For such a problem, the following observation turned out to be very helpful: after choosing a point from D_Z^5, N_I will depend only on the energy limits, i.e. $N_I = f(E_{min}, E_{max})$. Observations while unfolding data of different sources have shown that $f(\cdot, E_{max})$ is a parametric curve which will be shifted up and down correspondingly to the values chosen for the parameter E_{max}. The property that $f(\cdot, E_{max})$ has the same shape (depending only on the chosen point in D_Z^5 and energy bins) independent of E_{max}, helps to reach the minimal and/or maximal value of N_I in one covering of the domain for the energy limits. The property can be expressed as follows

$$\min_{(E_{min}, E_{max}) \in \mathbb{Q}} (N_I) = \min_{E_{max} \in \mathbb{Q}} (\min_{E_{min} \in \mathbb{Q}} (f(E_{min}.E_{max}))), \tag{4.8}$$

With the observation made above, N_I can be controlled such that its value is reduced/increased to be as close as possible to N_E. This is the reason why the maximization problem (4.5) can be divided into two quasi-independent problems. One problem regards just the maximization of the value for χ^2_2 and the second one uses the energy limits to bring N_I in the neighborhood of N_E.

There is no analytical expression for the function $f(E_{min}, E_{max})$ and to find one is difficult because there are too many variables into discussion, i.e. all the variable one has to set before the unfolding (see 4.1). Thus, it is always necessary to compute $f(E_{min}, E_{max})$ point by point, which is exactly what the optimization does. It can happen that the minimal/maximal value of N_I is not close enough to N_E, in which case the following are possible: one can chose a new starting point for the optimization, or can change slightly the value of global weight for the Background up to 2-3% (the overall behavior of the data is not changed). As N_I is sensitive to GW_B, i.e. its value will be changed significantly only by a minor change of GW_B, the parameter space for the second condition of (4.5) will be given by the domains of the two energy limits and the small neighborhood of GW_B, denoted by $D^3_Q \subset \mathbb{Q}$.

As for the case of optimization without Background, an initial point $z^0 = (x^0, y^0)$ is chosen with $x^0 \in D^5_Z$, $y^0 \in D^3_Q$ which has to fulfill the condition $|N_I - N_E| < \varepsilon$ for ε set by the user. If the restriction does not hold, the energy limits and GW_B have to be optimized until $|N_I - N_E| < \varepsilon$ holds and the new point y^1 will become y^0. With z^0 set, the optimization of the χ^2_2 value is performed, which will give the new point x^1 and again it is required to verify if the condition $|N_I - N_E| < \varepsilon$ is fulfilled for (x^1, y^0). If not, another $y^1 \in D^3_Q$ is searched such that $z^1 = (x^1, y^1)$ fulfill the condition. After every step (going from x^{k-1} to x^k), the condition $|N_I - N_E| < \varepsilon$ has to be verified. The important ingredient for this task is: if $\chi^2_2(x^0, y^0) = s_{00}$ and $\chi^2_2(x^1, y^0) = s_{10}$, is required that $\chi^2_2(x^1, y^1) = s_{11}$ has to be greater than s_{00}, in order to assure the increase in the value of χ^2_2. If one would not allow that GW_B changes slightly, the previous requirement would be very difficult to fulfill. Moreover, changes of N_I due to GW_B will imply not only one value for N_I that fulfills the constraints of (4.5), but an entire set $\mathcal{N}$ of values. More values in the set $\mathcal{N}$ imply higher probability to find $y^1 \in D^3_Q$ such that $s_{00} < s_{11}$. To increase even more the probability, it is helpful to optimize the energy limits on a set of GW_B instead of one value only.

The optimization with Background will necessitate more time to compute a bigger value for χ^2_2 than the optimization without Background, so the entire optimization scheme will take between 5 and 13 minutes. The time needed for the optimization depends on the domain where the solution is searched for. Knowing the domain of the number of bins for the unfolding variables, the restriction from (4.5) is easier to handle as the next subsection will show.

4.2.3 The unfolding factors

For the need of understanding the complexity of the unfolded data, it is useful to introduce the following two factors:

- *variability factor* with respect to the energy limits of N_I given by

$$\rho = \frac{N_I^{max}}{N_I^{min}}, \tag{4.9}$$

  where N_I^{max} is the maximal number of unfolded events and N_I^{min} is the minimal number of unfolded events;

- *probability factor* of N_I to lie close to N_E for 100 (or a sufficient large number) of randomly chosen points in D^5_Z for a pair of energy limits, denoted as $\pi(|N_I - N_E| > \varepsilon)$.

Both factors indicate how easy/difficult it is to unfold the data, more specifically, small values for ρ_V indicate a small variation of N_I with respect to the energy limits and GW_B, while larger values indicate jumps of N_I by a small change in the energy limits and/or GW_B. The same applies for the probability factor $\pi(\varepsilon)$ with fixed energy limits, which means that if the probability factor is small, a large range of N_I will lie close to N_E (in the given limits) and only a few far. Concluding, small values for both factors ρ_V and $\pi(\varepsilon)$ suggest that the data are easy to unfold and that only few optimization runs are necessary to obtain a satisfactory unfolding result. Meanwhile, large values of the parameters conclude that the data are difficult to unfold and that the optimization needs to run many times until a good solution is obtained.

Another interpretation for the two factors can be given, if the two factors have high values it means that one or maybe more unfolding variables are not suitable for the unfolding. To see which one of the unfolding variable causes the high value for both factors, one can plot N_I for the number of bins for every unfolding variables versus $1 - \pi_5$, where π_5 represents $\pi(|N_I - N_E| > 0.05)$. Such a plot is called a π_5 *plot*. For $Size$ and $Dist$ the π_5 plots indicate a broad range to search for the solution, reason why $Size$ and $Dist$ are called fundamental unfolding variables. Unlike the previous cases, the plot for Zd shows a very narrow range with a clear peak. The narrow range originates in the missing correlation between Zd and energy, although if such a correlation would exist, the peak would move with the change in the energy limits, creating a broad range as for the cases of $Size$ and $Dist$. The π_5 plots can be used to determine the domain for every unfolding variable. Moreover, the π_5 plot can be used for any parameter which describes the shower in the camera to test if it is suitable for unfolding or not. This is possible if one notices a broadening and/or increase of $1 - \pi_5$ of the domain of the unfolding variable already suitable for the unfolding, otherwise no new information is gained. On the other hand, if the peak is at 0, as it is often the case for Zd, one can conclude that Zd should be not used in the unfolding. As the two factors are independent of the unfolding result[1] it can be concluded that the data, after being analyzed, do not include information about the zenith angle.

The two factors ρ and π are introduced to verify some properties of the unfolding program described in the thesis, more precisely the response of the unfolding variables such that N_I is close to N_E. but finally it turned out that they are independent of the unfolding program used. The factors indicate the domain in which the convergence of the unfolding program is optimal, bed convergence being underlined by a non-smooth behavior of the data, i.e high value for ρ and π. Another property of these factors is that they can indicate missing information about unfolding variables. Generally, the highest value for the π_5 plot for each unfolding variable is about 80%, but in some cases much smaller values were noticed (bellow 70%), which suggests that for unfolding some information of the data (parameters that describe the shower) were not used.

As specified before, variables which do not correlate with energy will show a narrow range in the π_5 plot, but their value $1 - \pi_5$ from the π_5 plot modifies as GW_B varies. If the value of GW_B is not known GW_B is varied until $1 - \pi_5$ attains the maximal value. It turns out that this maximal value of $1 - \pi_5$ is reached for the value GW_B given by (4.1).

For any unfolding method, it is possible to define factors in a similar way as π and ρ were defined, i.e. to keep information regarding the convergence of the method and restrictions. In this sense it can be expressed the independence of π and ρ of the unfolding method used.

[1] One does not need to compute the values for χ_1^2 and χ_2^2 for the π_5 plots as this information are included in ρ.

4.3 Test of the optimized unfolding method

The simplest test one can use for any unfolding program is to unfold a distribution which is already known. As emphasized before in the Monte Carlo simulation, the energy distribution of the arriving photons is known. Thus, unfolding the energy distribution from Monte Carlo is a fast test for the unfolding program with no Background. To test the unfolding method with Background on real data, a *standard candle* for the VHE-observation (calibration for unfolding methods) was chosen, namely the Crab Nebula.

4.3.1 Test on Monte Carlo

The most simple way to test the unfolding program is by using Monte Carlo because the energy for every event is already known. For this the Monte Carlo is divided into two samples, one playing the role of data and the other representing the Monte Carlo used to determine the unfolding parameters described in chapter 2. The zenith angle for the used Monte Carlo is between 10° and 25°. Both Monte Carlo samples were analyzed as normal data. The range of the true energy is between 75 ($10^{1.87}$) GeV and 11.22 TeV (=$10^{4.05}$ GeV). The unfolding result is given in Fig. 4.4, where the black line gives the true distribution of the energy and the blue points give the unfolded results. As can easily be noticed, the first bin starts below the true energy range 63 (=$10^{1.8}$) GeV, but the unfolding program could handle the discrepancy well, i.e. unfolding with less statistics in the first bin.

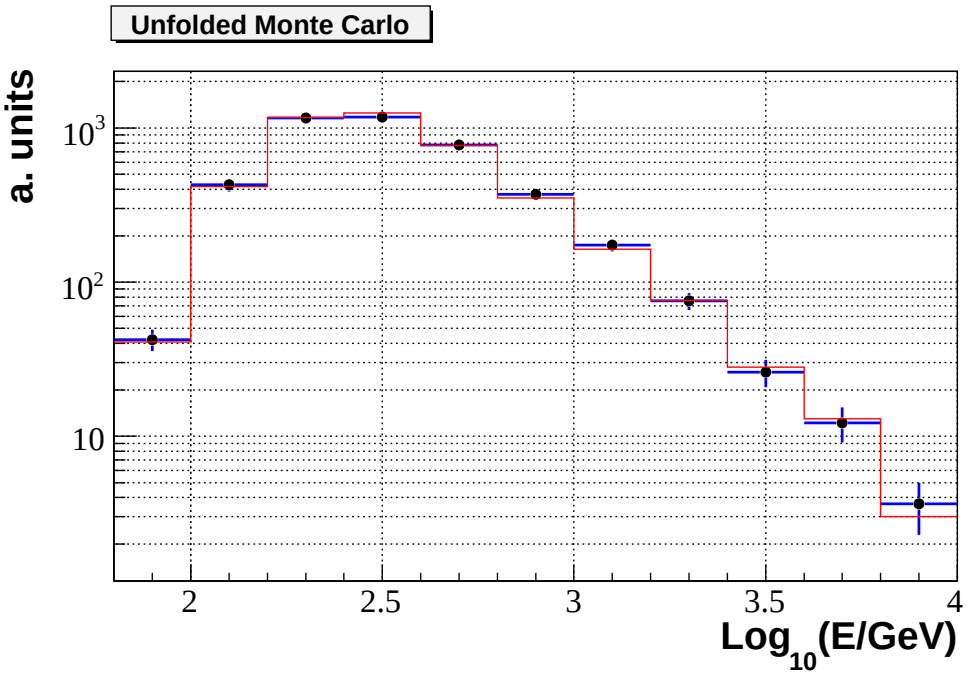

Figure 4.4: The result of the unfolding test with Monte Carlo. The black line is the true distribution of the energy, whereas the blue points are the distribution after unfolding with regularization.

The π_5 plots for the unfolding variables *Size*, *Dist* and *Zd* are given in Fig. 4.5. Every bin consists of 100 runs of the unfolding program. For *Size* and *Dist* the domain is 2 - 20 and 0-18,

respectively. Above the upper limits of the domain, ρ_V is greater than 1.1. As for the case of Zd, the domain has a narrow range from 0 to 1. After the standard data analysis, one can see that the Monte Carlo hardly depend on the zenith angle. The difference between using Zd ($Zd = 1$) and not using Zd ($Zd = 0$)for unfolding consists in the difference in the values of ρ_V, $\rho_V = 1.0347$ for the first case and $\rho_V = 1.0108$ for the second one. Moreover, in most of the runs, exchanging the number of bins for the zenith angle between 0 and 1 showed no significant modification if any, for both values of χ^2 and number of unfolded events. The reason why no zenith angle ($Zd = 0$) was used for the π_5 plots of $Size$ and $Dist$.

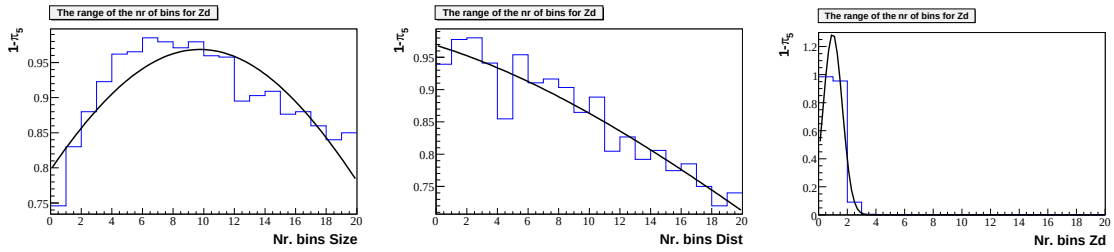

Figure 4.5: The π_5 plots for the individual unfolding variables: $Size$, $Dist$ and Zd. The black line represents a gaussian fit. As $Size$ and $Dist$ correlate with energy, the distribution is broad, whereas for the Zd which does not correlate with energy, the distribution has a narrow peak.

4.3.2 Test on Crab Nebula

Sometime during the year 1054 entire humanity witnessed a magical moment: a star, which before was one of the millions or billions of stars became so bright in the sky that one could see it even during the day. It was believed that the sphere of the stars would collapse on Earth. Although the knowledge humanity gained over the past 1000 years is tremendous, the object known as the Crab Nebula kept its magic until today.

Being $\sim$ 6500 light-years away, the bright emission observed in 1054 represents the death of a star which left behind a nebula (which appears today in the form of a crab) and a pulsar (neutron star) PSR B0531+21 with a period of 33 ms. The spectrum of the Crab Nebula extends nearly over 20 order of magnitudes, from radio (10^{-5}eV) to VHE (10^{14}eV). The strong magnetic field B $\geq$ 0.1 mG nominates the Crab Nebula as an excellent accelerator and is therefore the best studied object emitting non-thermal radiation.

At very high energies, the Crab Nebula was first discovered by the Whipple collaboration (Weekes et al., 1989). The Crab Nebula has a very stable flux and it is the strongest stable VHE γ-ray source in our galaxy. More then 10 different experiments have already measured the flux of the Crab Nebula and agreed very well from $\sim$ 200 GeV to $\sim$ 100 TeV (Akerlof et al. 1990,Vacanti et al. 1991; Baillon and et al. 1991; Goret et al. 1993; Konopelko et al. 1996 Tanimori et al. 1998; Hillas et al. 1998; Amenomori et al. 1999; Majumdar et al. 2002; Horns and HEGRA Collaboration 2003; Aharonian et al. 2000, 2004, 2006), which confirm the synchrotron nature of the spectrum of the Crab Nebula. Below 200 GeV, the data is delivered by solar arrays (Oser et al. 2001; de Naurois et al. 2002; Arqueros et al. 2002) where large uncertainties in the calculation of the effective collection area and γ/hadron differentiation are present. By this, it is difficult for the solar arrays from this generation to perform detailed differential flux measurements.

To understand the nebular dynamics and the observed spectrum up to GeV energies, one needs

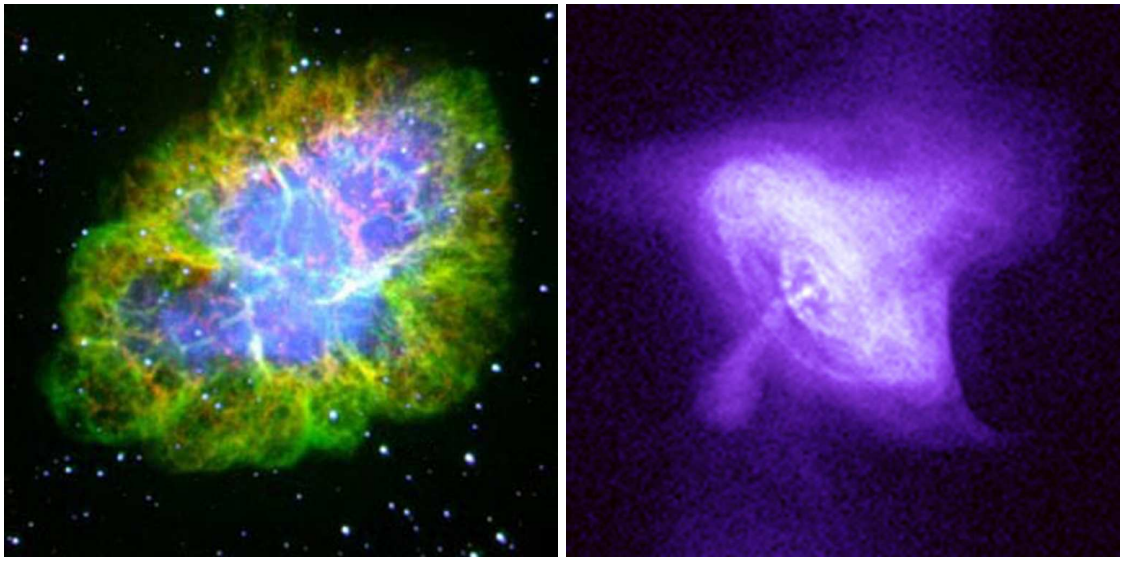

Figure 4.6: The Crab Nebula in visible light on the left, and in x-ray on the right (Universita degli studi di Firenze, 2008).

a magneto-hydrodynamic model which was first proposed by Rees and Gunn (1974) and developed by Kennel and Coroniti (1984a,b). In this model, the pulsar provides a continuous flow of particles, the so-called *pulsar wind*, with Lorentz boost factor of $10^6 - 10^7$. These wind particles gain their energy due to shock acceleration and lose their energy due to synchrotron radiation. The observed synchrotron emission at a few hundred MeV together with the γ-spectrum at TeV is an indicator that charged particles are accelerated up to energies of $\sim 10^{15-16}$ eV.

Above the GeV regime, the dominant source of γ-ray is the inverse-Compton (IC) scattering of synchrotron photons from the synchrotron emitting electrons (SSC) (Gould 1965; Weekes et al. 1989; de Jager and Harding 1992). Together with the IC scattering, one also has contributions to the seed photons fields from far-infrared excess, cosmic microwave background and mm-photons (Aharonian et al., 2004).

Specific contributions to the IC-mechanism, which describes well the observed energy spectrum in the 500 GeV – 10 TeV window, is the hadronic component in the pulsar wind. In the interaction of these components with the insterstellar medium, VHE γ-rays are emitted (via π^0 decay) which modify the spectrum at the TeV range and beyond (Atoyan and Aharonian 1996; Bednarek and Protheroe 1997; Bednarek and Bartosik 2003; Amato et al. 2003). Moreover, it is possible that an "amplified" bremsstrahlung flux at GeV energies (Atoyan and Aharonian, 1996) accounts for the discrepancy between the measured GeV flux and the prediction from the SSC model (de Jager et al., 1996). If this is true, one should expect a slope between $2.5-2.7$ in the 0.1-10 TeV window. Another contribution to the IC-mechanism are relativistic electrons in the unshocked pulsar wind. As the target photons are emitted by the pulsar, a pulsed component can reach γ-ray energies of several hundred GeV.

Because the cooling time decreases with energy due to synchrotron losses, only electrons with lower energies will reach out into the nebula, thus the effective source size of the observed γ-ray spectrum will decrease as the energy increases. However, the source size will increase if ionic components are present. Up to now the size of the measured VHE γ-ray emission region is < 1.5' for energies above 1 TeV (Aharonian et al., 2000).

The origin of the very high energy emission is assumed to be synchrotron radiation from relativistic charged particle which are forced to move along the magnetic field lines inside the magnetosphere

of the pulsar. However, it is still an open question whether the particles are accelerated or not. Theoretical models assume that the production of electrons and positrons and their acceleration take place either above the polar cap of the neutron star (Harding et al., 1978; Daugherty and Harding, 1982), in outer gaps between the null surface and the light cylinder of the magnetosphere (Cheng et al., 1986; Chiang and Romani, 1992) or at the outer rim of the polar cap ((Arons 1983, Muslimov and Harding 2003)).

The following analysis of the Crab Nebula is based on data taken with the MAGIC telescope between October and December 2005. To be sensitive to events at low energies, the On/Off mode was used for the performance of the observation. Approximative 16h of On-data was collected and 19h of Off-data. To get a better On:Off ratio, extra 7h of Off-data were used from other sources which were observed within the same parameter specification (zenith angle, observation period, etc.) as the Crab Nebula. Because the energy threshold depends on the zenith angle, i.e. lower zenith angle will increase the probability to observe events at lower energies, all data exceeding a zenith angle $\lesssim 20^\circ$ were not used in the analysis. Additional quality cuts were performed: high fluctuation in data rate, atmospheric light, etc., cuts which prove to be very important for the unfolding of the spectrum. For better statistics at lower energies, cuts were open to reach a cut efficiency of 65%.

After analyzing the data, a significance of 68.5 σ was obtained with 8305 excess events and 4390 background events, see Fig. 4.7. Monte Carlo was selected in the same range for the zenith angle and with a PSF close to the one of the data. From the solutions found using the optimized unfolding program, the one with the most smoothest form was selected (minimal ρ_V). In Fig. 4.7 the unfolding result is drawn in blue, whereas the red points and the red line represent the unfolding results obtained using the standard unfolding method of the MAGIC collaboration (Albert et al., 2008a). As it can easily be seen, the results are in good agreement.

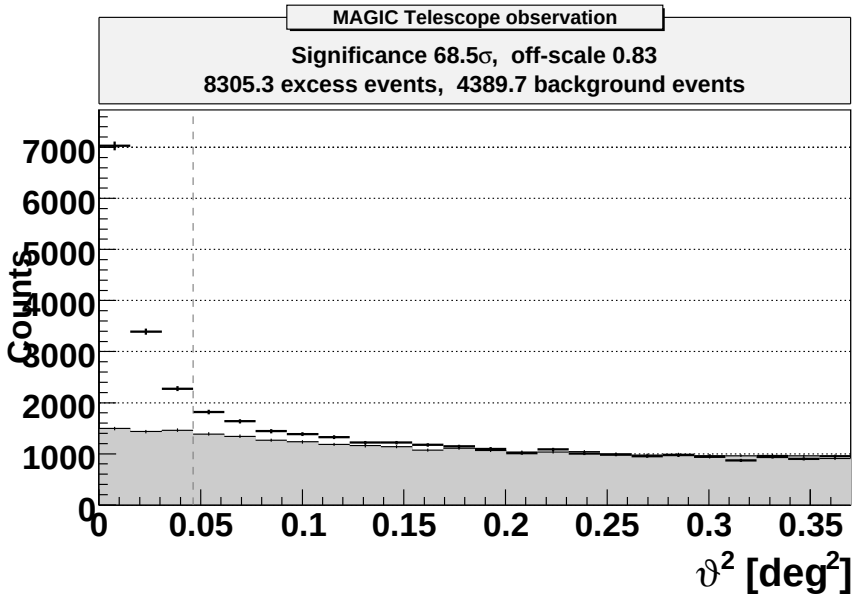

Figure 4.7: The significance for the Crab Nebula. The black points represents the On-data, whereas the gray shaded region the Off-data.

The distribution for the number of bins for each unfolding variable is shown in Fig. 4.9. To obtain a sufficient good estimation, 200 runs were used for every bin. If one chooses a lower limit of 70% for the value $1 - \pi_5$ of every individual unfolding variable, then for *Size* and *Dist* the starting points will be 6 and 5 respectively. ρ_V increases with the number of bins and the maximal admissible

value of ρ_V is set by the user. The upper limit of the number of bins is attained when ρ_V passes its maximal admissible value. For the zenith angle the range is again very narrow, between 2 and 3. The huge bump (from 7 to 20) in the figure is due to inhomogeneity in the data and also to the difficulty to determine the Background at lower energies for the case of the On-Off observation mode (Bretz, T; et al., 2005). The reason why only for the first bins a fit was done.

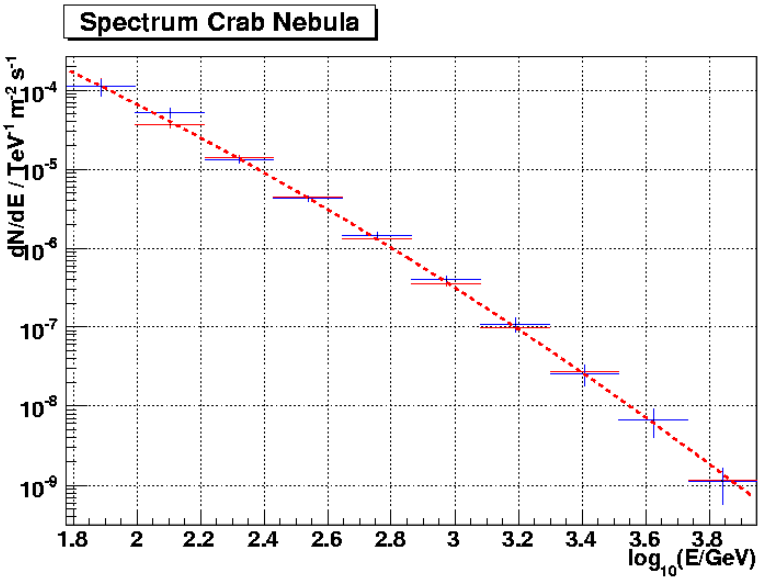

Figure 4.8: The spectrum for the Crab Nebula. The blue points represents the result obtained with the probability unfolding method, whereas the red points are the results obtained for the same data with the direct method (Albert et al., 2008a). The red curve represents the fit to the red points.

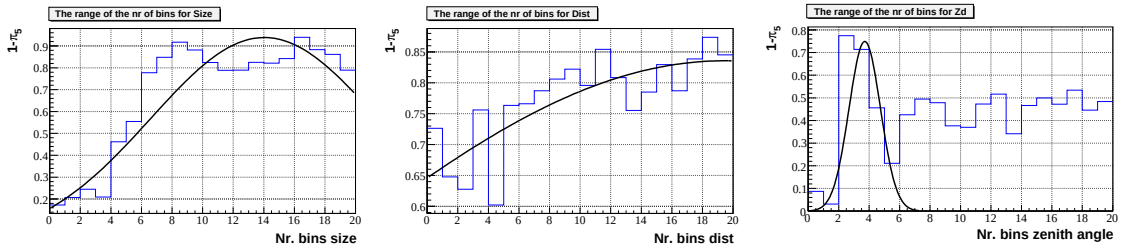

Figure 4.9: The range for the number of bins for the unfolding variable: *Size*, *Dist* and *Zd*. The low values for *Size* and *Dist* compared to Monte Carlo originated from the different cuts and the background, which, in the On-Off mode, is less homogenous as for the Wobble mode. The π_5 plot for *Zd* clearly indicates the narrow range of 2-3. The fluctuation around 0.43 that follow the narrow peak has its origin also in the background, On-Off observation mode, and inhomogeneity in the data.

The energy spectrum was parameterized with a curved power-law (Albert et al., 2008a)

$$\frac{dF}{dE} = f_0 \left(\frac{E}{300\text{GeV}} \right)^{a+b\log_{10}\left(\frac{E}{300\text{GeV}}\right)}, \tag{4.10}$$

with f_0 being the flux normalization calculated as $(6.0 \pm 0.2_{\text{stat}}) \times 10^{-6}$ m^{-2} s^{-1} TeV^{-1}, $a = -2.31 \pm 0.06_{\text{stat}}$ and $b = -0.26 \pm 0.07_{\text{stat}} \pm 0.2_{\text{syst}}$. Above 1 TeV the spectrum can be fitted well

with a pure power-law (Weekes et al., 1989; Aharonian et al., 2004), which is not the case for lower energy.

The measured spectral index varies in good agreement with the prediction made by Aharonian et al. (2004) (see above). The GeV γ-ray emission has a peak in the SED-representation. While the spectrum around the peak should be curved, the peak can be calculated from the measurements of the spectral index from the curved power-law fit, and one gets $77 \pm 47_{\mathrm{stat}}{}^{+107}_{-46\ \mathrm{syst}}$ (Albert et al., 2008a).

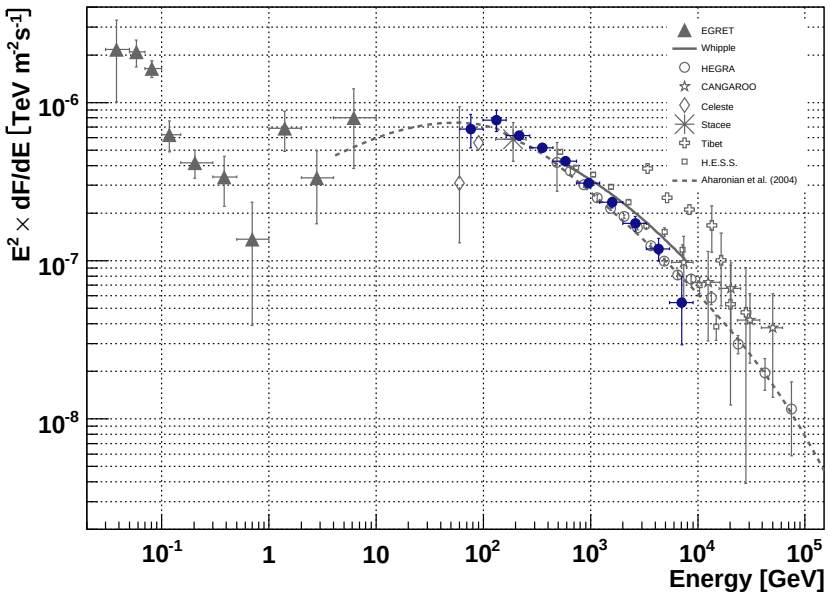

Figure 4.10: The spectral energy distribution for the Crab Nebula together with the results obtained by different experiments.

As pointed out in the beginning, the Crab Nebula is a stable, i.e. has constant flux. Fig. 4.11 shows the average flux of every observation night with a statistical uncertainty of ~ 20 % (the blue shaded region). The dashed line represents the average flux of all nights $F_{>200\mathrm{GeV}}$, with the value (Albert et al., 2008a)

$$F_{>200\mathrm{GeV}} = (1.96 \pm 0.05_{\mathrm{stat}}) \times 10^{-10}\ \mathrm{cm}^{-2}\ \mathrm{s}^{-1}. \tag{4.11}$$

The probability that the flux is constant, is 67%, i.e. from 10 nights 3 will have lower or higher fluxes. Thus, one can conclude that the reconstructed flux was, within statistical errors, constant during the observation time.

The range of the emission region can be also computed and one finds at ~ 250 GeV an upper limit of the emission region of 2.4' and at ~ 500 GeV an upper limit of 1.6'. This last value is four times larger than the predicted size of the inverse Compton surface brightness for γ-ray energies below 500 GeV (de Jager and Harding, 1992).

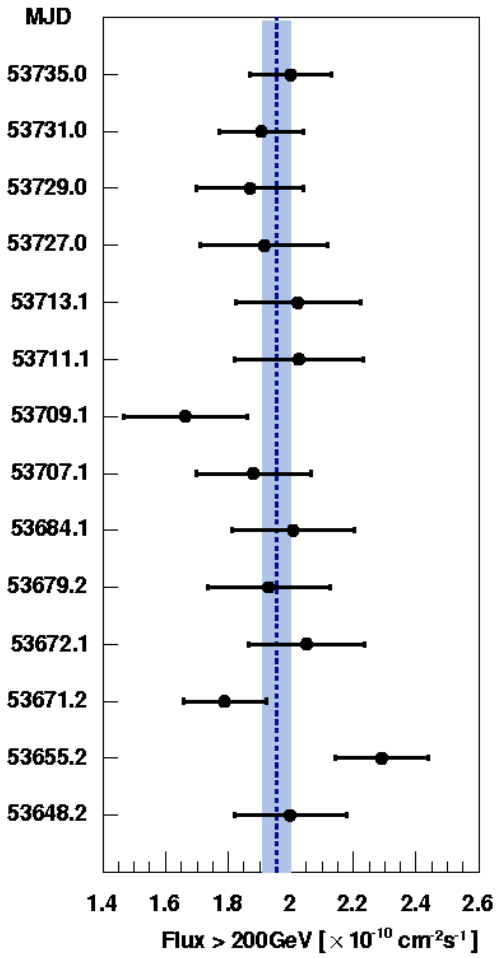

Figure 4.11: The light curve for the Crab Nebula for a flux above 200 GeV for every individual night. The dashed line represents the average flux for all the nights, whereas the blue shaded region represents the statistical errors (Albert et al., 2008a).

Chapter 5

The spectrum of AGN at very high energies

It is well known that the highest energies produced in the astronomical objects, exceed by far the energies one can obtain with manmade particle accelerators. Although the mechanisms observed in the astronomical phenomena cannot be controlled, they offer a unique opportunity to understand the physics at VHE.

In what follows, the most important characteristics of the spectrum of AGN are presented using the previously described unfolding method. For this, the blazars Markarian 421 (Mrk 421), Markarian 501 (Mrk 501) and PKS 2155-304 were chosen.

5.1 Mrk421

The blazar Mrk421 hosted by a S type galaxy at a redshift of $z = 0.0031$ with a visual brightness of 13.3 mag, is the nearest known AGN and together with Mrk 501, the best studied sources of TeV γ-ray. Moreover, it was the first AGN detected at high energies using imaging atmospheric Čerenkov telescopes (Punch et al., 1992; Petry et al., 1996). It was observed to be one of the strongest emitting VHE γ-ray sources with very high flux variations compared to other blazars. The flux can increase more than one order of magnitude and doubles in around 15 minutes (Gaidos et al., 1996; Aharonian et al., 2002).

In the radio, see Fig. 1, Mrk 421 could not be resolved at 22 GHz within a core size of 0.15 milliarcsecond (mas) or 0.1 pc (Zhang and Baath, 1991; Charlot et al., 2006). In the '90s a weak one-sided jet starting about 5 mas from the core could be detected (Polatidis et al., 1995; Kellermann et al., 1998). From this observation, it was possible to determine that the viewing angle is less then 30° and the apparent jet speed is between ∼0.8c and 1c (Giovannini et al., 1999). More recent data have decreased the value of the jet speed to 0.4c (Kellermann et al., 2004) and 0.1±0.02c (Piner and Edwards, 2005). Such small apparent values for the speed of the jet was observed in other blazars as well and have two possible explanations. First, the Doppler factor decreases along the jet due to jet curvature or deceleration. Second, the measured speed is not that of the jet itself but the speed of a perturbed pattern in the jet.

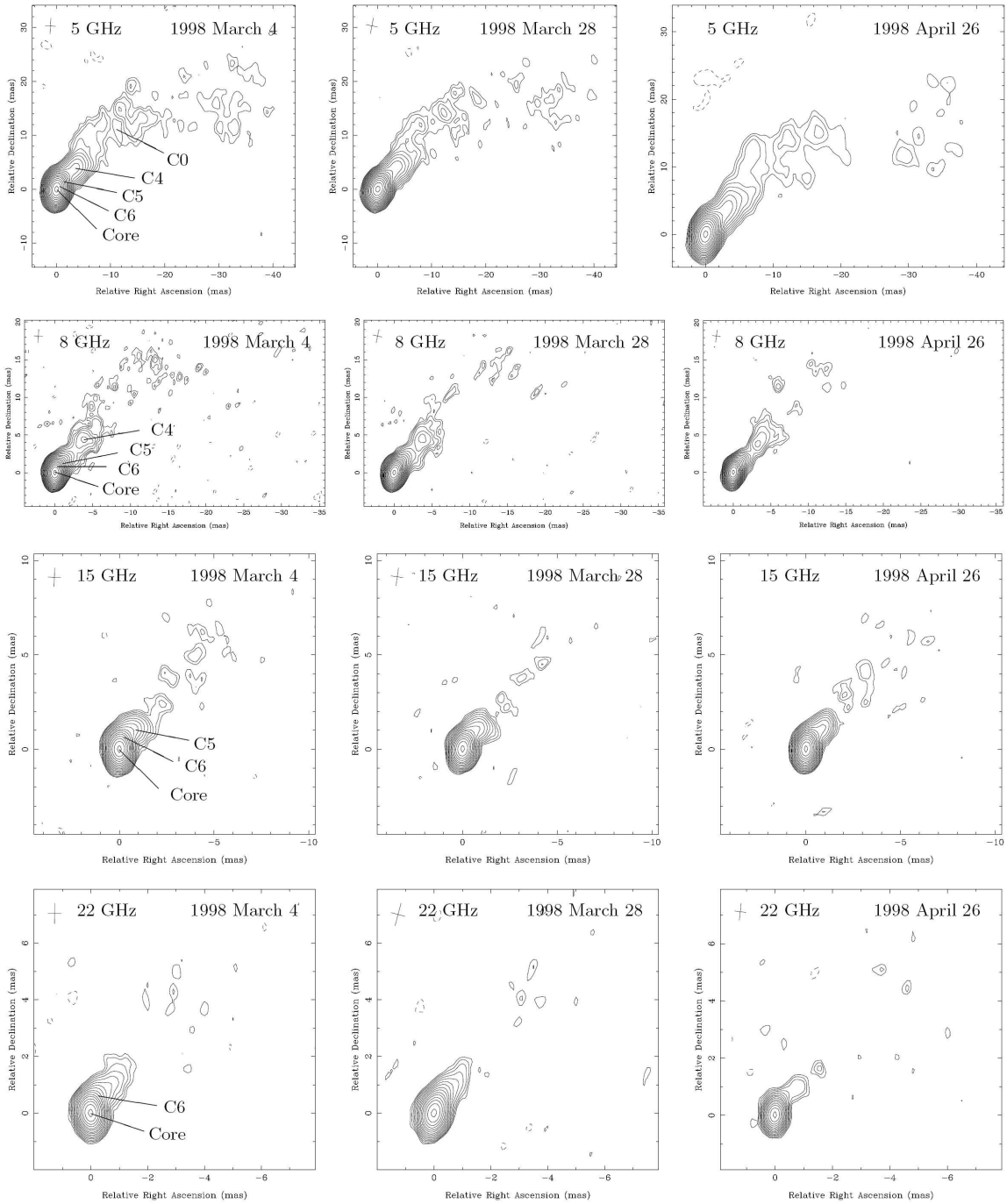

Figure 5.1: Total intensity maps of Mrk421 in the radio band at four different wavelengths (from upper to lower panels: 5 GHz, 8.4 GHz, 15 GHz, and 22.2 GHz) and three different epochs (from from left to right: 4 March, 28 March, and 26 April 1998) (Charlot et al., 2006).

In the later case one expects that the radio core is still efficiently boosted but without evidence for relativistic beaming from apparent motion in the radio jet. In this case a connection between the radio core and the high energy range is expected. Such a connection can be attributed to X-rays and γ-rays of AGN when new radio components occur (Krichbaum et al., 1998; Marchenko et al., 2000) and is specially true for Mrk 421 which shows sometimes multi-spectral flares (Katarzyński et al., 2003).

Together with the core, several long-lived jet components were also detected (Piner et al., 1999; Charlot et al., 2006) as can be seen in Fig. 5.1. The closest component C6 is only ∼0.87 mas from the core, while the most distant component observed C0 is at a distance of ∼15.42 mas. It was also possible to measure the speed for the first three jet components near the core of Mrk 421, i.e. 0.089c for C4, 0.095c for C5 and 0.029 for C6. There is no evidence in the variability of the fluxes or polarization of the jet components. But for the core, both total flux and polarized flux showed a variability at all observed frequencies (Charlot et al., 2006). Moreover, it was observed that such variability is connected with the polarization of the core, i.e. after the total flux of the core decreased by 10-20% in nearly two months, the decrease was followed by a rotation of the polarization angle with 30-60° at nearly all frequencies (8, 15 and 22 GHz).

To study Mrk 421 at high energies, data was taken with the MAGIC Telescope during April 2005. The data was taken in the Wobble mode analyzed with three off-regions and accumulate ∼ 9 hours of data. Due to good weather conditions, only a few runs were rejected to ensure a stable rate of ∼ 270 Hz during the entire observation time. The observation was taken at low zenith angles , 10°-13°, which ensures a low trigger energy threshold. For calibration and image cleaning, the standard cuts for the MAGIC Telescope were used (Bretz 2006,Tescaro et al. 2007).

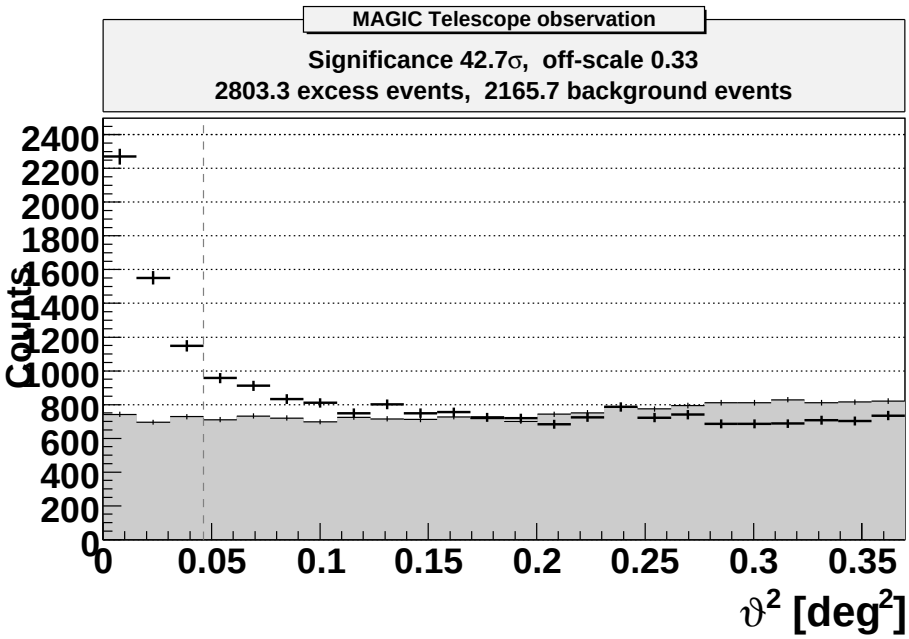

Figure 5.2: The signal for Markarian 421. The black points represent the On-data, whereas the gray region are the Off-data. The inconsistence between data and Background ($\theta^2 > 0.25$) is due to the three Off-region used for the analysis. The off-scale, which represents the ratio of On-time and Off-time, is also shown in the plot.

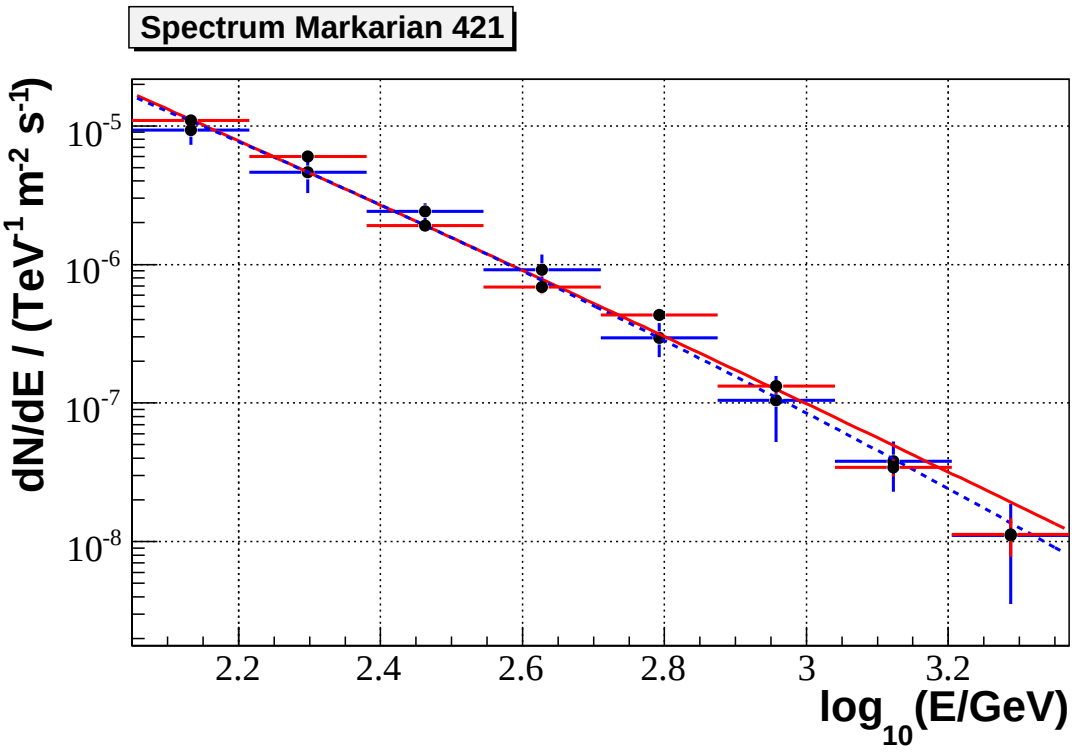

Figure 5.3: The spectrum for Markarian 421. Blue points represents the unfolding results, red points are the unfolding results obtained with the same data by (Albert et al., 2007a). The red curve represents the fit for the red points, the blue line the fit for the blue points.

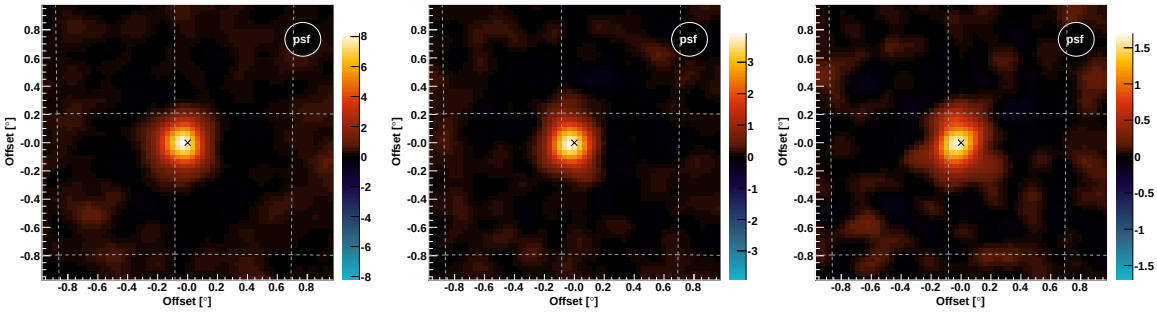

Figure 5.4: The Sky plot for Markarian 421 with different *Size* cuts applied. The left plot includes all showers with $Size < 1000$ phe, the middle plot $1000 < Size < 1400$ and the right plot $1400 < Size < 1800$.

The signal found in the data, see Fig. 5.2, is of 42.7 σ with 2803 excess events and 2166 Background events at an energy threshold of 193 GeV. The inconsistency between the data and the Background for $\vartheta^2 > 0.25$ in Fig. 5.2 is due to the three off-regions used and the high flux of Mrk 421. Such a high significance can be obtained only by lowering the cut-efficiency which raises the energy threshold. Thus for the energy spectrum one needs to increase the cut-efficiency to typical values around 60%. The cuts used to increase the cut-efficiency imply a new threshold at 163 GeV, with

2383 excess events and 1360 background events. The same cuts were used afterwards for the Monte Carlo.

The resulting spectrum is shown in Fig. 5.3. The Red points and the red line represent the results and the fit from Albert et al. (2007a), whereas the blue points are the results obtained with the new unfolding method. The blue dashed line represents the fit for the blue points and is a good estimation also for the red one. The spectral index of the spectrum described by the blue dashed line follows a curved power law given by

$$\frac{dN}{dE} = N_0 \left(\frac{E[\mathrm{TeV}]}{0.25\mathrm{TeV}} \right)^{-\Gamma} \quad \text{with} \quad \Gamma = a + b \cdot \log_{10} \left(\frac{E[\mathrm{TeV}]}{0.25\mathrm{TeV}} \right), \tag{5.1}$$

where $N_0 = (7.71 \pm 0.38) \cdot 10^{-6}$ (TeV m^2 s)$^{-1}$, $a = 2.3 \pm 0.09$ and $b = 0.24 \pm 0.09$.

Mrk 421 appears in the TeV regime as a point-like source as in the radio regimes. This is easy to notice in Fig. 5.4 which shows the sky plot of excess events for different $Size$, i.e. energy, regime. Such a characteristic is true for all observed blazars.

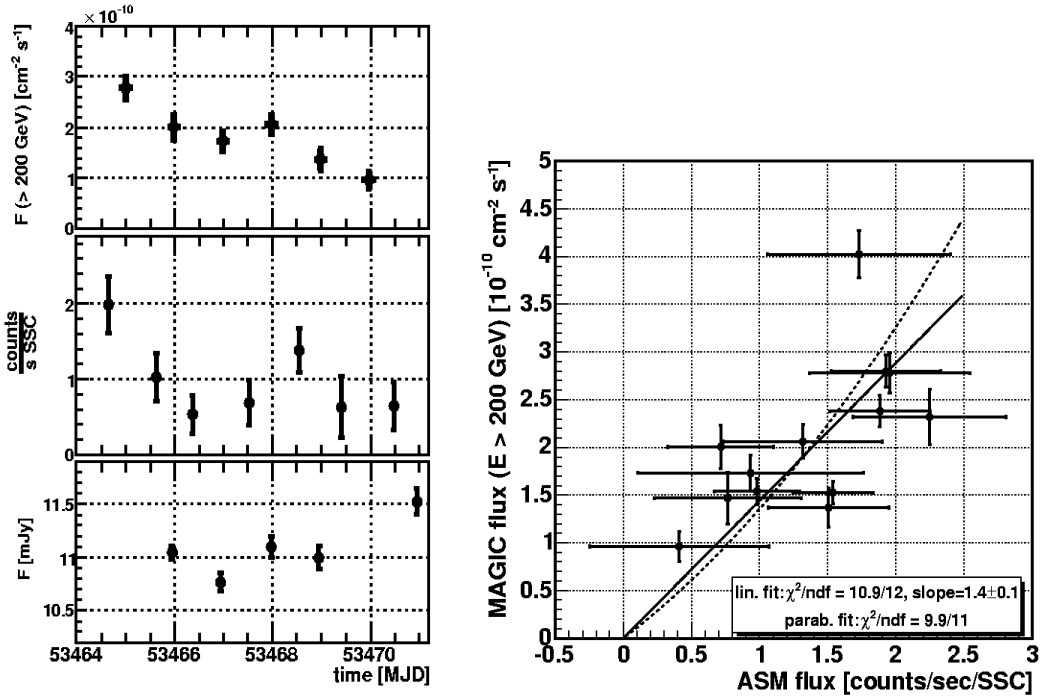

Figure 5.5: On the left the light curve for Mrk 421 at three different regimes. On the top in the TeV regime for every observation night. In the middle the X-ray regime observed by All Sky Monitoring for the same nights. On the bottom, Mrk 421 in the optical. On the right part, the correlation between the TeV and the X-ray data is shown. A clear correlation could be identify (Albert et al., 2007a)

The light curve shown in Fig. 5.5 indicates the flux above 200 GeV for each one of the 6 days of observation. To enlarge the limit for the energy threshold makes sure that the result is independent of the actual trigger threshold during each night. The flux is decreased by a factor of three from the first to the last day, a clear signal of variation. In addition to the light curve above 200 GeV in the left side of the Fig. 5.5 the light curve in X-ray measured by All Sky Monitoring (ASM) and optical data taken by KVA telescope on La Palma are shown. A clear correlation exists between the measured γ-ray and X-ray fluxes as shown on the right side of Fig. 5.5 (which also includes some

observation points from November). Both fits, linear and parabolic, have the same χ^2 probability of 54%, which implies a 2.4 σ correlation.

5.2 Mrk501

At $z = 0.034$ only a few Mpc away from Mrk 421, one finds another important blazar, Mrk 501. It was the second blazar discovered after Mrk 421, being together with Mrk 421, the strongest TeV sources in the sky (Quinn et al. 1996; Bradbury et al. 1997). One year after the discovery, Mrk 501 showed in the TeV range an increase in the flux of more than one order of magnitude (Aharonian et al., 1999). Moreover, with the MAGIC telescope, the flux doubling time was observed to be as short as $\sim$ 2 minutes (Albert et al., 2007b).

The morphology of Mrk 501 in the radio regime at large scale has a two-sided diffuse emission oriented at $\sim 45^\circ$ which indicates that the jets are not relativistic at a distance of $\sim$ 10 kpc from the core (Giroletti et al., 2004). At lower (mas) scale, Mrk 501 shows a strong core and a one-sided jet which originates at a distance below 1 mas, i.e $\sim$ 0.7 pc. The jet shows multiple sharp bending before undergoing a last turn ending with a rapid expansion. Near the core, the jet has a very bright structure and changes its direction several times. The brightness is not uniform, having a deep minimum (5-6 mas) and a high maximum (8-9 mas) very close together. Between 10 and 30 mas, the jet starts to lose its collimation and is visible only in lower resolution images. Moreover, the spectrum of the inner region of the jet is flatter than the one obtained from the outer region. At even larger distances from the core, the jet has a strong bending and a large opening angle, the orientation in this region of the jet coincides with the jet at large scale, i.e 43°. So far it remains unknown why the jet has such a changing structure.

As in the case of Mrk 421, it was possible to resolve the jet sufficiently well to observe jet components as shown in Fig. 5.6. Unfortunately, the jet components are observable only at high frequencies and no proper motion was found for its components (Giroletti et al., 2004). An explanation for such an observation is given by Doppler factors which can differ in the jet from region to region, such that inner high velocities could be de-boosted while a slower external layer could be less de-boosted or even boosted. The jet/contrajet ratio given by equation (3.48), assuming that $\alpha = 0.5$, $\beta > 0.89$ and $\theta < 27^\circ$, is higher than 70 at a distance of 60 mas from the core. This implies that the jet remains relativistic even at large distances from the core. This is in agreement with the bulk velocity which is strongly relativistic near the core $\Gamma \sim 15$ and decreases to $\Gamma \sim 1.25$ at 100 mas if the magnetic field is parallel or to $\Gamma \sim 7$ if the magnetic field is perpendicular (Giroletti et al., 2004).

The peak frequency in the radio was measured to be 8.4 GHz with the corresponding peak flux density of 0.55 mJy. This implies, at a distance of 0.15pc from the core a magnetic field of $b \sim 0.03$ G (Giroletti et al., 2004). From higher state measurements (Katarzyński et al., 2001) the magnetic field was found to vary between 0.02 and 0.2 G in the region < 0.03 pc. For the jet components, the magnetic field is of the order of ~ 0.015 G.

Normal monitoring (few weeks) of Mrk 501 showed a variation of the flux above 200 GeV nearly every night. Observation during the nights of the 30-th of June and the 9-th of July of 2006 have both indicated a flaring state for Mrk 501. The data was taken in On-Off modus providing 15.7 minutes On-data and 24.1 minutes Off-data for the night in June, and 45.5 minutes On-data and 50 minutes Off-data for the night in July. The only quality cuts applied to the data were for the rate, such that the observation rate remains stable at 277 Hz for the night of the 30-th of June and 300 Hz for the night of the 9-th of July.

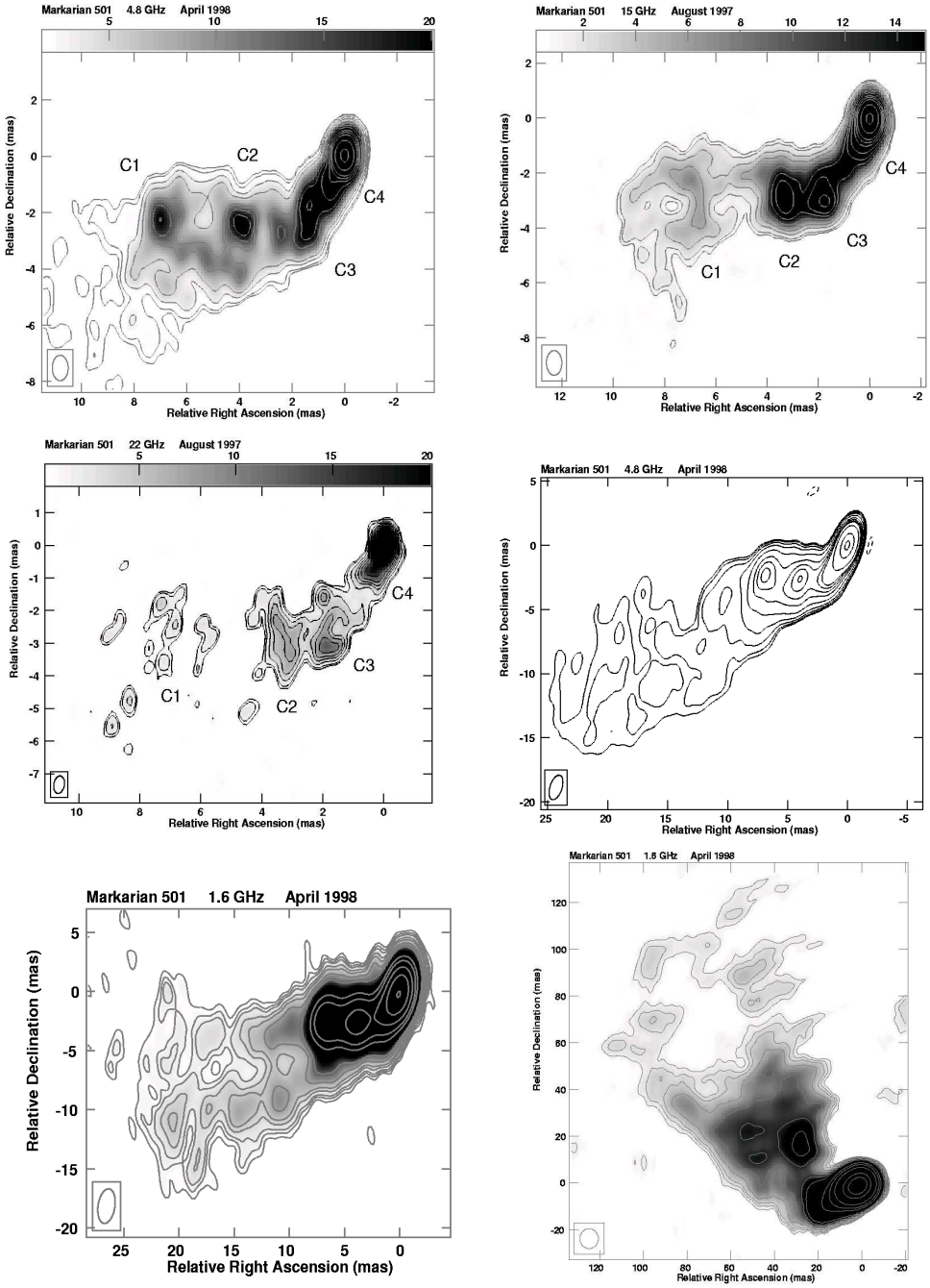

Figure 5.6: Markarian 501 in the radio band at different frequencies (1.6 GHz, 4.8 GHz, 15 GHz, and 22.2 GHz) showing the complex structure of the jet from the small scale (top) to the larger scale (bottom) (Giroletti et al., 2004).

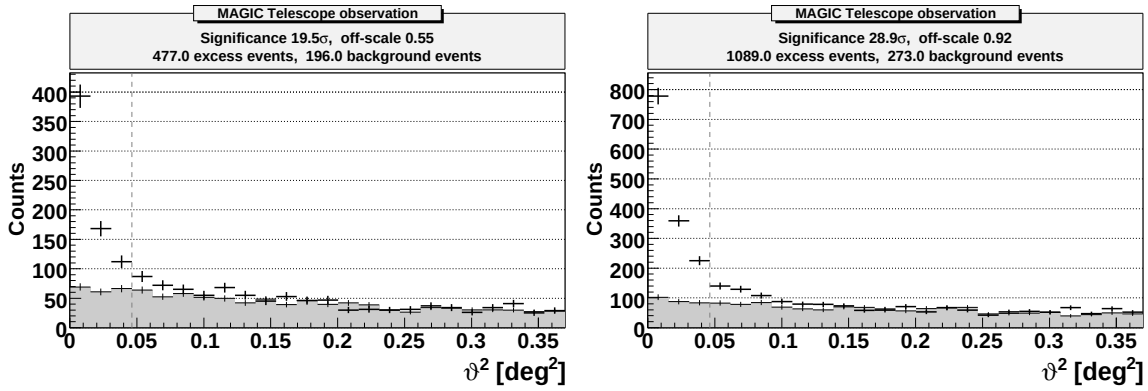

Figure 5.7: The signal for Mrk 501 for the night of the 30-th of June and the 9-th of July as used for the spectrum.

After standard cuts for calibration and image cleaning were applied to the data for each night, the significance was determined to be of 19.5 σ corresponding to 477 excess events and 196 Background events for the 30-th of June and 28.9 σ with 1089 excess events and 273 Background events for the 9-th of July as shown in Fig. 5.7. For the spectrum, the cuts were modified to obtain a cut-efficiency around 65%. This changed the threshold for both nights from 196 GeV to 140 GeV.

The result of the unfolding is shown in Fig. 5.8, for the 30-th of June on the left side and the 9-th of July on the right side. The blue points represent the spectrum obtained with the probability method and the blue dashed line is the fit. The red points represent the spectrum obtained for the same data by Albert et al. (2007b). The spectral slope of both nights is a curved power law of the form

$$\frac{dN}{dE} = N_0 \left(\frac{E[\mathrm{TeV}]}{0.3\mathrm{TeV}}\right)^{-\Gamma} \quad \text{with} \quad \Gamma = a + b \cdot \log_{10}\left(\frac{E[\mathrm{TeV}]}{0.3\mathrm{TeV}}\right), \tag{5.2}$$

where $N_0 = (1.86 \pm 0.06) \cdot 10^{-6}$ (TeV m^2 s)$^{-1}$, $a = 1.9 \pm 0.08$ and $b = 0.43 \pm 0.12$ for the 30-th of June and $N_0 = (1.55 \pm 0.07) \cdot 10^{-6}$ (TeV m^2 s)$^{-1}$, $a = 2.06 \pm 0.1$ and $b = 0.4 \pm 0.14$ for the 9-th of July, and are in very good agreement with the result of Albert et al. (2007b). In addition to the previous result, the spectrum could be extended for the night of the 9-th of July with an extra point at 5.9 TeV.

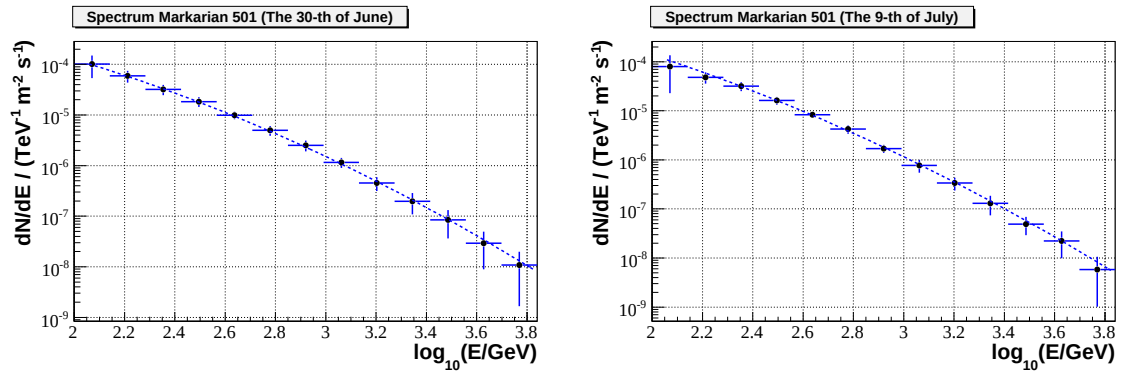

Figure 5.8: The spectrum for Mrk 501 for the night of the 30-th of June on the left side and the 9-th of July on the right side.

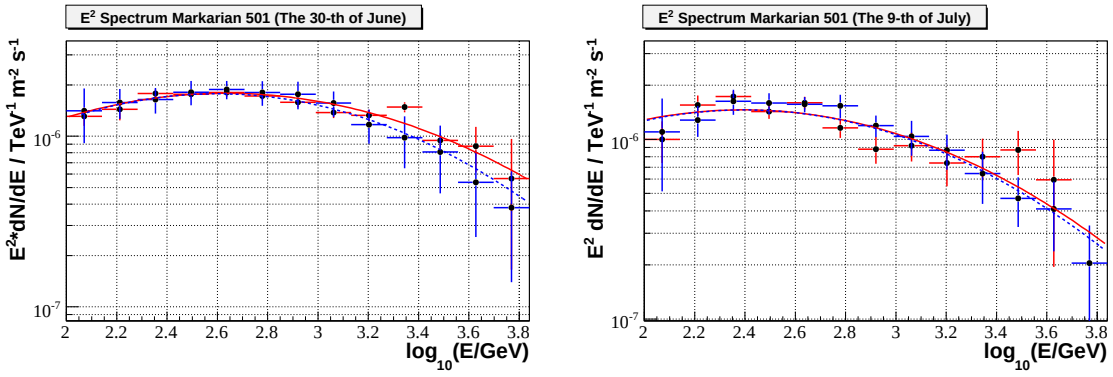

Figure 5.9: On the left, the spectrum for Mrk 501 for the night of the 30-th of June in blue with the probability method, in red from Albert et al. (2007b) with the associated fitting curves. On the right, the unfolding result for the night of the 9-th of July. The points have the same meaning as before.

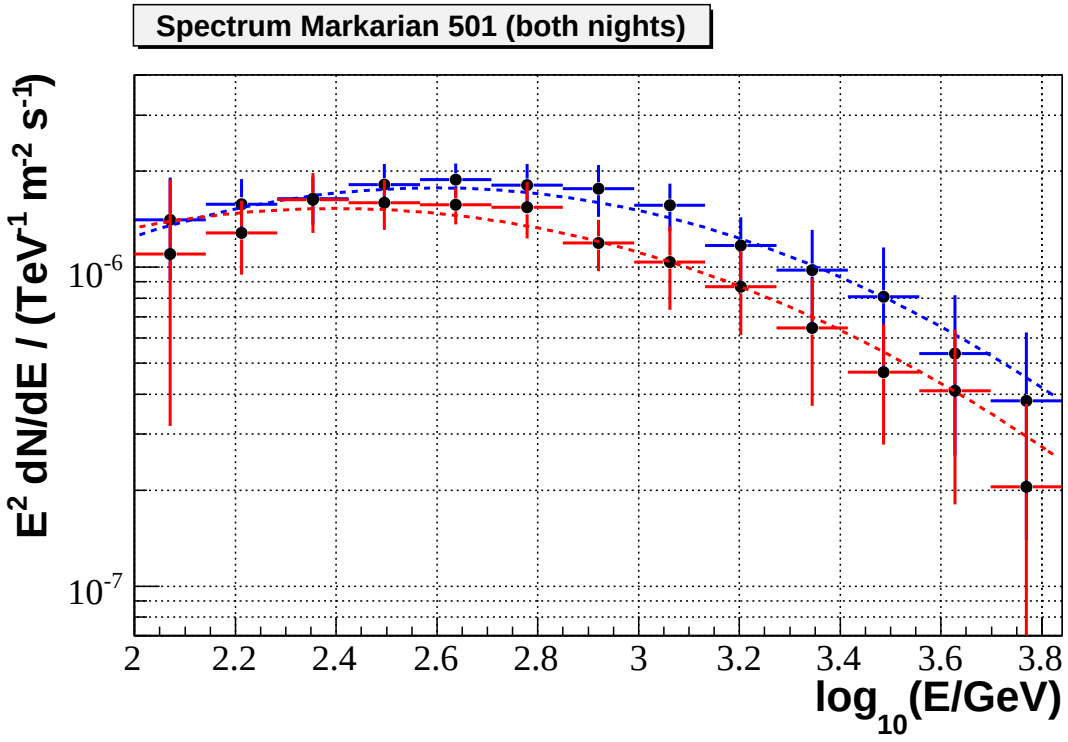

Figure 5.10: The spectrum for Mrk 501 for the night of the 30-th of June (blue) and of the 9-th of July (red). The blue and red curves represent the associated fits. The different peaks of the two nights can be seen very clearly as well as the increase of both, the peak values and the flux peak energy.

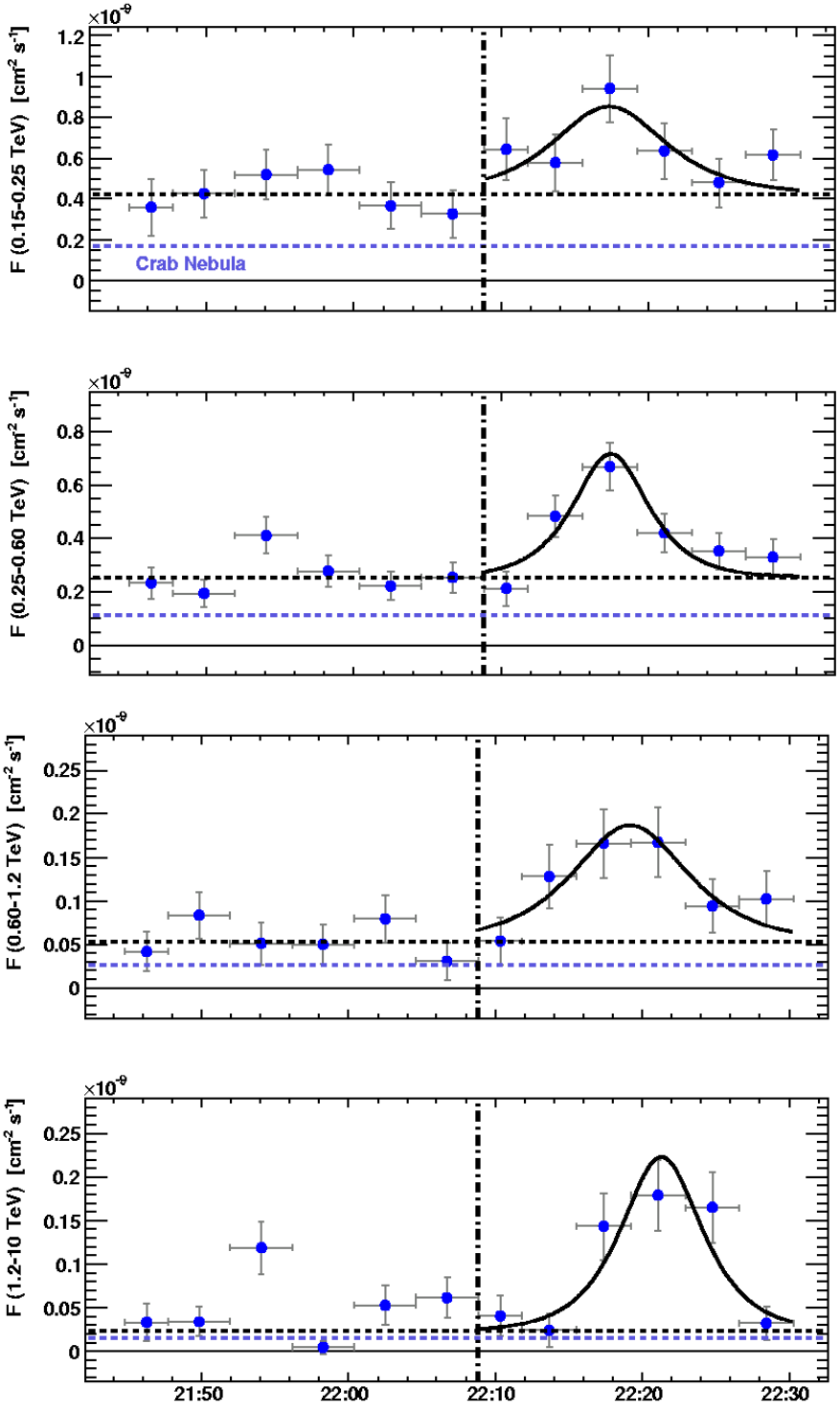

Figure 5.11: The light curve for Mrk 501 for the night of the 9-th of July at different flux ranges. From top to bottom: 0.15-0.25 TeV, 0.25-0.6 TeV, 0.6-1.2 TeV, and 1.2-10 TeV (Albert et al., 2007b).

To emphasize simpler the importance of the two observed flares of Mrk 501 it is convenient to plot the obtained spectrum in a slightly different way, by multiplying the spectrum with the square of the energy E^2, as shown for both nights in Fig. 5.10. The red points and line represent the spectrum and fit from Albert et al. (2007b). One immediately sees that in this representation the spectrum gets curved and the peak of the inverse Compton (IC) becomes visible. Moreover, two important remarks can be made.

- The peak of the energy spectrum (IC regime) changes with the flaring nights from a peak energy of 250 ± 70 GeV for the 9-th of July to 400± 60 GeV for the 30-th of June.
- The peak also moves in the energy (frequency) of the γ-ray; $(1.53 \pm 0.09) \cdot 10^{-6}$ (TeV m^2 s)$^{-1}$ for the 9-th of July to $(1.76 \pm 0.08) \cdot 10^{-6}$ (TeV m^2 s)$^{-1}$ for the 30-th of June.

The light curve for the night of the 9-th of July is shown in Fig. 5.11 and indicates two important characteristics. First, the short timing of the flare of the order of ~ 2 minutes within which the flux is doubled. Second, the light curve between different energy ranges shows energy dependent time delays in the peak flare emission.

Such observations indicate for several phenomena, on one hand one can see the delay as different acceleration rates of the electrons at different energies, on the other hand one can invoke quantum effects to explain its delay. This implies that the spacetime continuum is not smooth and γ-rays at higher energies (smaller wavelengths) will start to feel this effect and will need to travel a longer distance to Earth. Such calculation indicate a possible quantum effect with 2 σ (Albert et al., 2007c). Another way to interpret the delay is that the blob where the acceleration takes place has a nonconstant velocity (Bednarek and Wagner, 2008).

5.3 PKS 2155-304

The blazar PKS 2155-304, at redshift $z = 0.117$, was first detected in the TeV range in 1997 (Chadwick et al. 1999; Chiappetti et al. 1999) and confirmed by the H.E.S.S. (Djannati-Atai et al., 2003) and MAGIC collaborations (Hadasch et al., 2008). In comparison to the Markarian blazars, PKS 2155-304 is not well studied in the radio but in the optical bands. The reason for the poor radio data is the large distance of PKS 2155-304 where the small resolution window is of 0.5 mas, i.e. 1 pc at an observation frequency of 15 GHz.

The jet of PKS 2155-304 appears in radio with a smooth profile starting at 1 mas from the core and becomes broader and more diffuse before bending again around 3 mas and is oriented with an angle of $\sim 150°$. Due to limited resolutions one cannot distinguish between a series of distinct components of the jet near the core or a sum of appropriate discrete Gaussian, i.e. minima and maxima in the brightness of the jet. Such similarity with the jet structure of Mrk 421 and Mrk 501 is the only reason why discrete Gaussian are more accepted, although a power law (after the Gaussian for the core was subtracted) fits the data with the same probability (Piner and Edwards, 2004). It was still possible to detect a component C1 inside the jet which moved from 0.53 mas to 0.71 mas during the three epochs of observation as shown in Fig. 5.12. As in the case of Mrk 501, no significant motion thus no correlation between the radio components and TeV activity was found by Piner and Edwards (2004).

The radio flux of the core of PKS 2155-304 showed variation during the three epochs observed by Piner and Edwards (2004) from 205 mJy for the first epoch decreasing to 136 mJy to reach, finally, 165 mJy at the end of the observation time. It is possible to use the flux to calculate the

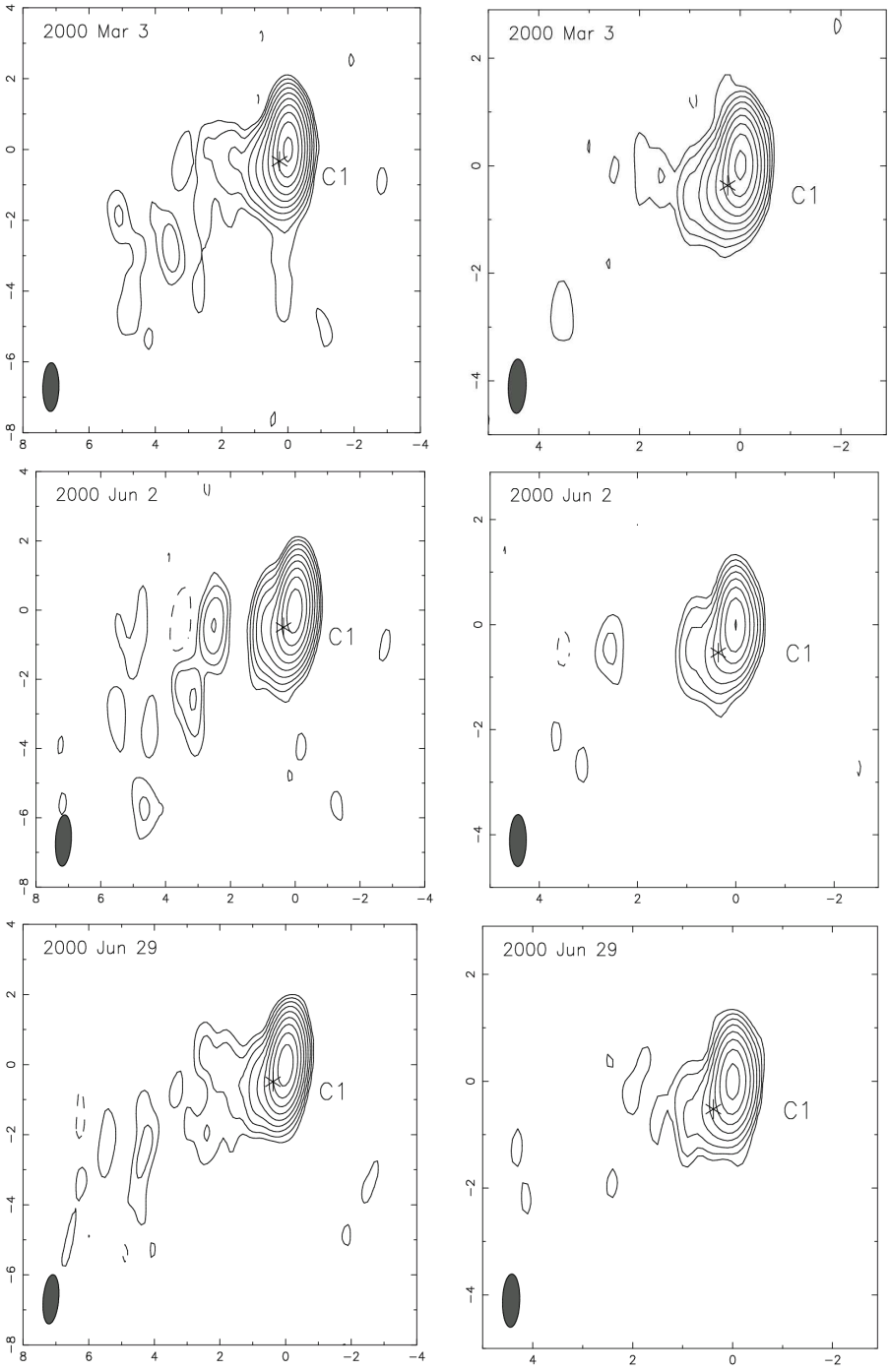

Figure 5.12: PKS 2155-304 in the radio band at a frequency of 15 GHz and three different epochs (from upper to lower panels: 3-th March, 2-nd June, and 29-th June 2000). On the left the data with an uvweight=0.2 and on the right with an uvweight=2.0 (Piner and Edwards, 2004).

brightness temperature as $T_B = 1.22 \cdot 10^{12} \frac{S(1+z)}{a^2 \nu^2}$, with S being the measured flux, z the redshift, a the full width at half maximum of the circular Gaussian and ν the observation frequency in GHz. Observed brightness temperatures are amplified by a Doppler factor and can lie above physical limits. Therefore the temperature can be a simple estimation for the Doppler factor. The mean brightness temperature computed for PKS 2155-305 was few times 10^{10} K, which implies small Doppler factors.

Variation in the light curves of PKS 2155-304 were observed also in the optical bands. During the observation of several years (1996 until 1999), a dimming was first observed in the first two years of observation followed by an irregular behavior in the last observation time with rapid variation (Dominici et al., 2004). Such variation, even intraday, were already observed before (Paltani et al., 1997). However, the flux density showed no significant changes during the observation time with the exception of 1999 when the light curve showed sharp dips with a duration of two days. The same period provided sufficient statistics to allow a slight correlation with the X-ray data, but without any indication of delays (brightness variation). Synchrotron fitting showed a changing of the peak frequency from $7.9 \cdot 10^{15}$ Hz in 1996 to $1.3 \cdot 10^{16}$ Hz in 1997 to return to $5 \cdot 10^{15}$ Hz in 1999.

At very high energies, PKS 2155-304 was observed by the H.E.S.S. collaboration in flaring state on July 2006 triggering the MAGIC collaboration to observe the source. While the H.E.S.S. observation was at low zenith angles, the observation performed with the MAGIC telescope was at very large zenith angles, more exactly, between 59° and 67°. Such large zenith angles imply higher energy threshold and a lower detection rate. The data was taken in wobble mode between the 18-th of July and the 2-nd of August 2006 and accumulated 12.7 hours of observation. Multiple quality-cuts were applied to get rid of bad data due to weather conditions, outlier in calibration pulse positions and of runs with abnormal observation rate. Data, with a zenith angle larger than 64°, was rejected due to missing Monte Carlo at that large zenith angle. After the quality-cuts only 8.1 hours of data remained.

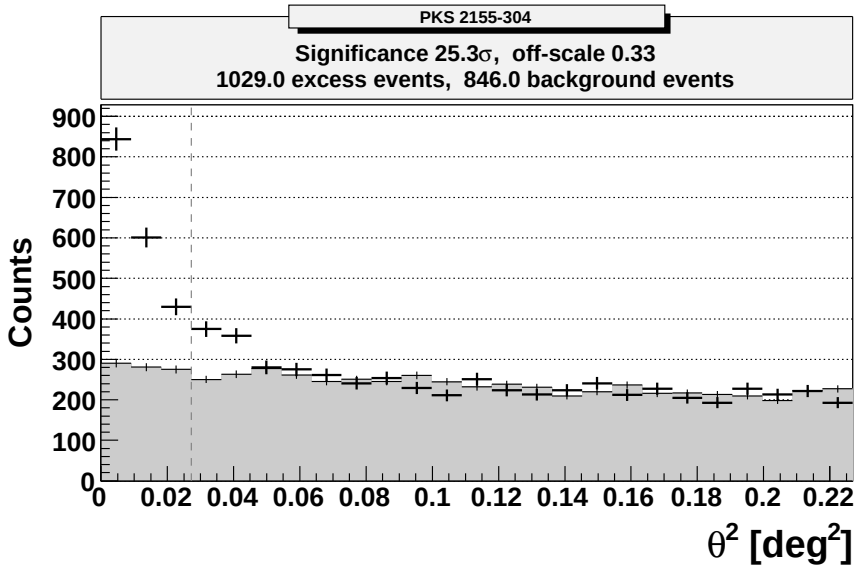

Figure 5.13: The signal for PKS 2155-304.

Due to the high zenith angle at which the source was observed, a special area cut, i.e. inversion of the parabola cut (see §1.5.4), was used to analyze the data permiting the inclusion of low energy events[1]. Additionally, a *Size* cut was done for all events below 80 phe. At the end of the analysis, a clear signal was observed of 25.3 σ with 1029 excess events and 846 Background events as shown

[1]For more details of the analysis see the diploma thesis of Hadasch (2008).

in Fig. 5.13. The energy threshold of this analysis was determined to be 362 GeV. The unfolded spectrum obtained from the analyzed data is shown in Fig. 5.14. The blue points represent the result obtained with the probability unfolding method, whereas the red points represent the unfolded spectrum with the MAGIC unfolding. Again the probability unfolding method delivered an extended spectrum with one additional bin on both the higher and lower part of the spectrum. A fit of the obtained spectrum with a simple power law indicated a lower probability than a broken power law, as emphasized in Fig. 5.14. The blue dashed line is a fit for the first three points of the spectrum with a slope of $\Gamma_1 = -2.83 \pm 0.18$, whereas the black dashed line is the fit for the rest of the spectrum with a slope of $\Gamma_2 = -3.63 \pm 0.12$. The slope of the energy spectrum changes at ~ 400 GeV being in very good agreement with the result of Aharonian et al. (2007) of ~ 430 GeV. The red line is the fit for the red points with a slope of -3.49 ± 0.2. Although the first two points have a very low significance, the spectrum could be reconstructed even for such low energies (down to ~ 150 GeV) although the additional *Size* cut was applied.

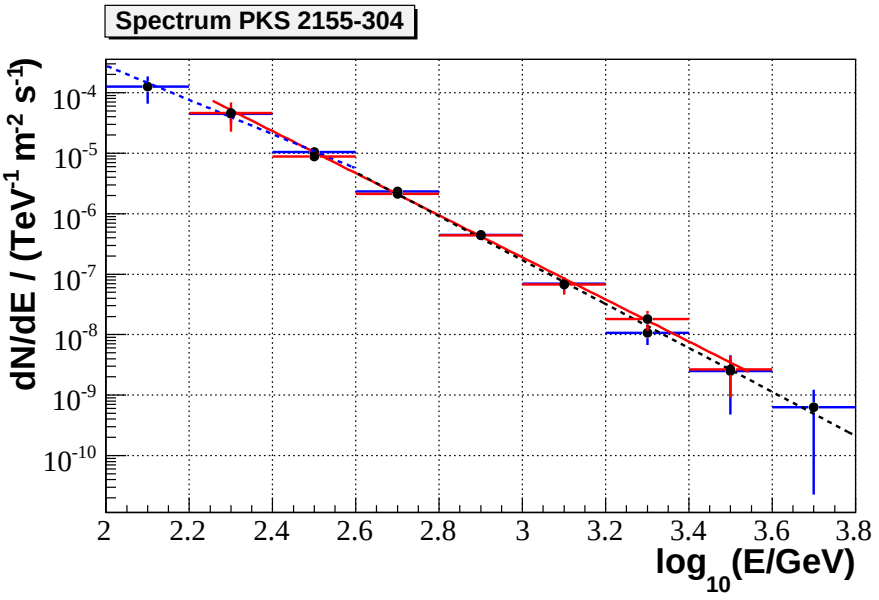

Figure 5.14: The spectrum for PKS 2155-304. Blue points represent the spectrum obtained with the probability unfolding method, in red the spectrum obtained by an alternative unfolding method. The blue and black lines represent the fit for the blue points, whereas the red line is the fit for the red points. One can remark that the red points lie well on the fit for the spectrum in blue.

A second analysis was performed without the *Size* cut. The resulting spectrum obtained with the probability method is shown in Fig. 5.15. The blue points represent the spectrum obtained before with the *Size* cut, whereas the red points represent the spectrum without the *Size* cut. In the latter case the spectrum at lower energies became softer, i.e. with a smaller slope of -2.61 ± 0.21 emphasized with the red dashed line. Both spectra agree very well, within the errors, with the spectrum obtained by Aharonian et al. (2007). Because Aharonian et al. (2007) observed PKS 2155-304 in flaring state, the flux is about one order of magnitude higher and thus not shown in Fig. 5.15.

The origin of the discrepancy between the two spectra can be traced clearly to the zenith angle, which is shown in the left side of Fig. 5.16. The blue distribution represents the data without the *Size* cut, whereas the red distribution stands for the data with the *Size* cut in both plots of Fig. 5.16. To make sure that no statistical fluctuations in the data will alter the result, 500 runs were used for

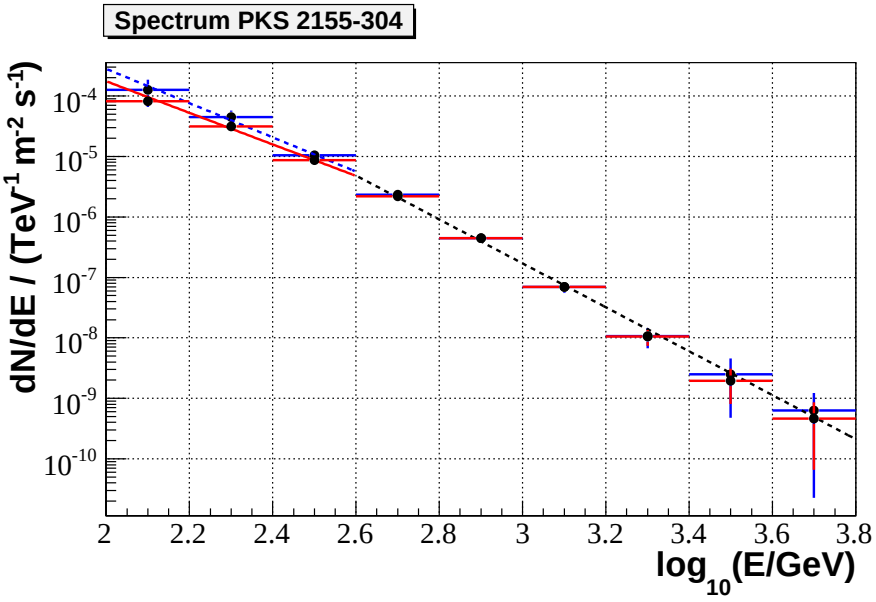

Figure 5.15: The spectrum for PKS 2155-304 obtained with the *Size* cut (blue) or without the *Size* cut (red). The blue and black lines have the same meaning as in Fig. 5.14, and the red line is the fit for the first three red points.

each bin. The right side of Fig. 5.16 shows the Monte Carlo distribution of the energy for both data analysis. The high value of the zenith angle of the observation is the reason why such a low cut in *Size* still affects events with $\sim$ 400 GeV as can be seen from the two distributions for the energy, on the right side of the Fig. 5.16. The important information is given by the π_5 plot, which shows clearly a shifting of the range of the zenith angle from 0 for the additional *Size* cut to 3 for the data without the *Size* cut. Therefore, the data with the *Size* cut does not contain information about the zenith angle anymore, whereas the data without the *Size* cut still preserves this information. This effect of the cuts, i.e. to eliminate the influence of the zenith angle, is responsible for the softening of the spectrum at lower energies.

In this way, the usefulness of the π_5 plots is emphasized, indicating how cuts affect the data by means of the parameters used in the unfolding. Moreover, one can use such information as a measure of how much cuts can affect the Hillas parameters, thus one is offered the opportunity to control the effects of the cuts on the data. Under these specification both analysis are correct, one needs only to decide whether the zenith angle is indeed important for observations at very high zenith angles or not. To decide for one of the two cases is not an easy task, since such observations were performed for the first time by the MAGIC telescope. Monte Carlo simulations are not very well studied at this range of the zenith angle, but the results obtained for the Crab Nebula at such a high zenith angle turned out to be consistent with results established at lower zenith angle (Hadasch, 2008).

The light curves of PKS 2155-304 for both observations, i.e. by H.E.S.S. and by MAGIC, are shown in Fig. 5.17. The plot on the top shows an increase of the flux by a factor of four during the multiple flares, i.e. every individual peak in the light curve. Every point is in one minute interval, and the dashed line represents the Crab flux. The bottom plot shows the light curve for PKS 2155-304 as observed by MAGIC. Every point is in $\sim$ 15 minutes interval, and a variability was observed (second night).

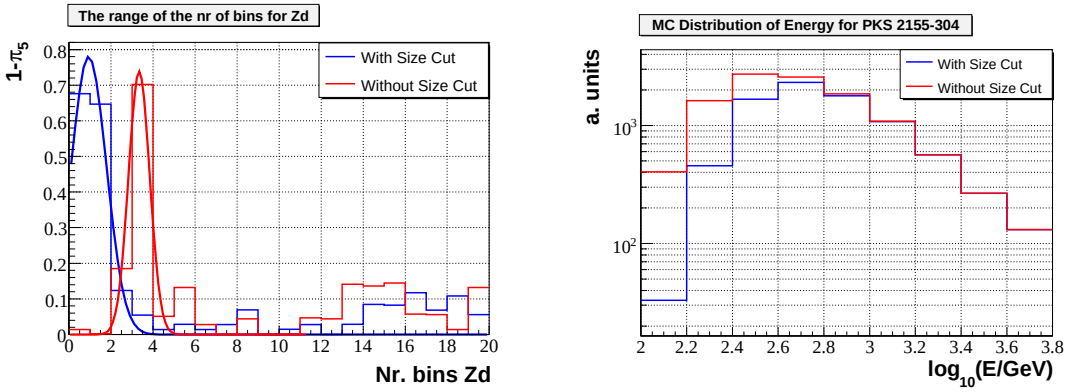

Figure 5.16: Left: The distribution of the number of bins for the zenith angle for the two different analyses, i.e. with the *Size* cut (blue) and without the *Size* cut (red). Right: The energy distribution (Monte Carlo) for the two different analyses.

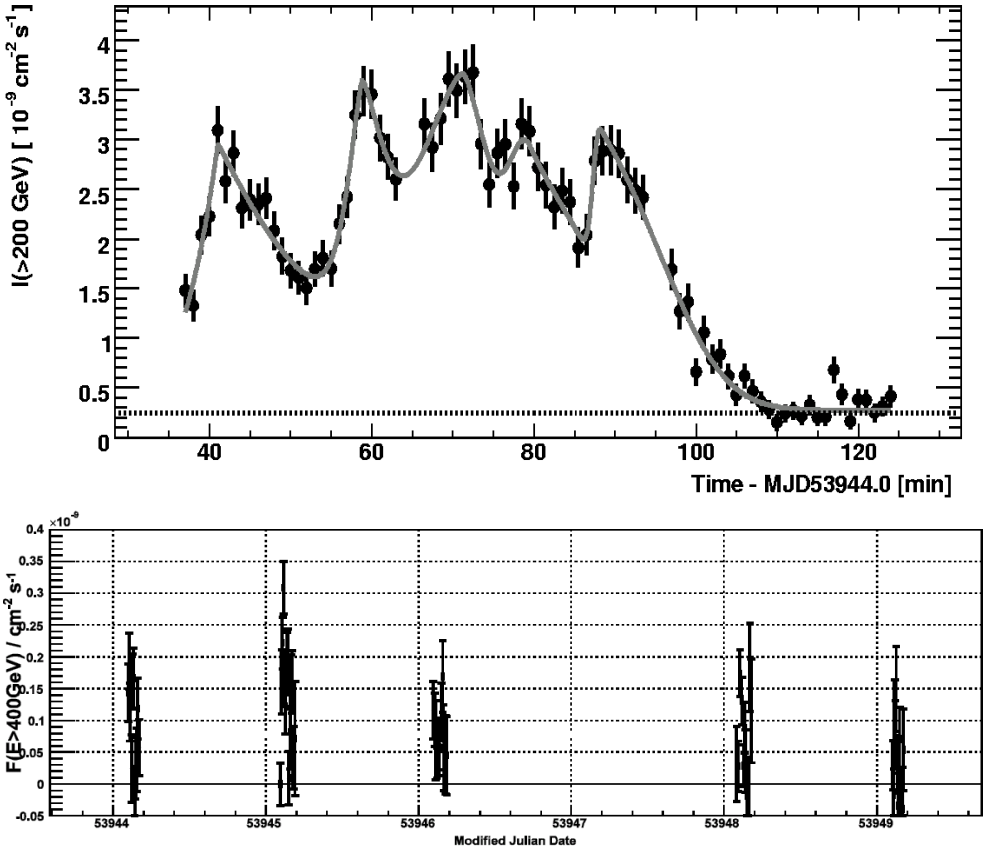

Figure 5.17: The light curve for PKS 2155-304. Top: for the data taken by H.E.S.S (Aharonian et al., 2007). Bottom: the light curve for the data taken by MAGIC (Hadasch et al., 2008).

Chapter 6

The spectral energy distribution and γ-ray absorbtion

AGN are the unique tools in the understanding of the universe. The huge distance at which they can be found makes them the youngest observable barionic structure in the universe and reveals a picture of the universe as a child. AGN give us a first hint on how galaxies are evolving and how they were initially formed. The great energy at which photons can be stimulated, exceeds by far the energies which can be produced at the present moment on Earth, therefore, the understanding of a process which produces such high energies is exciting and an unique opportunity for new physical phenomena.

From all AGN, only blazars reach such high energies, due to Doppler boosting, this is the reason why the spectral energy distribution (SED) of blazars includes the entire range of energy from all possible AGN. To understand AGN one has to understand which mechanism produces such SEDs of the observed blazars. As indicated in section 3.4.2, the jet is populated by electrons, positrons, protons and other hadronic components. Depending on which part of the population of the jet is accelerated, two types of models can be formulated: *leptonic* models, when only electrons are accelerated, and *hadronic* models, when the energies and magnetic fields are high enough such that pion production due to proton-photon interaction is possible. The differences between the two types of models occur only in the second peak (high energies) and in both of them, the first peak originates in a synchrotron spectrum. The flux, at a given observed frequency ν_0 is given by (Rybicki and Lightman, 1985)

$$F_{\nu_0} = \frac{\pi R^2 \epsilon_\nu(\nu)}{d_L^2 \kappa_\nu(\nu)} \left\{ 1 - \frac{2}{\tau_\nu^2}[1 - e^{-t_\nu}(t_\nu + 1)] \right\} \delta^3 (1+z), \tag{6.1}$$

where R is the radius of the source, d_L is the luminosity distance, ϵ_ν and κ_ν are the emission and the absorbtion coefficients. The observed frequency is related to the emitted frequency through $\nu = \nu_0[(1+z)/\delta]$, with δ the Doppler factor and z the redshift.

Moreover, it is generally assumed for both types of models, that the velocity of the bulk is constant – although acceleration (Bednarek and Wagner, 2008) or deceleration (Ghisellini et al., 2005) are used in favor of obtaining very rapid variability during the flares or for delays at different energies (like for Mrk 501, see Fig. 5.11).

6.1 Leptonic models

In the leptonic models, the second peak originates in the inverse Compton scattering of the ultrarelativistic electrons which produce the synchrotron emission at lower energies. Depending on the target photon fields, one has synchrotron photons produced inside the jet in which case the model is called synchrotron self-Compton (SSC), or external photons, called external Compton (EC).

6.1.1 SSC model

In this case the incident photons are emitted via synchrotron radiation by the same population of electrons that participate in the scattering.

To calculate the flux, one starts from a power-law distribution of relativistic electrons $N(\gamma mc^2) = N_0(\gamma mc^2)^{-p}$ $(\gamma_1 < \gamma < \gamma_2)$, which induces a spectral luminosity (Bloom and Marscher, 1996)

$$L_\nu = \pi\sigma_T R^3 N_0 (mc^2)^{1-p} 2^p v_c^{(1-p)/2} \cdot \int d\nu \nu^{(p-3)/2} I_{nu} \cdot \int_{q_1}^{q_2} f(g,s) dq, \tag{6.2}$$

where σ_T is the Thomson cross section, ν_c the critical frequency,

$$q := \frac{\nu_c}{4\nu\gamma^2(1 - h\nu_c/\gamma mc^2)}; \quad s := \left(\frac{h}{mc^2}\right)^2 \nu\nu_c, \tag{6.3}$$

and

$$f(q,s) = \frac{q^{(p-1)/2}[q\ln q + 1 + q - 2q^2 + 2sq(1-q)]}{\{1 + [sq/(1+sq)]^{1/2}\}^{p+2}(1+sq)^{(p+3)/2}}. \tag{6.4}$$

The flux can be derived after dividing with $4\pi d_l^2$ and correcting for relativistic bulk motion. For the first order self-Compton it follows the proportionality (Bloom and Marscher, 1996)

$$F_\nu^{1C} \propto N_0 R F_\nu^S \ln\left(\frac{\nu_2}{\nu_m}\right) \propto N_0^2 B^{1+\alpha} R^4 d_l^{-2} \ln\left(\frac{\nu_2}{\nu_m}\right), \tag{6.5}$$

where $F_\nu^S \propto \nu^{-\alpha}$ is the synchrotron spectrum, $\nu_2 = 2.8 \times 10^6 B\gamma_2^2$ Hz is the upper cutoff frequency, B the magnetic field and ν_m is the turnover frequency at which the source becomes opaque to synchrotron self-absorbtion. By analogy the second-order self-Compton flux can be defined as

$$F_\nu^{2C} \propto N_0 R F_\nu^{1C} \propto N_0^3 B^{1+\alpha} R^5 d_l^{-2} \ln\left(\frac{\nu_2}{\nu_m}\right). \tag{6.6}$$

Thus, the parameter space for the model consists of N_0, the magnetic field B, the Doppler factor δ, the source size, the cutoffs γ_1 and γ_2 of the electron energy distribution and electron spectral index and the distance from the BH where the acceleration takes place. Only some of these parameters can be estimated by observation, whereas the others have to be fitted or deduced theoretically.

A way to determine the magnetic field is due to the time delays between light curves at different frequencies (dominated by synchrotron emission). Then the magnetic field can be expressed, in units of G, as

$$B = \frac{2}{5}\sqrt[3]{\frac{\left(E_{\text{sy, low}}^{1/2} - E_{\text{sy, high}}^{1/2}\right)^2}{D_1(1+k)^2(\Delta t_h^{obs})^2}}, \tag{6.7}$$

where $k = u_e/u_B$ is the ratio of electron energy density in the photon field (co-moving frame) and magnetic density and Δt_h^{obs} is the observed time delay in hours.

After deciding where the acceleration of the electrons takes place, the important parameters of the models remain the Doppler factor and the electron energy density. However, a change in the value of the magnetic field implies that both, synchrotron and scattered flux density, will decrease with the same factor. Moreover, the upper cutoff depends on the first- and second-order SSC and on the magnetic field too, $\nu_2^{1C} \propto \gamma_2^4 B$. Therefore, an increase in the magnetic field results in a higher synchrotron cutoff frequency and thus a higher flux density for all frequencies between the original cutoff and the new one.

6.1.2 EC models

In this case the source of seed photons for the Comptonization is external to the jet. Two possible sources for these photons can be considered: from the central accretion disc or from a cloud. In both cases the external radiation needs to dominate the SSC emission. For this, the energy density of the external radiation (measured in the frame co-moving with the jet) must exceed the energy density of synchrotron radiation produced in the jet.

To avoid absorbtion of γ-rays by pair production on soft photons, the observed γ-rays must be produced in regions of the jet at distances bigger then 10^{17} cm, which is far from the source of radiation (Dermer and Schlickeiser, 1994). In the case that the source of the external radiation is from the accretion disc, the condition that the external radiation dominates the synchrotron radiation in the jet can be fulfilled only if the magnetic field is weak. This is a strong condition on the model. The model is not compatible with the hadronic models which need high values for the intensity of the magnetic field.

It is not unusual to suppose that the source of the external radiation is a cloud nearby the nuclei. The cloud can be the final product of the scattering of a hot accretion disc wind. The velocity vector of the material emitted lies anywhere within an angle $\theta_{\rm obs} \sim 1/\Gamma$ of the observers line of sight. This is because the Doppler factor δ has a nearly constant maximum value of $\sim \Gamma$ over this region and decreases fast outside the cone. Additionally, it is assumed that the cloud moves with the jet, and that both γ production (at low and high energies) originates in the same region of the flow[1], called *one-zone*. Such a picture is shown in Fig. 6.1.

Then the radiation energy density in the co-moving frame is (Sikora et al., 1994)

$$u'_{\rm rad} \approx \frac{L}{4\pi c^3 (\Delta t)^2 \Gamma^6} \frac{\phi_p^3}{\eta^2 \beta_p'^2}, \tag{6.8}$$

where L is the luminosity, Δt the characteristic timescale, ϕ_p represents the increase in apparent variability timescale, β'_p is the bulk speed in the co-moving frame and $\eta \leq 1$. The cooling condition can be written as

$$\frac{\gamma}{\dot{\gamma}} \sim \frac{m_e c}{\gamma_b \sigma_T u'_{\rm rad}}, \tag{6.9}$$

where γ_b is the value for the spectral break. The ratio between SSC losses and external radiation field losses is given by $u'_{\rm syn}/u'_{\rm diff}$, where the co-moving synchrotron energy density $u'_{\rm syn}$, is estimated by substituting the synchrotron luminosity $L_{\rm syn}$ in (7). If the ratio has an upper bound value $\zeta < 1$, then the condition for the Lorentz bulk factor is

$$\Gamma^6 \gtrsim \frac{\sigma_T}{4\pi m_e c^4} \frac{L_{\rm syn}}{\zeta \Delta t} \left(\frac{E_b}{E_{\rm est}} \right)^{1/2} \frac{\phi_p^2}{\eta \beta_p'^2}. \tag{6.10}$$

[1]Other models assume that the two energy range are from different location in the jet, and are called *two-zone* models (Blandford and Payne, 1981).

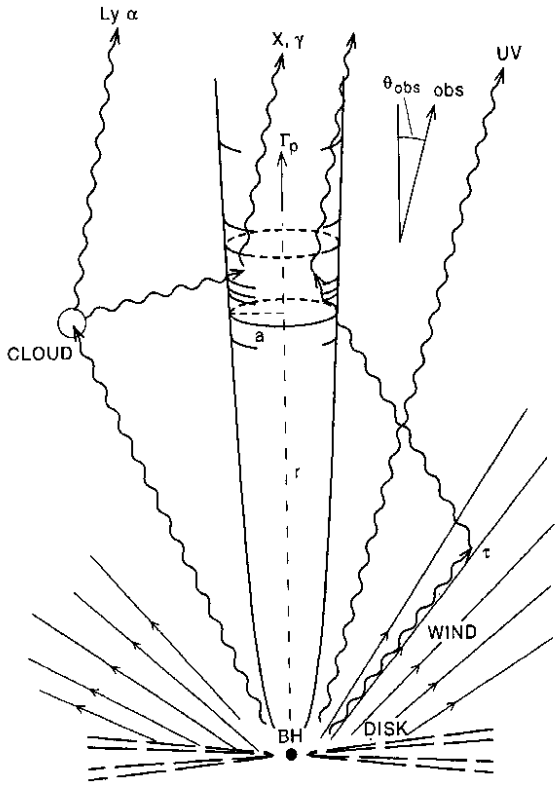

Figure 6.1: The scheme of the EC model. The radiation region, denoted by a short cylinder of dimension a moves along the jet with pattern Lorentz factor Γ_p. Underlying flow moves with Lorentz factor Γ, which can differ from Γ_p (Sikora et al., 1994).

To compute the luminosity function, the ratio between the electron energy and magnetic energy is needed

$$\frac{u'_e}{u'_B} \sim \frac{2\sigma_T(1+\ln\gamma_b)}{\pi m_e c^4 \Delta t \Gamma^6}\left(\frac{E_b}{E_{\rm est}}\right)^{1/2}\frac{(\partial L_\gamma/\partial E)^2}{\partial L_{\rm syn}/\partial E}\frac{\phi_p^2}{\eta|\beta'_p|^3}. \tag{6.11}$$

6.1.3 The modelling

At present, no overall model exists for all the blazars, since all the spectra are assumed to be power-law which is only an approximation. To be able to use the previous described models, one needs multiwavelength observations, which enable the determination of some parameters of the models within reasonable accuracy. By fitting the rest of the parameters, one tries to explain the SED for every source individually. In the last decade, the models could reproduce very well the SED of several blazars and appear to converge more and more to a consistent picture (Ghisellini et al., 1998).

It is possible to identify the following sequence HBL → LBL → FSRQ which implies an increase of the external Compton contribution to the γ-ray spectrum. Thus, most of the FSRQ are modeled with EC models (Dermer et al. 1997; Sambruna et al. 1997; Mukherjee et al. 1999; Hartman et al. 2001), whereas HBL could be explained only with SSC models (Mastichiadis and Kirk 1997; Pian

et al. 1998; Petry et al. 2000; Krawczynski et al. 2002). The LBL needs EC models as well if one uses the EGRET data (Sambruna et al. 1999; Madejski et al. 1999; Böttcher and Dermer 2002).

It was generally noticed that the HBL requires higher average electron energies and lower magnetic fields than LBL and FSRQ. Moreover, the decreasing relevance of external contributions to the radiation field in the FSRQ → LBL → HBL sequence can be an indication of an evolutionary state of the blazars, which can easily be seen from the EC model presented above where the cloud moves with the jet. If the rate of formed bulks in the jet is higher than that of the clouds, then the EC model transforms into a SSC model and vice-versa. This difference in the formation rate is related to the gradual depletion of a finite available circumnuclear material (Cavaliere and D'Elia, 2002).

6.2 Hadronic models

The fitting of a leptonic model to the multiwavelength data is not always possible. Moreover, an "orphan" flare for 1ES 1959+650 was observed (Krawczynski et al., 2004), i.e. an increase of the flux in the TeV range with not change in the X-ray regime. There are two possible ways of explaining such an observation: using leptonic models or using hadronic models. When using leptonic models, it must be assumed that the synchrotron spectrum and the Comptonization spectrum originate in different zones of the jet, such that the two-zone models are needed.

The main idea of hadron models is to add to the existing population of electrons and positrons a population of accelerated protons, which will cool in the synchrotron photon field induced by the accelerated electrons. Although the cross-section of the proton-photon interaction is of three orders of magnitude smaller than the Thomson cross-section, the cooling time for protons can be as short as the one for electrons (Mannheim, 1996). The ratio of electron and proton cooling time scale is given by

$$\frac{t_p}{t_e} \simeq \frac{n_\gamma(\epsilon)\frac{\epsilon}{m_e c^2}\gamma_e \sigma_T c}{n_\gamma \frac{m_\pi c^2}{\gamma_p} \cdot \frac{m_\pi}{m_p}\sigma_{p\gamma} c} = \frac{m_p}{m_e}\frac{\gamma_e}{\gamma_p}\frac{\sigma_T}{\sigma_{p\gamma}} \approx 2.5 \cdot 10^6 \frac{\gamma_e}{\gamma_p}, \tag{6.12}$$

where $n_\gamma(\epsilon) \propto \epsilon^{-1}$. The ratio of electron induced luminosity and proton induced luminosity is related to the cooling time as

$$\frac{L_p}{L_e} \approx \frac{u_p}{u_e}\frac{t_e}{t_p}, \tag{6.13}$$

with u_e and u_p the electron and the proton energy density. It can be remarked that the proton luminosity can exceed the electron induced luminosity with a large value. The cutoff usually follows at energies for which the acceleration time scale equals the expansion time scale.

The proton interaction with photons will produce pions, which decay in secondary electrons and positrons, γ-rays and neutrinos as described

$$\pi^0 \to \gamma + \gamma, \quad \pi^\pm \to \mu^\pm + \nu_\mu \to e^\pm + 2\nu_\mu + \nu_e. \tag{6.14}$$

It produces also neutrons with the same probability with which positive charged pions are produced, through the interaction $p + \gamma \to p + \pi^0$. The very high energy of the initial accelerated proton, i.e. more then 10^9 GeV, allows the neutron to escape and contribute to the overall cosmic-ray spectrum, through β-decay. The photons from pion decay are completely reprocessed by a synchrotron cascade until the energy of the process drops below TeV. The cascade is initiated due to the flat spectrum of the pion flux, which means that the maximal injection power is at the maximal pion energy (Mannheim, 1991).

In the case of proton-proton (pp) interaction the cooling time is constant and the emissivity of the secondary outcomes follows the power-law of the protons, which is much steeper than the pγ

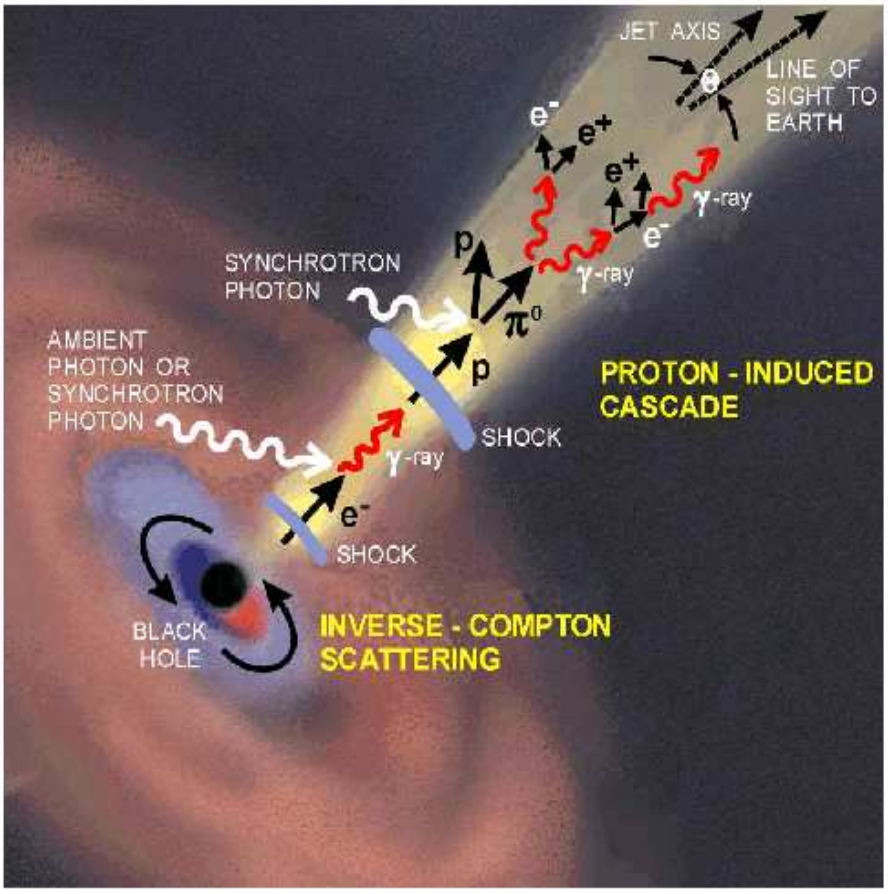

Figure 6.2: The hadron model (Buckley, 1998)

cooling. This property is important for the neutrino flux from proton blazars which is flat for pγ interaction, but is E^{-1} for pp interaction, being thus related to low energy neutrinos. To determine the ratio of the two luminosity, pγ and pp, one needs the energy loss time scale for pp interaction given by $t_{pp} = (n_{th} \cdot c \cdot \sigma_{pp})^{-1}$, with $\sigma_{pp} \simeq 3 \cdot 10^{-26}$ cm^2 and $n_{th} \leq 7.9 \cdot 10^2 \cdot M_8 \cdot r^{-2}$ cm^{-3}, where r is the length of the jet, and $M_8 = 10^8 \cdot M_\odot$. Then

$$\frac{L_\nu(pp)}{L_\nu(p\gamma)} = \frac{t_{p\gamma}}{t_{pp}} \leq 7 \left[\frac{r_S}{r}\right], \tag{6.15}$$

where r_S is the Schwarzschild radius ($r_S = 10^{-5} \cdot M_8$). The ratio implies that even at the base of the jet ($r \approx 10 r_S$) photon cooling is the dominating source of secondaries. However, while the electrons are continuing to cool even at greater distances from the accelerating region, generating extended emission region like the radio lobs, protons don't show such a behavior.

To calculate the spectrum, it is important to know the proper value of the proton/electron ratio, see equation (12). Then the spectrum can be expressed, in units of 10^{12} Hz Jy, as

$$[\nu S_\nu]_{12} = 0.03 k_e \ln \frac{r_{\min}}{r_{\max}} \left(1 + \frac{2}{3} k_e \Lambda_e\right)^{-1} \gamma_j^{-1} D_j^3 L_{44} d_L^{-2}, \tag{6.16}$$

where k_e and Λ_e are constants (see Mannheim (1993) for more detail), γ_j the Lorentz boost of the

bulk in the jet, D_j the Doppler factor of the jet, L_44 the luminosity of the jet in units of 10^{44} erg/s and d_L the luminosity distance in Gpc. The cascade spectrum of the induced proton luminosity depends also on the radiation components and the intensity of the magnetic field.

Since the flare of leptonic models (one-zone) correlate with the increase in the X-ray and TeV range, the hadronic models can explain an increase only in the TeV regime by π^0 decay in γ-rays as the result of the pγ interaction.

6.3 Absorbtion

Although the present models for AGN do not offer an overall explanation, they open a window for the physical phenomena that generate the VHE photons. However, not all the VHE photons from the blazars are reaching Earth due to their interaction with low energy photons, a process called absorbtion. This diminishes the initial number of emitted photons and therefore the observed spectra at VHE energies of the blazars differ from the true (emitted) ones. To be able to understand correctly the phenomenon that creates the VHE photons it is necessary to correct the measured VHE spectrum, i.e. to reabsorb.

The effect of absorbtion reveals another important aspect of the AGN structure. Due to the VHE of the emitted photons, the interaction with the low energetic photons takes place at the scale of $\sim$ Mpc from which an e^+e^- pair is created. At this distance, the pair is in the intergalactic medium with a very small magnetic field $\sim 10^{-11}$ G, but with a big uncertainty. Thus, depending on the intensity of the magnetic field, the emitted photons from the e^+e^- pair will be deflected insignificantly being observable on Earth, or it will be so much deflected that it will not reach Earth anymore. In the latter case, the photons will create a halo around the blazar.

6.3.1 Observation and modelling

There are several sources of the low energy photons which can interact with the VHE photons. The most important contributions are

- *Galaxy cluster.* Although not detected with EGRET, Scharf and Mukherjee (2002) have shown that ~ 450 of the richest clusters with a bolometric luminosity of $\approx 10^{44}$ erg s^{-1} can explain between 1% and 10% of the gamma-ray background.
- *AGN.* It is still not clear how much the AGN contribute to the MRF. Stecker and Salamon (1996) used a radio luminosity function and a linear correlation between radio and gamma-ray luminosity in order to measure the contribution of the blazars to MRF. With the flaring components of the blazars they could explain all the observed background flux, but they overproduced the number of low redshifted sources detected by EGRET. Other calculations (Chiang and Mukherjee, 1998) obtained only 25% to 50% of the observed background flux, whereas (Mücke and Pohl, 2000) obtained 40%-80% by the use of multiwavelength spectra. X-ray BL Lac contributes with maximum 10% (Kneiske and Mannheim, 2008) to MRF, and FRI galaxies with only 1% (Stawarz et al., 2006).
- *Star forming galaxies.* Using a power-law fit of the galactic spectrum of Milky-Way with a spectral break at 850 MeV, a total gas mass of 10^{10} M$_\odot$ with a gas density of 1 cm^{-3} and a star formation of 3.2 M$_\odot$ yr^{-1} (Pavlidou and Fields, 2002) could obtain a Milky-Way-like spectrum.

After integrating the luminosity with the cosmic star formation rate up to $z = 5$, they obtained a flux of $2{\times}10^{-7}$ GeV cm^{-2} s^{-1} sr^{-1} or $6{\times}10^{-7}$ GeV cm^{-2} s^{-1} sr^{-1} for star formation without and with dust corrections. This represents $\sim 20\%$ of the observed background flux.

- *Interstellar medium.* The most significant ingredients are gas and dust. In our galaxy, it is known that they coexist at different temperature regimes depending on the distance to the energy source. Hot dust, in spiral galaxies, has temperatures varying from 50K–200K (Sauvage et al., 1997). The origin of the energy that heats the dust are young massive stars or accretion sources. The radiation from this dust contributes to the mid-infrared and reprocesses only a small ratio of the emitted luminosity. Worm dust, with temperatures between 25K and 50K, is heated by the mean interstellar radiation field. Dust inside molecular clouds is protected by the radiation and can have temperatures between 10K and 25K. Very cold dust at temperatures of 10K or bellow can be present as well, but it is difficult to detect it (sub-mm observation were not conclusive), thus it is not used in modelling.

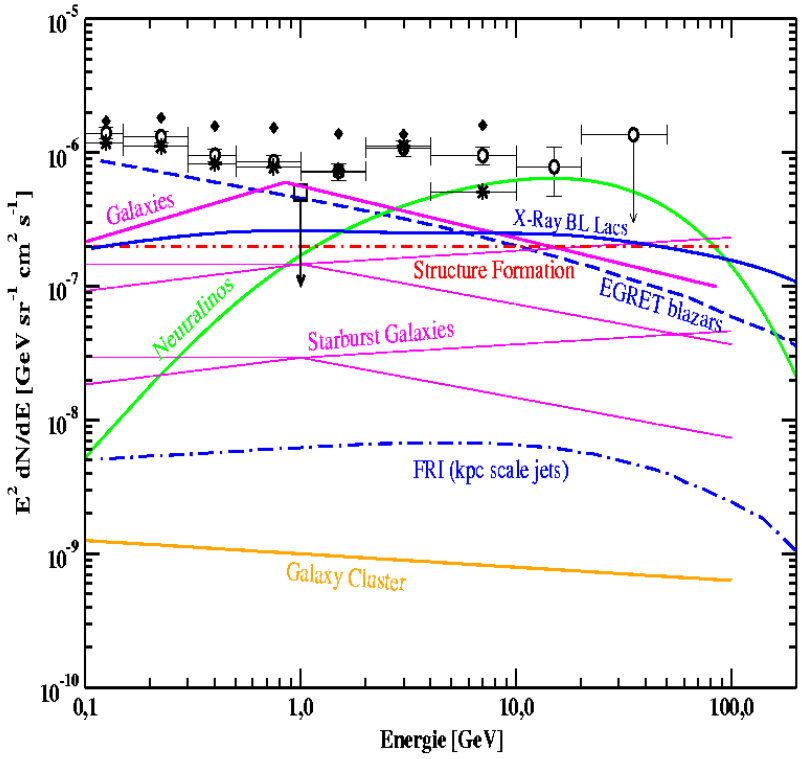

Figure 6.3: Different contributions to the Gamma-ray background (Kneiske, 2007).

All of them form the metagalactic radiation field (MRF), which today ($z = 0$) is seen as the extragalactic background light (EBL) as shown in Fig. 6.3. The modelling of the MRF is not an easy task since many of the contributing parts are very poorly known, as already emphasized. The most important ingredients of the model are

- *Galaxy model.* Because no appropriate model exists, the galaxies are be approximated with an initial mass fraction which decays in a stellar distribution. Because the massive stars have

a short life time (10^7 yrs) they will produce predominantly UV light, while the less massive stars have a longer life time and produce the bulk of the "red light". Therefore the SED of the galaxy depends highly on time.

- *Interstellar medium.* The three regions of dust are modeled by means of black body spectra

$$L^d_\lambda(L_{bol}) = Q_\lambda \cdot \sum_{i=1}^{3} c_i(L_{bol}) \cdot B_\lambda(T_i), \tag{6.17}$$

with $Q_\lambda \propto \lambda^{-1}$, and $L_{bol} = L_{bol}(\tau)$. All six parameters are obtained by fitting the data.

- *Stellar formation history.* Similar to the interstellar medium, it is possible to fit the data with a power law

$$\dot{\rho}(z) \propto (1+z)^\alpha \tag{6.18}$$

with $\alpha = \alpha_m > 0$ for $z \leq z_{peak}$ and $\alpha = \beta_m < 0$ for $z \geq z_{peak}$. The data obtained from the deep galaxy surveys (Kennicutt, 1999) or from Lyman α absorbed studies Pei et al. (1999), indicate a peak in the star formation rate around $z_{peak} \approx 1.1$.

- *Metallicity.* Represents the abundance of chemical elements in the stars. No model exists, thus average values $Z_\odot$ are used between 0.0001 and 0.02.

- *Optical depth.* The optical depth for pair creation for a source at redshift z_o with an observed energy E_γ, is given by

$$\tau_{\gamma\gamma}(E_\gamma, z_o) = c \int_0^{z_o} \int_0^{2} \int_{\epsilon_{gr}}^{\infty} \frac{dl}{dz'} \frac{\mu}{2} \cdot n(z', \epsilon) \cdot \sigma_{\gamma\gamma}(E_\gamma, \epsilon, \mu, z') d\epsilon d\mu dz', \tag{6.19}$$

with $\frac{dl}{dz'}$ the cosmological line element, $\mu = \cos\theta$ where θ is the incident angle between the interacting photons, $n(z', \epsilon)$ the number density of MRF as function of redshift and the MRF photons energy and $\sigma_{\gamma\gamma}$ the pair-production cross section. The effect of optical depth is strong only at low redshift (< 0.2), above, the MRF appears to be rather insensitive to it. The observed spectra are modified by γ-ray attenuation through the equation

$$F_{obs}(E) = F_{int}(E) \cdot \exp[-\tau_{\gamma\gamma}(E, z)], \tag{6.20}$$

where F_{obs} and F_{int} are the observed and intrinsic fluxes.

In order to calculate the MRF, one begins with the distribution of the galaxies models which gives the co-moving emissivity (luminosity density) at the redshift z through the convolution integral

$$\mathcal{E}_\nu(z) = \int_z^{z_m} L_\nu(t(z) - t(z'))\dot{\rho}(z') \left| \frac{dt'}{dz'} \right| dz', \tag{6.21}$$

where z_m represents the redshift at which the star formation has began. Integrating the emissivity over redshift yields the energy density. If the energy density is multiplied with $\frac{c}{4\pi}$, one obtains the co-moving power spectrum for the MRF

$$P_\nu(z) = \nu I_\nu(z) = \nu \frac{c}{4\pi} \int_z^{z_m} \mathcal{E}_{\nu'}(z') \left| \frac{dt'}{dz'} \right| dz' \tag{6.22}$$

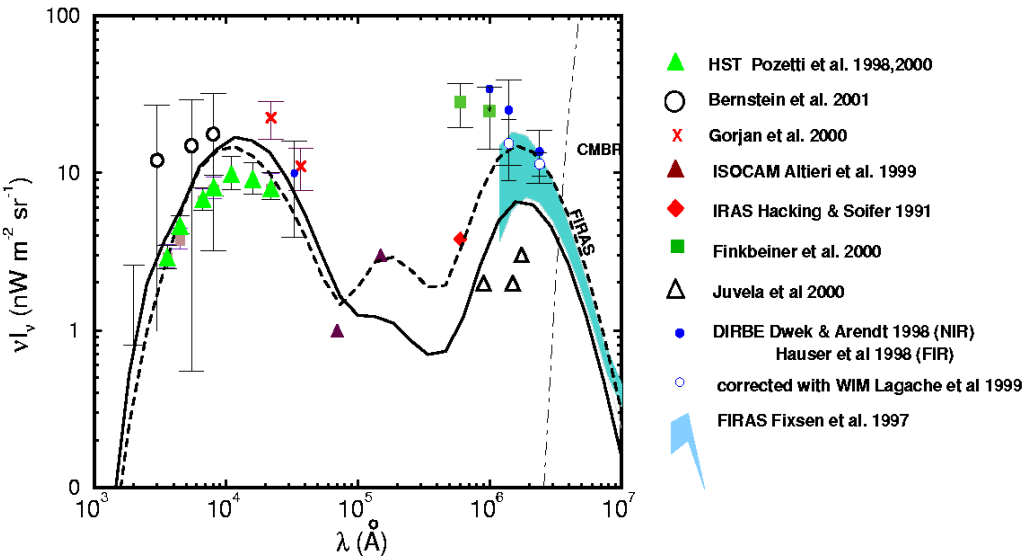

Figure 6.4: The EBL computed with the model (solid line). A metallicity of $Z = 0.02$ and E(B-V)=0.14 for young star population, and E(B-V)=0.03 for an old star population. The deficit at lower wavelengths can be avoided only for very low metallicity $Z = 0.0001$ (Kneiske et al., 2002).

where $\nu'(1+z) = \nu(1+z')$. For the derivative of time with respect to redshift one has (see Weinberg (1972))

$$\left|\frac{dt}{dz}\right| = \frac{1}{H_0(1+z)\sqrt{\Omega_r(1+z)^4 + \Omega(1+z)^3 + \Omega_R(1+z)^2 + \Omega_\Lambda}}, \tag{6.23}$$

where $\Omega_r, \Omega, \Omega_R$ and Ω_Λ are the density parameters for relativistic, radiation, matter and cosmological. The result of the model is shown in Fig. 6.4 together with data obtained at different wavelengths.

6.3.2 The re-absorbed spectrum

The parameters for the MRF generally used to fit the data at redshift $z = 0$ are: the peak redshift for the star formation rate together with the two indexes α_m and β_m, the star formation rate at the peak redshift (see equation (6.18)), the coefficient for warm dust c_e and the fraction of ionized photons that escape from a galaxy. Different fits will give different models for the absorbtion. The model which best interpolates the actual MRF data is called *Best-fit model*[2]. For the re-absorb the spectra obtained in chapter 5, the Best-fit model was used.

The result of the re-absorbtion for Mrk 421 is shown in Fig.6.5. The blue points represent the observed spectrum, whereas the red ones show the spectrum after the re-absorbtion. The blue and red curve are the fits corresponding to observed and reabsorbed spectra. To emphasize the range of the re-absorbed spectrum with respect to the SED, on the right side of Fig.6.5, the spectrum is shown after being multiplied with E^2. The small redshift for Mrk421 implies that the observed

[2]For the individual values for each model see (Kneiske et al., 2004).

spectrum needs only a minor correction. The values of the parameterized spectral indexes become $a = 2.25 \pm 0.11$ and $b = 0.17 \pm 0.08$. Then the peak for the energy is reached at 117± 61 GeV.

Also Mrk 501 minor corrections appear as ca be seen in Fig.6.6. For both observation nights the peaks of the energy were already seen in the measured spectra. Through the re-absorbtion the flux peaks move towards higher energies and increase in values. For the night of the 30-th of June the flux peak changes from 430 GeV to 800 ± 93 GeV having a value of $(2.16 \pm 0.19_{\text{stat}}) \times 10^{-6}$ m^{-2} s^{-1} TeV^{-1}. Same shift is observed also for the night of the 9-th of July from, as the flux peak moves from 250 GeV to 490 ± 78 GeV, with a value of $(1.70 \pm 0.21_{\text{stat}}) \times 10^{-6}$ m^{-2} s^{-1} TeV^{-1}. independently of the observed variations from the two nights of Mrk 501, it can be noticed that the IC-peak is nearly one order of magnitude higher than the one of Mrk 421.

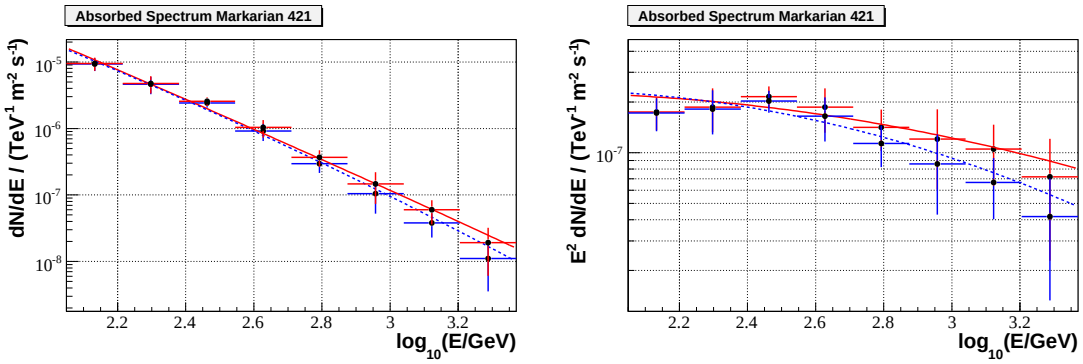

Figure 6.5: The absorbed spectrum for Mrk 421. On the left side the observed spectrum in blue and the re-absorbed spectrum in red. The blue and red curve are the fits for the individual spectra. On the right side the spectra are plotted after being multiplied with E^2.

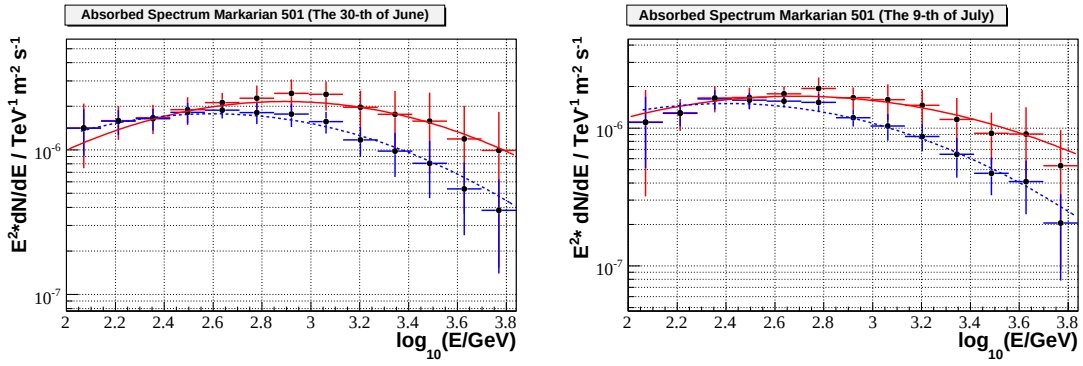

Figure 6.6: The absorbed spectrum for Mrk 501 for the night of the 30-th of June (left) and the night of the 9-th of July (right). The blue/red points and curves represent the measured/re-absorbed spectra and fits.

In contrast to both Markarian, PKS 2155-304 does not show a curved spectrum in none of the two cases, i.e. measured, respective re-absorbed spectrum as shown in Fig. 6.7. This indicates that the peak must be at energies below 100 GeV, since the spectrum is compatible with a power-law only at some distance from the peak. The fact that the re-absorbed spectrum could be fitted by a pure power-law (with the slope of -2.59 ± 0.2), an important conclusion can be drawn: the observed broken spectrum is due to a local effect from the emitter to the observer. The same broken spectrum

was observed by Aharonian et al. (2007), so can be concluded that it is not an effect of the very high zenith angle observation with the MAGIC telescope, or an effect of the zenith angel in general, the cause still remains unknown.

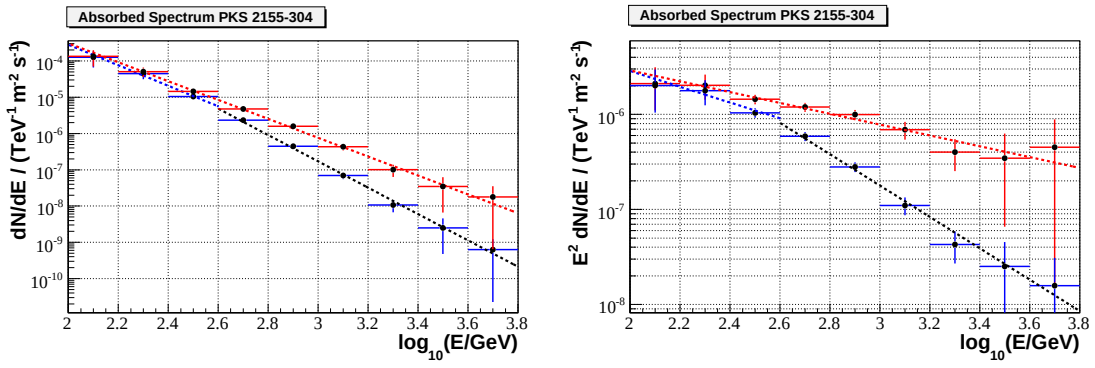

Figure 6.7: The absorbed spectrum for PKS 2155-304. The blue points together with the blue and black lines represent the measured spectrum, whereas the red points and curve the re-absorbed spectrum.

6.3.3 How small is the observable universe at very high energies?

For all the re-absorbed spectra presented above, it was possible to fit an SSC or EC model. But as the redshift increases, it becomes more difficult to find a fit for the re-absorbed spectra and data taken simultaneously at different frequencies. The reason is that the re-absorbtion is responsible for a shrinking of the observable universe as the energy of the photon increases. When a photon with VHE interacts with a low energy photon, it cannot be observed anymore as in the interaction ane^+e^- pair is produced. As the energy of the photon increases, increases also the probability to interact with a low energy photon. The spectrum of the low energy photon (from stars, galaxies, etc.) evolves in time and depends on the redshift as already emphasized, thus, the higher the redshift of the VHE source, the lower the probability to observe it. As a conclusion, the observable universe decreases as the energy of the photon increases, as the left side of Fig. 6.8 shows. The gray area represents the zone where observation of VHE photons is strongly suppressed, i.e. with optical depths $\tau > 1$. The dotted line represents the sensitivity of the MAGIC telescope and emphasizes how far VHE sources can still be detected.

One can easily remark from Fig. 6.8 that for $\tau = 1$ at 1 TeV the gamma-sky shrinks around $z = 0.13$ and drops below $z = 0.1$ for 5 TeV. For PKS 2155-304 the range of the observed spectrum extends up to 5 TeV although the source is at a redshift of z=0.117. Moreover, the newly discovered 3c279 at z=0.536 extends up to $\sim$ 500 GeV (Albert et al., 2008b), being in the gray range for $\tau = 1$. The spectrum of 3c279 is shown on the right side of Fig. 6.8 with the black points as the measured spectrum and the red and blue ones for different re-absorbed spectra. Both re-absorbed spectra show an increase at higher energy, due to the optical depth. Although one should observe less than measured, the re-absorbed spectra increase due to the strong suppression of the $\gamma\gamma$ interaction. Such a phenomenon is called the *TeV crisis*.

One way out of this crisis is to suppose that the predicted models are not sufficiently good, i.e. τ should be greater than 1. However, this is not so easy, as all the present models are based on extensive observations for all classes of low energy photons (§6.3.1). Another way to overcome the TeV crisis is to assume that the unfolding methods are not sufficiently developed, since they

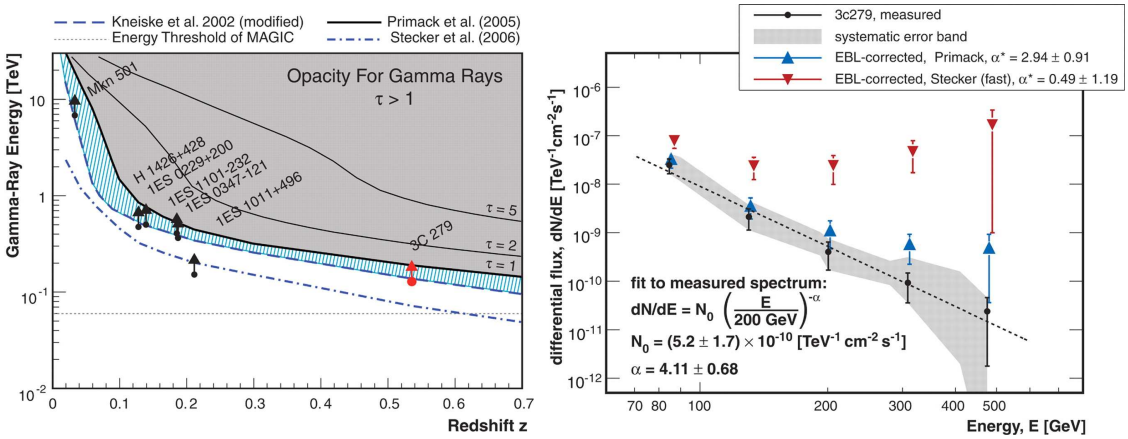

Figure 6.8: Left: the gamma-ray horizon. The prediction range of the EBL models is illustrated by the thick solid black line and the dashed-dotted blue line. The gray area indicates an optical depth with $\tau > 1$, i.e. where the suppression of the flux becomes stronger. Right: the spectrum of 3C 279 (black points) and two different re-absorbtions of the spectrum (blue and red points) (Albert et al., 2008b).

overestimate the energy distribution at higher energies. The new unfolding method described in chapter 4 enforces the answer of the established unfolding methods to the TeV crisis. Since the unfolding methods are based on different principles, the probability that a mistake is hidden in the methods, decreases.

Other solutions of the TeV crisis were proposed. Harwit et al. (1999) considered the high energy events as the superposition of two or more low energy photons which arrive simultaneously on the top of the atmosphere. However, such an idea turned out to be unlikely although not completely ruled out (Protheroe and Meyer, 2000). Another possibility is to invoke Lorentz invariance (Coleman and Glashow, 1999), which can reduce the re-absorbed spectrum, but the reduction is not sufficient, reason why the Lorenz invariance is only a component of the whole mechanism. A more recent possibility was advocated by Aharonian et al. (2008) where hard spectra can be obtained as a result of internal $\gamma\gamma$ interaction. This is possible if the internal absorbtion of gamma-rays caused by interactions with dense narrow-band radiation fields in the vicinity of compact gamma-rays production regions. Such mechanism needs large values for the Doppler factor (> 30) and predicts detectable synchrotron radiation of secondary e^-e^+ pairs. Such detection will be meaningful only by a revision of the present theoretical developments and has, additionally, a high Background due to the magnetic field.

Chapter 7

Conclusion

The present thesis proposes a new unfolding method for the MAGIC telescope, named *probability unfolding method*. Results obtained using this method were compared with the results obtained by already established unfolding methods, being a strong proof that the new unfolding method is reliable and it offers another point of view for the spectra reconstruction. For a better functioning of the unfolding method an optimization algorithm was conceived and implemented. With the same scope, two new indicators (ρ_V and π) for the parameter space of the unfolding solution, were introduced. In what follows, an overview of the most important results of this thesis is presented.

1. In order to adapt the unfolding method to the requirements of the MAGIC telescope, a large number of parameters were tested preserving only the most important ones: $Size$, $Dist$ and zenith angle (Zd). For a correct subtraction of the Background from the Data, the global weight value for the Background is needed. An additional method to compute the global weight for the Background was developed, based on its correlation with the zenith angle.

2. The parameter space of the unfolding method is very large, so finding a solution is a time consuming task. The optimization method applied to overcome this inconvenience takes advantage of the properties of the unfolding method as the function to be optimized is unknown. These properties are related to the energy limits of unfolding, more concrete one of the energy limits acts like a translation factor for a function depending on the other energy limit.

3. Since every unfolding method is independent of the data content, it is important to understand to which extent the unfolded solution represents the unfolding variables in the data after analysis cuts. The new factors (ρ_V and $\pi(\varepsilon)$) introduced in section 4.3.3 offer an approach to tackle the problem of the correlation of the unfolded solution with the data. Along the way, a wider applicability of the two factors revealed.

   (a) Small values for both factors indicate an easy and fast to find unfolding solution, whereas large values for at least one of them indicate a difficult to find unfolding solution.

   (b) The probability factor $\pi(\varepsilon)$ with $\varepsilon = 0.05$ and named π_5, is used to describe a dependency between the number of unfolded events (N_I) and excess events (N_E). The variation along the domain of any parameter used in the unfolding, of the value $1 - \pi_5$ is named π_5 *plot*. For such a plot a minimum of 100 runs for Monte Carlo and 200 runs for Data for each value in the domain (bin) are required. Choosing a lower limit ($\sim 75\%$) for the value of $1 - \pi_5$, the reduced parameter space of the unfolding results is obtained.

(c) The unfolding variables that correlate with the energy show a broad region in the π_5 plot, whereas those which do not correlate with the energy show a very narrow range. If using an additional unfolding variable to the already used ones and the domain of one of the old unfolding variables proves a broadening and an increase in the value of $1 - \pi_5$, then it is sure that the new unfolding variable is suitable for the unfolding. Thus, low values for $1 - \pi_5$ indicate missing unfolding variables, e.g. PKS 2155-304 Fig. 5.16. The effect of broadening can be very small, so that a large number of random runs are required (> 500/bin).

(d) For the same data, different analysis cuts generate different domains and different $1 - \pi_5$ values in the π_5 plot of every unfolding variable. For PKS 2155-304 two different analysis cuts applied indicate, in the case of zenith angle, a shift of the domain from 0-1, first cuts, to 3, second cuts. As a conclusion, the analyzed data after the first cuts do not include any information about the zenith angle, whereas those from the second cuts do, and explain the two different spectra obtained for PKS 2155-304, Fig. 5.15.

(e) The π_5 plot can also be used as a measure of the effect of the cuts on the analyzed data, i.e. how much the domain of an unfolding variable is shifted (see Fig. 4.5 and Fig. 4.9). In the case of very narrow domain, if the cuts shift the domain towards zero, then it is considered that the unfolding variable did not survive the cuts. Only those unfolding variables which survive the cuts are needed in the unfolding. It follows that unfolding is cut-sensitive, being an advantage for the probability unfolding method for which the unfolding variables used can be a priori fixed. In the case of the direct unfolding methods the sensitivity to cuts is a disadvantage, since the formula to estimate the energy has to be actualized after every cut.

(f) Another property of the two factors is that they can be defined independently of the unfolding result and moreover, independently of the unfolding method used. In order to define them as mentioned, the condition for a good result of the unfolding method and the restrictions of the unfolding problem are used.

The principle of the factors introduced extends the applicability of the unfolding methods towards completely different directions of investigation than initially designed.

4. The spectra obtained stressis the typical behavior of the blazars proved by other unfolding methods. In most of the cases it was even possible to extend the previous existing spectra to higher and lower energy limits (same data but not necessarily same cuts).

5. Although the spectra represent the reconstructed information of the photons, i.e. the energy distribution, it is not possible to use them for physical predictions. This is a consequence of the interaction of the VHE photons with low energy photons, which produces a suppression of the intrinsic spectra of the blazars and AGN, in general. So, for physical predictions, the obtained spectra have to be re-absorbed by means of a Best-fit-Model (Kneiske et al., 2004). For energies above a few TeV the analyzed spectra show a much smaller slope than the theoretical results suggest. So, with a completely different approach, the present unfolding method enforces the results obtained by the classical unfolding methods regarding the spectra of the blazars, which contradict the theoretical predictions. What is to be trusted, theory, which develops on solid ground or experiments as Kepler did?

Appendix A

Trajectory of charged particles

To calculate the trajectory of a charged particle in a magnetic field, one stars from the Lorentz force

$$m\gamma\frac{d\mathbf{v}}{dt} = \frac{q}{c}(\mathbf{v}\times\mathbf{B}), \tag{A.1}$$

which can be written as ($D = \frac{d}{dt}$)

$$\begin{cases} D^2v_x - B_z\frac{e}{m}Dv_y + B_y\frac{e}{m}Dv_z = 0 \\ B_z\frac{e}{m}Dv_x + D^2v_y - B_x\frac{e}{m}Dv_z = 0 \\ -B_y\frac{e}{m}Dv_x + B_x\frac{e}{m}Dv_y + D^2v_z = 0. \end{cases} \tag{A.2}$$

After some algebraical manipulation one can write for the x component

$$B'_x\frac{d^3v_x}{dt^3} + \left[\frac{d^2B'_x}{dt^2} - B'_z\frac{dB'_y}{dt} + B'_x(B_x^{'2} + B_y^{'2} + B_z^{'2})\right]\frac{dv_x}{dt} + B'_z\frac{d(B'_xB'_z)}{dt}v_x = 0, \tag{A.3}$$

with $B'_i = \frac{qB_i}{\gamma mc}$, $i = x, y, z$. In the same way one can write the equation for v_y and v_z by rotating the indices. The equation (A.3) represent the general equation for the trajectory of a charged particle (for the x component) for an arbitrary magnetic field. No analytical solution exist for (A.3), thus one assumes a homogeneous magnetic field and (A.3) becomes

$$\frac{d^3v_x}{dt^3} + (B_x^{'2} + B_y^{'2} + B_z^{'2})\frac{dv_x}{dt} = 0 \;\Leftrightarrow\; \frac{d^3v_x}{dt^3} + \left(\frac{qB}{\gamma mc}\right)^2\frac{dv_x}{dt} = 0, \tag{A.4}$$

with $B = \sqrt{B_x^2 + B_y^2 + B_z^2}$. Writing $Dv_x = \psi_x$ the right part of (A.4) yields

$$\frac{d^2\psi_x}{dt^2} + \left(\frac{qB}{\gamma mc}\right)^2\psi_x = 0. \tag{A.5}$$

The last equation implies, due to the constant coefficient, the solutions

$$\psi_{x,1} = c_0\cdot\sin\left(\frac{qB}{\gamma mc}t\right) \;\text{ and }\; \psi_{x,2} = c_0\cdot\cos\left(\frac{qB}{\gamma mc}t\right). \tag{A.6}$$

Because the coefficient of equation (A.5) is independent of the index, one obtains the same solution for the velocity independent of the index, i.e.

$$\mathbf{v}_1 = c_0\frac{\sin(\omega_B t)}{\omega_B} + c_1 \;\text{ and }\; \mathbf{v}_2 = c_0\frac{\cos(\omega_B t)}{\omega_B} + c_1, \tag{A.7}$$

with

$$\omega_B = \frac{qB}{\gamma mc}. \tag{A.8}$$

As the integration is on a single direction, the constant c_1 represents a constant velocity, whereas the parallel and perpendicular velocities ($\mathbf{v}_1$ and $\mathbf{v}_2$) are in the same plain and describe a circular motion.

Appendix B

Apparent speeds for jet components

To calculate the subluminal limit one starts from (3.38) and imposes

$$\frac{v_{app}/c}{\sin\phi + (v_{app}/c)\cos\phi} < 1 \quad \Rightarrow \quad \beta_a < \frac{\sin\phi}{1-\cos\phi}, \tag{B.1}$$

with $\beta_a = v_{app}/c$. It follows that

$$\beta_a^2 < \frac{1 - cos^2\phi}{1 - 2\cos\phi + \cos^2\phi}, \tag{B.2}$$

which is equivalent to

$$(\beta_a^2 + 1)\cos^2\phi - 2\beta_a^2\cos\phi + (\beta_a^2 - 1) < 0. \tag{B.3}$$

Solving the equation for $\cos\phi$ one finds

$$\cos\phi_{1,2} = \frac{\beta_a^2}{\beta_a^2+1} \pm \frac{1}{\beta_a^2+1} \quad \Rightarrow \quad \cos\phi_1 = 1, \;\; \cos\phi_2 = \frac{\beta_a^2-1}{\beta_a^2+1}. \tag{B.4}$$

Thus, the condition (B.1) implies

$$\frac{\beta_a^2-1}{\beta_a^2+1} < 1. \quad \square \tag{B.5}$$

For the minimum from (3.38) one gets

$$\frac{d\beta}{d\phi} = 0 \quad \Rightarrow \quad \cos\phi - \beta_a\sin\phi = 0 \quad \Rightarrow \quad \cot\phi = \beta_a = \frac{v_{app}}{c}, \tag{B.6}$$

with $\beta = v/c$. To calculate the minimal value one uses the identity

$$\sin^2\phi + \cos^2\phi = 1 \quad \overset{\text{(B.6b)}}{\Rightarrow} \quad \frac{1}{\sin^2\phi} = 1 + \beta_a^2 \quad \Rightarrow \quad \sin\phi = \sqrt{\frac{1}{1+\beta_a^2}}. \tag{B.7}$$

On the other hand from (3.38) one gets

$$\begin{aligned} \beta_{min} &\overset{\text{(B.6b)}}{=} \frac{\frac{\cos\phi}{\sin\phi}}{\sin\phi + \frac{\cos^2\phi}{\sin\phi}} \\ &= \cos\phi \\ &\overset{\text{(B.6b)}}{=} \beta_a \sin\phi \\ &\overset{\text{(B.7c)}}{=} \sqrt{\frac{\beta_a^2}{1+\beta_a^2}}. \quad \square \end{aligned} \tag{B.8}$$

Acknowledgements

During the PhD journey, many people have contributed to my scientific formation, so I want to use this opportunity to thank to all of them. I would like to address special thanks to my advisor, Prof. Dr. Dr. Wolfgang Rhode for guidance and support during my time as a PhD student and also for the patience proved in many moments.

I want to thank also to Athina Meli for her constant interest in my scientific work, for the fruitful discussions to clarify important notions and for encouragement.

To Daniela Doerner, Thomas Bretz and Stefan Rügamer for their availability in clarifying analysis problems and mainly for the enormous help offered in dealing with the unfriendly computer languages.

To all my colleagues from Astrophysics and especially to my office mates Daniela Hadasch, Michael Backes and Dominik Neise, who cheered the days spent at the university. And again to Michael, Daniela and also to Evan Niner for the patience to correct this thesis.

I must not forget to thank our secretaries, Mrs. Eva Lorenz and Mrs. Monika Schoknecht without whom I would have been lost in the bureaucratical problems.

To the MAGIC collaboration for the opportunity offered to experience once in a life time moments at the Observatory Roche de Los Muchachos (La Palma) and also the possibility to make new contacts in the Astrophysics area.

And of course I am thanking to my family and friends who were by my side all this time, giving me the strength to go further.

I especially thank to my wife for making my life so wonderful during this time.

List of Figures

Bibliography

F. Aharonian et al. Variations of the TeV energy spectrum at different flux levels of Mkn 421 observed with the HEGRA system of Cherenkov telescopes. *Astronomy and Astrophysics*, 393: 89–99, 2002.

F. Aharonian et al. The Crab Nebula and Pulsar between 500 GeV and 80 TeV: Observations with the HEGRA Stereoscopic Air Cerenkov Telescopes. *Astrophysical Journal*, 614:897–913, 2004.

F. Aharonian et al. Observations of the Crab nebula with HESS. *Astronomy and Astrophysics*, 457: 899–915, 2006.

F. Aharonian et al. An Exceptional Very High Energy Gamma-Ray Flare of PKS 2155-304. *Astrophysical Journal Letters*, 664:L71–L74, 2007.

F. A. Aharonian, D. Khangulyan, and L. Costamante. Formation of hard very high energy gamma-ray spectra of blazars due to internal photon-photon absorption. *Monthly Notices of the Royal Astronomical Society*, 387:1206–1214, 2008.

F. A. Aharonian et al. Optimizing the angular resolution of the HEGRA telescope system to study the emission region of VHE gamma rays in the Crab Nebula. *Astronomy and Astrophysics*, 361: 1073–1078, 2000.

F. A. Aharonian et al. The time averaged TeV energy spectrum of MKN 501 of the extraordinary 1997 outburst as measured with the stereoscopic Cherenkov telescope system of HEGRA. *Astronomy and Astrophysics*, 349:11–28, 1999.

C. Akerlof et al. Detection of High Energy Gamma Rays from the Crab Nebula. In *International Cosmic Ray Conference*, volume 2, pages 135–138, 1990.

J. Albert and et al. Unfolding of differential energy spectra in the MAGIC experiment. *Nuclear Instruments and Methods in Physics Research A*, 583:494–506, 2007.

J. Albert et al. Observations of Markarian 421 with the MAGIC Telescope. *Astrophysical Journal*, 663:125–138, 2007a.

J. Albert et al. Variable Very High Energy Gamma-Ray Emission from Markarian 501. *Astrophysical Journal*, 669:862–883, 2007b.

J. Albert et al. Probing Quantum Gravity using Photons from a Mkn 501 Flare Observed by MAGIC. *ArXiv e-prints*, 708, 2007c.

J. Albert et al. VHE γ-Ray Observation of the Crab Nebula and its Pulsar with the MAGIC Telescope. *Astrophysical Journal*, 674:1037–1055, 2008a.

J. Albert et al. Very-High-Energy gamma rays from a Distant Quasar: How Transparent Is the Universe? *Science*, 320:1752–1754, 2008b.

E. Amato, D. Guetta, and P. Blasi. Signatures of high energy protons in pulsar winds. *Astronomy and Astrophysics*, 402:827–836, 2003.

M. Amenomori et al. Observation of Multi-TEV Gamma Rays from the Crab Nebula using the Tibet Air Shower Array. *Astrophysical Journal Letters*, 525:L93–L96, 1999.

J. Arons. Pair creation above pulsar polar caps - Geometrical structure and energetics of slot gaps. *Astrophysical Journal*, 266:215–241, 1983.

H. Arp. Atlas of Peculiar Galaxies. *Astrophysical Journal Supplement*, 14:1–20, 1966.

F. Arqueros et al. Very high-energy /γ-ray observations of the Crab nebula and other potential sources with the GRAAL experiment. *Astroparticle Physics*, 17:293–318, 2002.

A. M. Atoyan and F. A. Aharonian. On the mechanisms of gamma radiation in the Crab Nebula. *Monthly Notices of the Royal Astronomical Society*, 278:525–541, 1996.

Pierre Auger, P. Ehrenfest, R. Maze, J. Daudin, and Robley A. Fréon. Extensive cosmic-ray showers. *Rev. Mod. Phys.*, 11(3-4):288–291, 1939.

Aurore Simonnet, Sonoma State University. The large and small of m87. `http://www.nasa.gov/centers/goddard/news/topstory/2007/active_galaxy.html`, 2008.

P. Baillon and et al. Observation of the Crab in Multi TeV Gamma Rays by the THEMISTOCLE experiment. In *International Cosmic Ray Conference*, volume 1, pages 220–223, 1991.

D.; et al. Bastieri. The mirrors for the magic telescopes. In *Proceedings of the 29th International Cosmic Ray Conference. August 3-10, 2005, Pune, India*, pages 283–286, 2005.

W. Bednarek and M. Bartosik. Gamma-rays from the pulsar wind nebulae. *Astronomy and Astrophysics*, 405:689–702, 2003.

W. Bednarek and R. J. Protheroe. Gamma Rays and Neutrinos from the Crab Nebula Produced by Pulsar Accelerated Nuclei. *Physical Review Letters*, 79:2616–2619, 1997.

W. Bednarek and R. M. Wagner. A model for delayed emission in a very-high energy gamma-ray flare in Markarian 501. *Astronomy and Astrophysics*, 486:679–682, 2008.

A. R. Bell. The acceleration of cosmic rays in shock fronts. I. *Monthly Notices of the Royal Astronomical Society*, 182:147–156, 1978.

R. D. Blandford and D. G. Payne. Compton scattering in a converging fluid flow. I - The transfer equation. II - Radiation-dominated shock. *Monthly Notices of the Royal Astronomical Society*, 194:1033–1039, 1981.

V. Blobel. Unfolding methods in high-energy experiments. In DESY, editor, *Proceedings of the 1984. CERN School of Computing*, pages 84–114, 1984.

V. Blobel. An unfolding methods in high-energy experiments. 2002.

S. D. Bloom and A. P. Marscher. An Analysis of the Synchrotron Self-Compton Model for the Multi–Wave Band Spectra of Blazars. *Astrophysical Journal*, 461:657–663, 1996.

Haidrun Bojahr. *Suche nach TeV-Blazaren mit dem HEGRA-System der abblidenden Čerenkov-Teleskope*. PhD thesis, Universität Wuppertal, Dezember 2002. WubDis 2002-3.

M. Böttcher and C. D. Dermer. An Evolutionary Scenario for Blazar Unification. *Astrophysical Journal*, 564:86–91, 2002.

S. M. Bradbury et al. Detection of γ-rays above 1.5TeV from MKN 501. *Astronomy and Astrophysics*, 320:L5–L8, 1997.

T; Bretz et al. Standard Analysis for the MAGIC Telescope. In *Proceedings of the 29th International Cosmic Ray Conference. August 3-10, 2005, Pune, India*, pages 315–318, 2005.

Thomas Bretz. *Observation of the Active Galactic Nucleus 1ES 1218+304 with the MAGIC-telescope*. PhD thesis, Universität Würtzburg, 2006.

Bretz, T; et al. Comparison of On-Off and Wobble mode observations for MAGIC. In *Proceedings of the 29th International Cosmic Ray Conference. August 3-10, 2005, Pune, India*, pages 311–314, 2005.

R. J. Brucato and J. Kristian. Optical Candidates for Two X-Ray Sources. *Astrophysical Journal Letters*, 173:L105–107, 1972.

J. H. Buckley. ASTROPHYSICS: What the Wild Things Are. *Science*, 279:676–677, 1998.

Cangoroo. The first and second fermi acceleration. `http://icrhp9.icrr.u-tokyo.ac.jp/image/FermiAcceleration1.gif`, July 2008.

M. et al. Cappellari. The Counterrotating Core and the Black Hole Mass of IC 1459. *Astrophysical Journal*, 578:787–805, 2002.

B. W. Carroll and D. A. Ostlie. *An Introduction to Modern Astrophysics*. Institute for Mathematics and Its Applications, 1996.

A. Cavaliere and V. D'Elia. The Blazar Main Sequence. *Astrophysical Journal*, 571:226–233, 2002.

P. M. Chadwick et al. Very High Energy Gamma Rays from PKS 2155-304. *Astrophysical Journal*, 513:161–167, 1999.

P. Charlot et al. Simultaneous radio-interferometric and high-energy TeV observations of the γ-ray blazar Mkn 421. *Astronomy and Astrophysics*, 457:455–465, 2006.

K. S. Cheng, C. Ho, and M. Ruderman. Energetic radiation from rapidly spinning pulsars. I - Outer magnetosphere gaps. II - VELA and Crab. *Astrophysical Journal*, 300:500–539, 1986.

A. C. Cheung, D. M. Rank, C. H. Townes, and W. J. Welch. Further Microwave Emission Lines and Clouds of Ammonia in Our Galaxy. *Nature*, 221:917–919, 1969.

J. Chiang and R. Mukherjee. The Luminosity Function of the EGRET Gamma-Ray Blazars. *Astrophysical Journal*, 496:752–760, 1998.

J. Chiang and R. W. Romani. Gamma radiation from pulsar magnetospheric gaps. *Astrophysical Journal*, 400:629–637, 1992.

L. Chiappetti et al. Spectral Evolution of PKS 2155-304 Observed with BeppoSAX during an Active Gamma-Ray Phase. *Astrophysical Journal*, 521:552–560, 1999.

M. J. Claussen and K.-Y. Lo. Circumnuclear water vapor masers in active galaxies. *Astrophysical Journal*, 308:592–599, 1986.

S. Coleman and S. L. Glashow. High-energy tests of Lorentz invariance. *Physical Review D*, 59(11): 1–14, 1999.

G. Cowan. *Statistical Data Analysis*. Oxford University Press, 1998.

J. K. Daugherty and A. K. Harding. Electromagnetic cascades in pulsars. *Astrophysical Journal*, 252:337–347, 1982.

O. C. de Jager and A. K. Harding. The expected high-energy to ultra-high-energy gamma-ray spectrum of the Crab Nebula. *Astrophysical Journal*, 396:161–172, 1992.

O. C. de Jager et al. Gamma-Ray Observations of the Crab Nebula: A Study of the Synchro-Compton Spectrum. *Astrophysical Journal*, 457:253–266, 1996.

M. de Naurois et al. Measurement of the Crab Flux above 60 GeV with the CELESTE Cerenkov Telescope. *Astrophysical Journal*, 566:343–357, 2002.

C. D. Dermer and R. Schlickeiser. On the location of the acceleration and emission sites in gamma-ray blazars. *Astrophysical Journal Supplement*, 90:945–948, 1994.

C. D. Dermer, S. J. Sturner, and R. Schlickeiser. Nonthermal Compton and Synchrotron Processes in the Jets of Active Galactic Nuclei. *Astrophysical Journal Supplement*, 109:103–137, 1997.

A. Djannati-Atai et al. First Results from Southern Hemisphere AGN Observations Obtained with the H.E.S.S. VHE Gamma-Ray Telescopes. In *International Cosmic Ray Conference*, volume 5, pages 2575–2578, 2003.

T. P. Dominici, Z. Abraham, R. Teixeira, and P. Benevides-Soares. Long-Term Optical Variability of the Blazars PKS 2005-489 and PKS 2155-304. *Astrophysical Journal*, 128:47–55, 2004.

East Tennessee State University. The jets and core of ngc 4261. `http://www.etsu.edu/math/gardner/5310/diffgeo.htm`, 2008.

Exploraciones en la Ciencia de los Sistemas Complejos. Ngc 1097 in radio. `http://weblogs.madrimasd.org/complejidad/archive/2006/10/31/48890.aspx`, 2008.

NRAO AUI F. N. Owen (NRAO) et al., VLA. The large and small of m87. `http://apod.nasa.gov/apod/ap990216.html`, 2008.

B. L. Fanaroff and J. M. Riley. The morphology of extragalactic radio sources of high and low luminosity. *Monthly Notices of the Royal Astronomical Society*, 167:31P–36P, 1974.

E. Fermi. On the Origin of the Cosmic Radiation. *Physical Review*, 75:1169–1174, 1949.

L. Ferrarese, H. C. Ford, and W. Jaffe. Evidence for a Massive Black Hole in the Active Galaxy NGC 4261 from Hubble Space Telescope Images and Spectra. *Astrophysical Journal*, 470:444–459, 1996.

J. A. Gaidos et al. Very Rapid and Energetic Bursts of TeV Photons from the Active Galaxy Markarian 421. *Nature*, 383:319–320, 1996.

Gaug, M; et al. Calibration of the MAGIC Telescope. In *Proceedings of the 29th International Cosmic Ray Conference. August 3-10, 2005, Pune, India*, pages 375–378, 2005.

G. Ghisellini, F. Tavecchio, and M. Chiaberge. Structured jets in TeV BL Lac objects and radiogalaxies. Implications for the observed properties. *Astronomy and Astrophysics*, 432:401–410, 2005.

G. Ghisellini et al. A theoretical unifying scheme for gamma-ray bright blazars. *Monthly Notices of the Royal Astronomical Society*, 301:451–468, 1998.

G. Giovannini, L. Feretti, T. Venturi, W. D. Cotton, and L. Lara. VLBI Observations of Mrk421 and Mrk501. In *BL Lac Phenomenon*, volume 159 of *Astronomical Society of the Pacific Conference Series*, pages 439–442, 1999.

M. Giroletti et al. Parsec-Scale Properties of Markarian 501. *Astrophysical Journal*, 600:127–140, 2004.

P. Goret et al. Observations of TeV gamma rays from the Crab nebula. *Astronomy and Astrophysics*, 270:401–406, 1993.

R. J. Gould. High-Energy Photons from the Compton-Synchrotron Process in the Crab Nebula. *Physical Review Letters*, 15:577–579, 1965.

L. J. Greenhill, C. Henkel, R. Becker, T. L. Wilson, and J. G. A. Wouterloot. Centripetal acceleration within the subparsec nuclear maser disk of NGC4258. *Astronomy and Astrophysics*, 304:21–33, 1995.

K. Greisen. Extensive cosmic-ray showers. *Prog. Cosmic Ray Phys.*, 3:1–3, 1956.

D. Hadasch. Study of the magic performance at high zenith angles and application of the results on a very high energy gamma ray flare of the blazar pks 2155-304. Master's thesis, University of Dortmund, 2008.

D. Hadasch, Bretz T., Mazin D., et al. High zenith angle observation of PKS 2155-304 with the MAGIC telescope. *Heidelberg International Symposium of High Energy Gamma-Ray Astronomy, July, 7–11*, 2008.

A. K. Harding, E. Tademaru, and L. W. Esposito. A curvature-radiation-pair-production model for gamma-ray pulsars. *Astrophysical Journal*, 225:226–236, 1978.

R. J. et al. Harms. HST FOS spectroscopy of M87: Evidence for a disk of ionized gas around a massive black hole. *Astrophysical Journal Letters*, 435:L35–L38, 1994.

R. C. Hartman et al. Multiepoch Multiwavelength Spectra and Models for Blazar 3C 279. *Astrophysical Journal*, 553:683–694, 2001.

M. Harwit, R. J. Protheroe, and P. L. Biermann. TEV Cerenkov Events as Bose-Einstein Gamma Condensations. *Astrophysical Journal Letters*, 524:L91–L94, 1999.

A. D. Haschick, W. A. Baan, and E. W. Peng. The masering torus in NGC 4258. *Astrophysical Journal Letters*, 437:L35–L38, 1994.

Walter Heitler. *The quantum theory of radiation*. Clarendon Press, 3-rd edition, 1966.

A. Hewish, S. J. Bell, J. D. Pilkington, P. F. Scott, and R. A. Collins. Observation of a Rapidly Pulsating Radio Source. *Nature*, 217:709–713, 1968.

A. M. Hillas. Ultra high energy cosmic rays. In M. M. Shapiro, editor, *NATO ASIC Proc. 107: Composition and Origin of Cosmic Rays*, pages 125–148, 1983.

A. M. Hillas et al. The Spectrum of TeV Gamma Rays from the Crab Nebula. *Astrophysical Journal*, 503:744–759, 1998.

D. Horns and HEGRA Collaboration. Studies of the Crab Nebula Based upon 400 Hours of Observations with the HEGRA System of Cherenkov Telescopes. In *International Cosmic Ray Conference*, volume 4, pages 2373–2376, 2003.

John D. Jackson. *Classical Electrodynamics*. Wiley, 3-rd edition, 1998.

K. Katarzyński, H. Sol, and A. Kus. The multifrequency emission of Mrk 501. From radio to TeV gamma-rays. *Astronomy and Astrophysics*, 367:809–825, 2001.

K. Katarzyński, H. Sol, and A. Kus. The multifrequency variability of Mrk 421. *Astronomy and Astrophysics*, 410:101–115, 2003.

K. I. Kellermann, R. C. Vermeulen, J. A. Zensus, and M. H. Cohen. Sub-Milliarcsecond Imaging of Quasars and Active Galactic Nuclei. *Astrophysical Journal*, 115:1295–1318, 1998.

K. I. Kellermann et al. Sub-Milliarcsecond Imaging of Quasars and Active Galactic Nuclei. III. Kinematics of Parsec-scale Radio Jets. *Astrophysical Journal*, 609:539–563, 2004.

K. I. Kellermann et al. Doppler boosting, superluminal motion, and the kinematics of AGN jets. *Astrophysics and Space Science*, 311:231–239, 2007.

C. F. Kennel and F. V. Coroniti. Confinement of the Crab pulsar's wind by its supernova remnant. *Astrophysical Journal*, 283:694–709, 1984a.

C. F. Kennel and F. V. Coroniti. Magnetohydrodynamic model of Crab nebula radiation. *Astrophysical Journal*, 283:710–730, 1984b.

R. C. Kennicutt. Evolution of the Stars and Gas in Galaxies, by B.M. Tinsley. In *Bulletin of the American Astronomical Society*, volume 31, pages 1560–+, 1999.

T. M. Kneiske. Gamma-ray background: a review. *ArXiv e-prints*, 707, 2007.

T. M. Kneiske and K. Mannheim. BL Lacertae contribution to the extragalactic gamma-ray background. *Astronomy and Astrophysics*, 479:41–47, 2008.

T. M. Kneiske, K. Mannheim, and D. H. Hartmann. Implications of cosmological gamma-ray absorption. I. Evolution of the metagalactic radiation field. *Astronomy and Astrophysics*, 386:1–11, 2002.

T. M. Kneiske, T. Bretz, K. Mannheim, and D. H. Hartmann. Implications of cosmological gamma-ray absorption. II. Modification of gamma-ray spectra. *Astronomy and Astrophysics*, 413:807–815, 2004.

A. Konopelko et al. Detection of gamma rays above 1 TeV from the Crab Nebula by the second HEGRA imaging atmospheric Cherenkov telescope at La Palma. *Astroparticle Physics*, 4:199–215, 1996.

Arthur Köstler. *Lunaticii*[1]. Humanitas, 1995.

H. Krawczynski, P. S. Coppi, and F. Aharonian. Time-dependent modelling of the Markarian 501 X-ray and TeV gamma-ray data taken during 1997 March and April. *Monthly Notices of the Royal Astronomical Society*, 336:721–735, 2002.

H. Krawczynski et al. Multiwavelength Observations of Strong Flares from the TeV Blazar 1ES 1959+650. *Astrophysical Journal*, 601:151–164, 2004.

T. P. Krichbaum, , et al. Sub-mas Jets in Gamma-Active Blazars: Results from High Frequency VLBI. In *IAU Colloq. 164: Radio Emission from Galactic and Extragalactic Compact Sources*, volume 144, pages 37–38, 1998.

T.P. Li and Y.Q. Ma. Analysis methods for results in gamma-ray astronomy. *Astrophysical Journal*, 272:317–324, 1983.

[1]The Sleepwalker

K. R. Lind and R. D. Blandford. Semidynamical models of radio jets - Relativistic beaming and source counts. *Astrophysical Journal*, 295:358–367, 1985.

F. et al. Macchetto. The Supermassive Black Hole of M87 and the Kinematics of Its Associated Gaseous Disk. *Astrophysical Journal*, 489:579–600, 1997.

G. M. Madejski et al. X-Ray Observations of BL Lacertae during the 1997 Outburst and Association with Quasar-like Characteristics. *Astrophysical Journal*, 521:145–154, 1999.

P. Majumdar et al. Preliminary Results on Crab from Pachmarhi Array of Cerenkov Telescopes. In *The Universe Viewed in Gamma-rays*, 2002.

M. A. Malkan. The ultraviolet excess of luminous quasars. II - Evidence for massive accretion disks. *Astrophysical Journal*, 268:582–590, 1983.

K. Mannheim. X-Ray Continuum Emission Caused by Relativistic Protons. In *Relativistic Hadrons in Cosmic Compact Objects*, volume 391, pages 57–66, 1991.

K. Mannheim. The proton blazar. *Astronomy and Astrophysics*, 269:67–76, 1993.

K. Mannheim. TeV Gamma-Rays from Proton Blazars. *Space Science Reviews*, 75:331–340, 1996.

S. G. Marchenko et al. Comparison of Epochs of Ejection of Superluminal Components with the Gamma-Ray Light Curves of EGRET Blazars. In *American Institute of Physics Conference Series*, volume 510, pages 357–361, 2000.

A. Mastichiadis and J. G. Kirk. Variability in the synchrotron self-Compton model of blazar emission. *Astronomy and Astrophysics*, 320:19–25, 1997.

R.; et al. Mirzoyan. The activ mirror control of the MAGIC Telescopes. In *Proceedings of the 28th International Cosmic Ray Conference. July 31-August 7, 2003. Trukuba, Japan*, pages 2935–2938, 2003.

M. et al. Miyoshi. Evidence for a Black-Hole from High Rotation Velocities in a Sub-Parsec Region of NGC4258. *Nature*, 373:127–129, 1995.

A. Mücke and M. Pohl. The contribution of unresolved radio-loud AGN to the extragalactic diffuse gamma-ray background. *Monthly Notices of the Royal Astronomical Society*, 312:177–193, 2000.

R. Mukherjee et al. Broadband Spectral Analysis of PKS 0528+134: A Report on Six Years of EGRET Observations. *Astrophysical Journal*, 527:132–142, 1999.

A. G. Muslimov and A. K. Harding. Extended Acceleration in Slot Gaps and Pulsar High-Energy Emission. *Astrophysical Journal*, 588:430–440, 2003.

N. Nakai, M. Inoue, K. Miyazawa, M. Miyoshi, and P. Hall. Search for Extremely-High-Velocity H_2O Maser Emission Seyfert Galaxies. *Publications of the Astronomical Society of Japan*, 47: 771–799, 1995.

ESA NASA and the Hubble Heritage Team (STScI/AURA)-ESA/Hubble Collaboration. The antennae galaxies in collision. `http://apod.nasa.gov/apod/ap061024.html`, 2008.

D. A. Neufeld and G. J. Melnick. Excitation of millimeter and submillimeter water masers. *Astrophysical Journal*, 368:215–230, 1991.

S. Oser et al. High-Energy Gamma-Ray Observations of the Crab Nebula and Pulsar with the Solar Tower Atmospheric Cerenkov Effect Experiment. *Astrophysical Journal*, 547:949–958, 2001.

A Ostankov et al. The image camera of the 17m diameter air cherenkov telescope magic. *Nuclear Instruments and Methods in Physics Research Section A*, 471(1-2):188–191, 2001.

S. Paltani, T. J.-L. Courvoisier, A. Blecha, and P. Bratschi. Very rapid optical variability of PKS 2155-304. *Astronomy and Astrophysics*, 327:539–549, 1997.

Paoletti, R.; et al. The Trigger System of the MAGIC Telescope. *IEEE Transactions on Nuclear Science*, 54(2):404–409, 2007.

V. Pavlidou and B. D. Fields. The Guaranteed Gamma-Ray Background. *Astrophysical Journal Letters*, 575:L5–L8, 2002.

T. J. et al. Pearson. Superluminal expansion of quasar 3C273. *Nature*, 290:365–368, 1981.

Y. C. Pei, S. M. Fall, and M. G. Hauser. Cosmic Histories of Stars, Gas, Heavy Elements, and Dust in Galaxies. *Astrophysical Journal*, 522:604–626, 1999.

D. Petry et al. Detection of VHE γ-rays from MKN 421 with the HEGRA Cherenkov Telescopes. *Astronomy and Astrophysics*, 311:L13–L16, 1996.

D. Petry et al. Multiwavelength Observations of Markarian 501 during the 1997 High State. *Astrophysical Journal*, 536:742–755, 2000.

David L. Phillips. A technique for the numerical solution of certain integral equations of the first kind. *Journal of the ACM*, 9(1):84–97, 1962.

E. Pian et al. BeppoSAX Observations of Unprecedented Synchrotron Activity in the BL Lacertae Object Markarian 501. *Astrophysical Journal Letters*, 492:L17–L20, 1998.

B. G. Piner and P. G. Edwards. The Parsec-Scale Structure and Jet Motions of the TeV Blazars 1ES 1959+650, PKS 2155-304, and 1ES 2344+514. *Astrophysical Journal*, 600:115–126, 2004.

B. G. Piner and P. G. Edwards. VLBA Polarization Observations of Markarian 421 after a Gamma-Ray High State. *Astrophysical Journal*, 622:168–177, 2005.

B. G. Piner et al. VSOP and Ground-based VLBI Imaging of the TEV Blazar Markarian 421 at Multiple Epochs. *Astrophysical Journal*, 525:176–190, 1999.

A. G. Polatidis et al. The First Caltech–Jodrell Bank VLBI Survey. I. lambda = 18 Centimeter Observations of 87 Sources. *Astrophysical Journal Supplement*, 98:1–32, 1995.

R. J. Protheroe and H. Meyer. An infrared background-TeV gamma-ray crisis? *Physics Letters B*, 493:1–2, 2000.

M. Punch et al. Detection of TeV photons from the active galaxy Markarian 421. *Nature*, 358: 477–+, 1992.

J. Quinn et al. Detection of Gamma Rays with E $>$ 300 GeV from Markarian 501. *Astrophysical Journal Letters*, 456:L83–L86, 1996.

M. J. Rees and J. E. Gunn. The origin of the magnetic field and relativistic particles in the Crab Nebula. *Monthly Notices of the Royal Astronomical Society*, 167:1–12, 1974.

Benjamin Riegel. Systematische untersuchung der bildparameter zur entwicklung einer standard-analyse für das magic-telescope. Master's thesis, Universität Würzburg, 2005.

George B. Rybicki and Alan P. Lightman. *Radiative Processes in Astrophysics*. Wiley-Interscience, 1985.

R. M. Sambruna, G. Ghisellini, E. Hooper, R. I. Kollgaard, J. E. Pesce, and C. M. Urry. ASCA and Contemporaneous Ground-based Observations of the BL Lacertae Objects 1749+096 and 2200+420 (BL Lac). *Astrophysical Journal*, 515:140–152, 1999.

R. M. Sambruna et al. The High-Energy Continuum Emission of the Gamma-Ray Blazar PKS 0528+134. *Astrophysical Journal*, 474:639–649, 1997.

S. Sauvage et al. Intraband absorption in n-doped InAs/GaAs quantum dots. *Applied Physics Letters*, 71:2785–2787, 1997.

C. A. Scharf and R. Mukherjee. A Statistical Detection of Gamma-Ray Emission from Galaxy Clusters: Implications for the Gamma-Ray Background and Structure Formation. *Astrophysical Journal*, 580:154–163, 2002.

M. Schmidt. 3C 273 : A Star-Like Object with Large Red-Shift. *Nature*, 197:1040–1040, 1963.

C. K. Seyfert. Nuclear Emission in Spiral Nebulae. *Astrophysical Journal*, 97:28–41, 1943.

G. A. Shields. Thermal continuum from acretion disks in quasars. *Nature*, 272:706–708, 1978.

M. Sikora, J. G. Kirk, M. C. Begelman, and P. Schneider. Electron injection by relativistic protons in active galactic nuclei. *Astrophysical Journal Letters*, 320:L81–L85, 1987.

M. Sikora, M. C. Begelman, and M. J. Rees. Comptonization of diffuse ambient radiation by a relativistic jet: The source of gamma rays from blazars? *Astrophysical Journal*, 421:153–162, 1994.

Hubble Site. The hubble classification of galaxies. `http://hubblesite.org/newscenter/archive/releases/1999/34/image/o/`, July 2008.

Todor Stanev. *High energy cosmic rays*. Springer, 2-nd edition, 2004.

Ł. Stawarz, T. M. Kneiske, and J. Kataoka. Kiloparsec-Scale Jets in FR I Radio Galaxies and the γ-Ray Background. *Astrophysical Journal*, 637:693–698, 2006.

F. W. Stecker and M. H. Salamon. The Gamma-Ray Background from Blazars: A New Look. *Astrophysical Journal*, 464:600–605, 1996.

T. Tanimori et al. Detection of Gamma Rays of up to 50 TeV from the Crab Nebula. *Astrophysical Journal Letters*, 492:L33–L36, 1998.

D. Tescaro et al. Study of the performance and capability of the new ultra-fast 2 GSample/s FADC data acquisition system of the MAGIC telescope. *ArXiv e-prints*, 709, 2007.

A. Toomre and J. Toomre. Galactic Bridges and Tails. *Astrophysical Journal*, 178:623–666, 1972.

Universita degli studi di Firenze. The crab nebula in optical and x-ray. `http://www.astro.unifi.it/gruppi/plasmi/ricerca/rmhd.html`, July 2008.

G. Vacanti et al. Gamma-ray observations of the Crab Nebula at TeV energies. *Astrophysical Journal*, 377:467–479, 1991.

Robert M. Wagner. The magic telescope. `http://commons.wikimedia.org/wiki/Image:The_MAGIC_Telescope.jpg`, July 2008.

Robert M. Wagner. *Measurements of Very High Energy Gamma-Ray Emission from Four Blazars Using the MAGIC Telescope and a Comparative Study*. PhD thesis, Fakultät für Physik der Technischen Institut München, November 2006. MPP 2006-245.

Wolfgang Wagner. *Design and Realisation of a new AMANDA Data Acquisition System with Transient Waveform Recordes*. PhD thesis, Universität Dortmund, Oktober 2004. DissDo 2004-169.

T. C. Weekes et al. Observation of TeV gamma rays from the Crab nebula using the atmospheric Cerenkov imaging technique. *Astrophysical Journal*, 342:379–395, 1989.

Steven Weinberg. *Gravitation and Cosmology*. John Wiley & Sons, 1972.

C. J. Willott. Four Quasars above Redshift 6 Discovered by the Canada-France High-z Quasar Survey. *Astrophysical Journal*, 134:2435–2450, 2007.

E. R. Wollman, T. R. Geballe, J. H. Lacy, C. H. Townes, and D. M. Rank. NE II 12.8 micron emission from the galactic center. II. *Astrophysical Journal Letters*, 218:L103–L107, 1977.

Roberta Zanin. *Observation and Analysis of VHE Gamma Emission from AGN 1ES 1959+650 with the MAGIC Telescope*. PhD thesis, Universita degli studi di Padova, 2006.

Y. B. Zel'Dovich and I. D. Novikov. Mass of Quasi-Stellar Objects. *Soviet Physics Doklady*, 9: 834–837, 1965.

F. J. Zhang and L. B. Baath. The submilliarcsecond radio structures of the two BL Lac objects Mkn421 and 0735 + 178. *Monthly Notices of the Royal Astronomical Society*, 248:566–571, 1991.

Shuang N. Zhang. Similar phenomena at different scales: black holes, the Sun, γ-ray bursts, supernovae, galaxies and galaxy clusters. In *Proceedings of the International Astronomical Union, 2*, pages 41–62, 2006.